Optimization and Control of a Dual-Motor Hybrid Opposed Piston Engine

by

Joseph A. Drallmeier

A dissertation submitted in partial fulfillment
of the requirements for the degree of
Doctor of Philosophy
(Mechanical Engineering)
in the University of Michigan
2022

Doctoral Committee:

Associate Research Scientist Jason Siegel, Co-Chair
Professor Anna Stefanoupoulou, Co-Chair
Professor Andre Boehman
Professor Heath Hofmann
Professor Ilya Kolmanovsky
Assistant Research Scientist Robert Middleton

Joseph A. Drallmeier
drallmei@umich.edu
ORCID iD: 0000-0001-7162-592X

To my parents, who have provided me with every imaginable opportunity.

ACKNOWLEDGMENTS

I would like to start this dissertation with a show of gratitude to the numerous individuals who helped make this possible. First, I want to thank Dr. Jason Siegel. Jason, without your help in the test cell and in the theory behind the controls development, I would most certainly still be struggling to even get this engine running. Your intuition and problem solving abilities, as well as the general curiosity in which you approach all research, are an inspiration. Dr. Stefanopoulou, I am incredibly grateful for you accepting me into your lab. Your enthusiasm and dedication to research has been imperative in my development as a researcher. Dr. Robert Middleton, thank you for all of the practical help and advice with my research as well as your excellent feedback on all of my published papers and presentations.

I would also like to thank the other members of my dissertation committee. Dr. Andre Boehman, thank you for your test cell and fuels support, as well as providing rewarding discussions on the advancement of this research. Dr. Ilya Kolmanovsky, thank you for being an excellent instructor and providing me with the optimization and control theory necessary to complete this work. And finally, Dr Heath Hofmann, thank you so much for all of the help in developing the electric machine control. Your guidance and expertise has been invaluable to this work.

I also owe a big thank you to all of the Powertrain Control Lab members, past and present, that I have had the opportunity to work with. Specifically, Dr. Shima Nazari, thank you for all of the guidance you have provided me. You allowed me to tag along on some of your work when I started as a graduate student, and you helped me finish my own work as I wrapped up my PhD. I can't thank you enough. Dr. Mitch Bieniek and Dr. Saravanan Duraiarasan, I can't imagine a better pair of lab mates to take classes with, work on projects, and and have random conversations in the Autolab with. Omar Ahmad, thank you for always being the responsible lab mate when it comes to preparing for conferences, and keeping me on the right track. Abhishek Nayak, thank you for all the support with the motor controls and enabling this work to progress.

To all of the members of Achates Power who have supported this work, Ashwin Salvi, Ming Huo, Sasan Barissi, Ryan MacKenzie, John Blacklock, and all other Achates Power employees, thank you for all of the advice and help for on this work that you have provided.

I am also thankful for all of the support from the Auto Lab. Chuck Solbrig, thank you for patiently sitting with me in the control room for all of the countless hours running, and probably more so debugging, the test cell. Jim Elkins, your help and wise guidance were instrumental in setting up the test cell. Kent Pruss, thank you for the help in fabricating every single unique part that went into this work. Bill Kirkpatrick, thank you for always being willing to lend a hand with whatever random task I had, and for the lengthy chats about two-stroke opposed piston engines and whatever else we may have stumbled upon.

And finally, thank you to my family. Maddie, thank you for being my best friend and your endless love and support throughout graduate school and whatever comes next. To all of my siblings, you guys are who made me who I am. I look up to every one of you and what you have been able to accomplish, and it shows me I can do anything I put my mind to. Dad, your advice, example, and ever present wisdom has had such an influence on my life that I can't put it into words. All I can say is thank you. And lastly, and most importantly, Mom, you deserve the biggest thank you I can contrive. You have taught me to do what I do with confidence and satisfaction. To believe in myself. I have, and will continually, learn from your example. Thank you.

TABLE OF CONTENTS

LIST OF FIGURES

LIST OF TABLES

ABSTRACT

In hybrid electric vehicles (HEV), the added degree of freedom from multiple power sources providing the demanded traction power allows for more efficient utilization of a downsized internal combustion engine (ICE). This thesis investigates the opportunity for hybridization to maximize the potential benefits of the opposed piston (OP) engine, leveraging the unique downsizing capabilities, reduced heat transfer losses, and increased power to weight ration of this engine by advancing the state of modeling and developing novel control algorithms. The powertrain architecture studied is a dual motor series hybrid design. Each crankshaft is directly coupled to a single electric motor, eliminating the conventional geartrain linking the two crankshafts along with the associated friction and weight. In this way, the electric motors can directly extract the work generated by the engine and regulate the crankshaft dynamics, introducing the capability to dynamically vary compression ratio, combustion volume, and scavenging dynamics. To realize these potential benefits, coordination between the engine, control actuators, and motor torque is necessary.

For intra-cycle operation, meaning the operation of the engine within a single cycle, a novel scheme utilizing nonlinear optimization of a 0-D model iteratively coupled to a high fidelity model is formulated to capture the system dynamics while also computing the optimal crankshaft motion profile which maximizes the work generated by the system. This iterative approach reduces the model complexity used in the optimal control problem (OCP) while capturing the gas exchange dynamics critical to the 2-stroke cycle of the OP engine. Results from this optimization process show that a crankshaft motion profile with near constant motor torque maximizes the work extraction efficiency of the system. Model uncertainty created challenges for linear quadratic state feedback control used to regulate the desired piston motion profile. Fortunately, we could leverage the repetitive nature of the OP engine to develop an iterative trajectory optimization (ITO) algorithm. This allows a new tracking reference of the crankshaft motion to be determined in real-time Which could optimize the system efficiency in the presence of disturbances and model uncertainty. Experimental results demonstrate the rapid convergence and near optimal crankshaft motion profiles for the ITO strategy as well as its proficiency under both motored

and fired cycle operation. While the general ITO algorithm developed here has application beyond the hybrid OP engine, the intra-cycle analysis showed that the electric machine efficiency was the dominant factor in system efficiency. Therefore, a piston motion profile which minimizes the motor torque amplitude maximizes the system efficiency over an engine-centric profile.

This thesis also considered the inter-cycle operation of this system. In a series HEV, the engine operating setpoint, including the engine speed, load, and phasing of the crankshafts, is decoupled from the instantaneous power demands of the vehicle. The engine calibration problem is addressed by implementing an onboard setpoint optimization algorithm, highlighting the ability to use crankshaft phasing as a controllable parameter impacting scavenging dynamics thermal efficiency. Finally, an optimization framework for the component sizing and energy management of a vehicle utilizing a dual-motor controlled OP engine in a series hybrid format is introduced. The onboard setpoint optimization enables ECL and crankshaft motion profiles to support higher system level operation such as hybrid topology design and fuel agnostic operation as these control actuators have little influence on the OP engine performance under normal operating conditions.

CHAPTER 1

Introduction

1.1 Background

In the United States, the transportation sector is the second largest sector of energy consumption, comprising 28% of the total U.S. primary energy use and accounting for 22% of total U.S. CO2 emissions [1]. Of the transportation sector energy consumption, light duty passenger vehicles are responsible for 61% [1], making personal mobility a central focus in reducing greenhouse gas (GHG) emissions. For the past century, improvement in transportation efficiency through the advancement of vehicle and internal combustion engine (ICE) technologies has been significant. Yet, in the face of these ever growing environmental concerns, continued improvement of engine efficiency at the historical rate has become exponentially more difficult as the field has matured [2]. Motivated by this challenge, several low emission vehicle (LEV) technologies are in development, including hybrid electric vehicles (HEV), fuel cell electric vehicles (FCEV), and battery electric vehicles (BEV). Of these, HEVs are an auspicious powertrain design in the near future due to the trend of technological convergence in the automotive industry as HEVs benefit from ongoing research in both internal combustion engines vehicles (ICEV) and BEVs [3].

1.2 Hybridization of Opposed Piston Engines

Hybridization offers an approach to improve vehicle fuel economy through diversification of the powertrain with multiple power sources. This allows for downsizing of the internal combustion engine while also decoupling the engine operation from the speed and load demands of a drive cycle. However, smaller engines also increase heat transfer losses and can yield lower peak efficiency. While the conventional four-stroke ICE provides an energy dense and relatively low-cost power source in a hybrid, the lower peak engine efficiency limits the overall potential of the hybrid system. Therefore, the opposed piston (OP) engine

has been proposed as an alternative internal combustion (IC) engine design to maximize the potential efficiency of hybrid powertrains [4–6]. Along with several thermodynamic benefits [7–9], the OP engine is inherently balanced in nature due to the two crankshafts operating opposite each other, allowing for downsizing though reduction in cylinder count rather than individual cylinder volume. This lends itself well to lower power, downsized, hybrid powertrain applications, without incurring the increased heat transfer losses of a conventional, four stroke internal combustion engine.

1.2.1 Opposed Piston Engines

Opposed piston engines have been commercialized since the late 1800's, and a detailed history of the development of these engines is given by Pirault et al. [9]. Several fundamental advantages of OP engines are well documented in literature [7, 10–14], and because of these, OP engines have been deployed in a wide variety of applications and remain a research interest. The general advantages of the OP engine design are:

- Smaller surface area to volume ratio to reduce heat transfer
- For the same power output, the energy input per cycle is reduced which leads to shorter combustion duration without excessive pressure rise rates
- Leaner operating conditions improve thermal efficiency and lower engine-out emissions

Several challenges that restricted the wide spread use of OP engines have recently been overcome by modern technology and innovative designs. For example, the inclusion of a biaxial wrist pin can compensate for the lack of load reversal and help lubricate the bearing between the piston and connecting rod [15]. Advances such as this have allowed OP engines to be reintroduced as a viable engine design with significant advantages over conventional four-stroke engine designs. While many variations of the OP engine exist, the main difference between designs is the method of work extraction. The types discussed here include the free piston OP engine and the OP engines with two crankshafts.

1.2.1.1 Free Piston Opposed Piston Engine

Free piston (FP) engines replace the conventional crankshaft of internal combustion engines with either hydraulic or electric power take-off. It is important to note that only a small subset of FP engines employ an OP architecture. However, some works [16–18] utilize an opposed piston, opposed cylinder (OPOC) design where two OP cylinders are linearly

orientated with hydraulic chambers between the cylinders to extract work. Due to the lack of a crankshaft to regulate the motion of the pistons, FP engines are capable of variable piston trajectories and compression ratios as well as a large reduction in friction losses. This provides significant opportunities for real-time control of in-cylinder conditions [10, 18]. However, this flexibility demands robust control of the piston motion as FP engines are highly susceptible to cycle-to-cycle variation as well as the possibility of pistons colliding with other engine components.

1.2.1.2 Crankshaft Based Opposed Piston Engine

For OP engines with a crankshaft, there are a wide variety of designs used to extract power from the pistons, ranging from a single crankshaft to designs with as many as four [9]. However, the double crankshaft designs appear to be the most prevalent [19, 20]. Similarly, most OP engine designs operate on a two-stroke cycle with the exception of the more complex sleeve valve design proposed by Pinnacle Engines which operates on a four-stroke cycle [8, 21]. Typically, the two crankshafts in an OP engine are linked externally through a geartrain and lead to a single power take-off, as depicted in Fig. 1.1a. While this design lends significant robustness to the engine operation where the FP engine design does not, there are certain trade-offs. First, the geartrain provides a significant source of friction, noise, and vibration. Additionally, coupling the crankshafts fixes the relative phasing between the two cranks. This operating parameter, known as exhaust crankshaft lead (ECL), along with the relative sizes of the intake and exhaust ports, determines the scavenging dynamics of a uniflow scavenged OP engine. Typically, the exhaust ports are traversed by the corresponding crankshaft (referred to as the exhaust crankshaft) before the opposing crankshaft (intake crankshaft) opens the intake ports for adequate blowdown of the burned gasses. This can be achieved by either the port height in the cylinder or an ECL, or both. As detailed by Naik et al. [12] the magnitude of the blowdown process is directly proportional to the energy released during combustion and thus the cylinder pressure. Therefore, for high power applications, a larger ECL is desired to ensure sufficient blowdown and limit backflow into the intake manifold. However, at low power setpoints a larger ECL reduces the expansion ratio, reducing fuel efficiency.

With these aspects in mind, this thesis investigates the control and optimization of a series hybrid architecture utilizing a uniflow scavenged OP engine in which the geartrain that couples the two crankshafts of the OP engine is eliminated. A motor-generator on each crankshaft extracts mechanical work from combustion and converts it to electricity, as shown in Fig. 1.1b. Not only can this configuration greatly reduce geartrain friction losses, but the electric motors can regulate the angular velocity of the crankshafts.

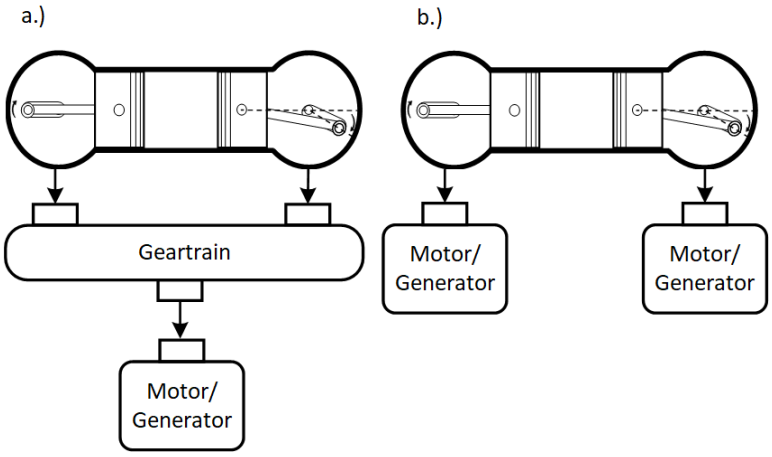

Figure 1.1: Schematic of a.) a hybrid OP engine design with a conventional geartrain linking the crankshafts and b.) a novel hybrid OP engine architecture decoupling the relative motion of each crankshaft.

With independent control of the piston trajectories, the capability to dynamically vary compression ratio, combustion volume, and scavenging dynamics is introduced, similar to FP engine designs, while maintaining the robustness provided by the crank slider mechanism and rotating inertia of the motor.

To realize these opportunities, control and optimization of both the intra-cycle operation, on the scale of crank angle degrees, and inter-cycle operation, on the scale of both minutes for engine setpoint and drive cycles for power management, requires consideration for the control and optimization of the entire system.

1.3 Intra-Cycle Operation

As the geartrain linking the two crankshafts of an OP engine has been removed in this work, it is necessary to maintain the relative positioning between the two pistons through control over the instantaneous crankshaft position. Therefore, the challenge is not only to control each crankshaft to a desired trajectory, but also to define the optimal position and velocity trajectories which the physical system is being to control to.

The first works to address the idea of optimizing piston motion in an internal combustion engine are from Mozurkewich et al. [22] and Hoffmann et al. [23], which optimized the finite-time thermodynamics of the irreversible Otto and Diesel cycles, respectively. More recent research in this area has largely focused on free piston engines due to the unconstrained nature of the engine design. Work from Xu et. al. [24] investigates the effects of various piston trajectories on the in-cylinder temperature and pressure as

well as oxides of nitrogen (NO_X) formation, but neglect discussion of the impact of piston trajectory on any efficiency metric. Several works on the opposed piston, opposed cylinder (OPOC) free piston engine design, including Zhang et al. [11] and Zhang et al. [18], investigate the effects of variable piston trajectory on emissions as well as thermal efficiencies. Yet, this work was limited to a sweep of predetermined trajectories rather than optimizing for a free piston trajectory input. Further, the ability to change the phasing of the pistons relative to each other was not addressed. As noted by Naik et al. [12], the ECL directly affects the timing of intake and exhaust port actuation and the scavenging performance of the engine. Further, this phasing of the piston position also changes the minimum volume of the cylinder during the compression stroke, making it a variable of interest when optimizing the piston trajectory.

In work from Eriksson et al. [25, 26], the indicated work output of a single cylinder engine was maximized by selecting a completely free heat release input while also applying constraints on emissions and engine performance. This input, however, was not translated to the corresponding directly controllable inputs. Further, all the works mentioned here are limited to discussion of indicated results and do not discuss the efficiencies associated with extracting the generated work. In this thesis, we show that the method of extracting work from the system is a critical component in the overall system efficiency [27]. Specifically, maximization of the indicated thermal efficiency of the engine while neglecting the electric motor efficiency can result in a net negative amount of work from the system.

1.4 Inter-Cycle Operation

In a series HEV, supervisory control is required to maintain system operation near areas of high efficiency. This includes controlling both the instantaneous operating setpoint as well as the power management of each powertrain component over entire drive cycles.

Several optimization based techniques exist for calibrating engine operation and are detailed in a recent survey [28]. These consist of both offline and online optimization processes. For offline optimization, the data is first collected on the engine and then run through regression or optimization techniques to determine optimal setpoints as well as future test points. An example of this is provided by Pal et al. [29] where Bayesian optimization is used to inform the selection possible optimal operating points through a trade-off between exploitation and exploration. This can be achieved with evaluation of the posterior distribution of the regressed non-parametric system model, but incurs a heavy computational cost. Online optimization processes utilize streaming data from the engine in real-time to shift engine operation to higher efficiency areas. This approach

includes extremum seeking methods [30], as well as other local regression and optimization schemes [31]. Additionally, techniques such as those presented by Malikopoulos et al. [32] use full exploration of the design space to learn a decentralized system model with which to optimize engine operation. In the pursuit of reducing calibration time and maintaining the ability to adjust to system disturbances or aging in real time, this work implements an online optimization routine.

For the power management strategy, physics based modeling was utilized to implement nonlinear optimization over a full drive cycle profile while minimizing fuel consumption and battery capacity fade in the vehicle system. While this analysis is not implementable online, it is used as an analysis tool for sizing the engine, electric machines, and battery components.

1.5 Contributions and Organization

This thesis presents the optimization and control techniques of a novel series hybrid design utilizing an OP engine. This consists of regulating the crankshaft motion during individual cycles to improve work extraction efficiency, as well as supervisory control for determining the engine operating point and power management between the engine and battery in the powertrain. The contributions of this thesis are as follows:

- *Modeling and Optimization of the Crankshaft Motion for a Dual Motor Controlled OP Engine*

  The system level efficiency of the hybrid OP engine is largely dependent on the harmonious operation of both the electric motors extracting work from the OP engine as well as the OP engine itself. Therefore, a methodology optimizing the motion of each crankshaft in an opposed piston engine utilizing compression ignition to maximize brake output power is developed, including the mechanical to electrical conversion efficiency for extracting the rotational work from the crankshafts and utilizing the motor torque as the input to the system. The conversion efficiency in this case is the electric motor efficiency for the motor attached to each crankshaft and is shown to be a dominant factor in the brake system efficiency. To avoid the model complexity necessary to adequately capture the gas exchange of the two stroke engine in the numerical optimization problem, an iterative procedure between a 0D and 1D co-simulation and the numerical optimization routine is developed. The optimization problem and the numerical techniques used to solve it are presented in Chapter 2 along with the proposed integrated framework of the high fidelity modeling and

optimization procedure is introduced. The iterative optimization process and results are published in:

  - Drallmeier, J., Siegel, J. B., Middleton, R., Stefanopoulou, A. G., "Optimizing Fuel Efficiency of an Opposed Piston Engine for Electric Power Generation" *International Journal of Engine Research*, 2022 [33]

These results highlight the importance of accounting for electric machine efficiency in the optimization process as well as the insensitivity of the OP engine operation to changes in intra-cycle crankshaft motion. This suggests the novel control authority over ECL and crankshaft motion can be better exploited in the inter-cycle operation.

- *Control Implementation and Experimental Validation of a Hybrid OP Engine*

  Chapter 3 presents the experimental test setup used to provide a proof of concept for this system as well as the control architecture to regulate the independent crankshaft motion. The position regulator was developed as a linear quadratic regulator with augmented integrator states for the position error of each crankshaft and the crankshaft motion represented as a double integrator. To account for the impact of engine torque on the crankshaft dynamics and provide a faster control response, a feedforward control input estimating the required motor torque based on cylinder pressure and crankshaft location is implemented. The controller design is published in:

  - Drallmeier, J., Siegel, J. B., Middleton, R., Stefanopoulou, A. G., Salvi, A., Huo, M. "Modeling and control of a hybrid opposed piston engine" in *2021 ASME Internal Combustion Engine Fall Technical Conference (ICEF)* [27]

  The experimental results show significant sensitivity to model uncertainty due to high cylinder pressure and reversal of piston motion near minimum volume. This causes the motor torque required to track the optimized trajectory obtained through the solution of the optimal control problem in Chapter 2 to be significantly different from the input predicted in simulation. This ill-conditioned nature of the system is quantified by linearizing the system at multiple points near minimum volume and evaluating the condition number in:

  - Drallmeier, J., Siegel, J. B., Stefanopoulou, A. G. "Comparison of Estimation Techniques for the Crankshaft Dynamics of an Opposed Piston Engine" in *2019 ASME Dynamic Systems and Control Conference (DSCC)* [34]

To further evaluate the interaction between the electric motor and the OP engine, detailed electrical loss simulations were used in conjunction with measured engine torque data to calculate efficiency of the individual components responsible for extracting work from the engine. This work compared the dual motor design shown in Fig 1.1b to the more robust system design shown in Fig 1.1a to assess whether an efficiency improvements could be achieved by removing the geartrain of the OP engine. While the geartrain adds stability to the OP engine regardless of the torque generated on each crankshaft, the maximum work extraction efficiency can be improved nearly 10% by removing the geartrain to reduce frictional losses and using appropriately sized motors. However, this improvement is highly dependent on electric motor operation. This analysis is detailed in:

  – Drallmeier, J., Hofmann, H., Middleton, R., Siegel, J. B., Stefanopoulou, A. G. "Work Extraction Efficiency in a Series Hybrid Opposed Piston Engine" *2021 SAE Technical Paper* Tech Rep 2021-01-1242 [6]

- *Online Technique for Iterative Trajectory Optimization*

  As shown in Chapter 3, the dual-motor system efficiency is highly dependent on the operation and required torque input from the electric motors. Any gains in efficiency from removing the geartrain can be lost to poor motor performance. Results from Chapter 2 show a near constant torque profile maximizes the work extraction efficiency of this system. However, the necessity to maintain the relative positioning between the two pistons requires control over the instantaneous crankshaft position and prohibits the use of constant intra-cycle torque control to maintain the desired engine speed. The challenge then is not only in controlling the crankshaft to a desired position trajectory; It is also in defining the optimal position and velocity trajectory to control to while avoiding the model uncertainty limiting the effectiveness of offline optimization. Chapter 4 details the development of an iterative learning algorithm to optimize the parameterized trajectory of a system in real time utilizing constrained optimization of a cost function generated from the performance values of the previous cycle. In this way, the repetitive nature of the OP engine can be leveraged to use the information rich signals from previous cycles to mitigate the effects of model uncertainty. The theory for this iterative trajectory optimization (ITO) algorithm is published in:

  – Drallmeier, J., Siegel, J. B., Stefanopoulou, A. G. "Iterative Learning-Based Trajectory Optimization Using Fourier Series Basis Functions" *IEEE Control*

Systems Letters, 2022 [35]

The theory for this algorithm was published separately from the application as this learning scheme has a generic formulation and can be applied outside the specific application of a hybrid OP engine system. The ITO scheme is then demonstrated experimentally and is shown to converge rapidly to near optimal crankshaft motion profiles while being applicable under both motored and fired cycle operation. These results are presented in:

– Drallmeier, J., Siegel, J. B., Middleton, R., Solbrig, C., Stefanopoulou, A. G. "Maximizing Efficiency of a Hybrid Opposed Piston Engine Through Iterative Trajectory Optimization" *IFAC Symposium on Advanced in Automotive Control*, 2022

- *Inter-Cycle Analysis including Setpoint Optimization and Energy Management*

  With a robust intra-cycle control structure and a reliable real-time motion planing scheme for the OP engine crankshafts, inter-cycle operation of the opposed piston engine can be explored. Conventionally, the ECL is fixed by a geartrain linking the exhaust and intake crankshafts and the boost pressure is the only viable control actuator to regulate the airflow through the cylinder during engine operation. However, Chapters 1-4 demonstrate the feasibility of controlling the motion of the two crankshafts separately, introducing the ECL as a controllable parameter in the hybridized OP engine which allows for variation in the effective compression and expansion ratio of the engine, along with scavenging performance. The introduction of this novel control actuator as well as the adjustable speed and load setpoint in a series hybrid OP engine powertrain architecture necessitates intensive calibration effort to realize any possible efficiency improvements. Therefore, Chapter 5 initiates this calibration process by exploring two power setpoints for the system, sweeping speed and ECL to evaluate the value of ECL as an actuator. Further, these two operating points are then used to validate an onboard setpoint optimization strategy to automate the calibration process. Again, the OP engine used in this work remained robust against changes in ECL even in inter-cycle operation. This suggests ECL and crankshaft motion profiles can be used to support higher system level operation such as hybrid topology design and fuel agnostic operation as these control actuators have little influence on the OP engine performance under normal operating conditions.

  Finally, using the operating characteristics of the OP engine captured in Chapter 5, Chapter 6 develops a framework for integrating the hybrid OP engine into a

vehicle system and sizing the individual components accordingly. This optimization procedure is then used to evaluate the relative operational cost of fuel consumption of the OP engine and the capacity fade within the hybrid vehicle battery pack.

CHAPTER 2

Modeling and Crankshaft Motion Optimization for a Series Hybrid OP Engine

The objective of this chapter is to outline a method of finding the optimal crankshaft motion of a hybrid OP engine which maximizes system efficiency using motor torque as the control input. To that end, the iterative approach for optimization including a numerical optimal control problem (OCP) coupled with a high fidelity model is outlined below. As this is still a fairly complex model with a large number of states, an analytical solution would be extremely difficult to provide, motivating the following numerical optimal control problem. The individual models as well as the coupling between the high fidelity model and the optimization model are also discussed [27]. Results and insights from the OCP are presented at the end of the chapter.

2.1 Optimal Control Problem

It is beneficial to describe the optimization problem setup before detailing the models used in the optimization process as this will inform the structure of the model. Therefore, the modeling of the system will first be described, followed by an outline of the optimization process.

2.1.1 System Description

The OP engine design used here implements two crankshafts to regulate the motion of two pistons moving in a single cylinder, as shown in Fig. 2.1. This engine operates on a two-stroke cycle with uniflow scavenging. The scavenging process is governed by the pressure ratio across the intake and exhaust ports while the ports are actuated by the motion of the pistons translating across them. The crankshaft which moves a piston across the exhaust ports is then denoted as the exhaust crankshaft, colored red in Fig. 2.1, with the intake

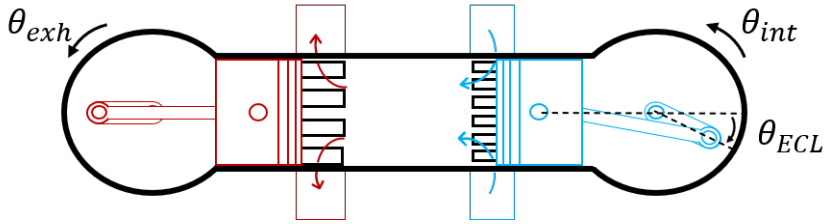

Figure 2.1: Schematic of a uniflow scavenged two-stroke opposed piston engine

crankshaft labeled in the same manner and colored blue in Fig. 2.1. The phasing of the two pistons' motions is denoted in Fig. 2.1 as θ_{ECL}, quantifying exhaust crankshaft lead (ECL), or the difference between the exhaust crankshaft and intake crankshaft position. As noted by Naik et al. [12], the ECL directly affects the timing of intake and exhaust port actuation and the scavenging performance of the engine. Further, this phasing of the piston position also changes the minimum volume of the cylinder during the compression stroke, making it a variable of interest when optimizing the piston trajectory. Electric motors are coupled directly to each crankshaft and provide an input torque to regulate the motion of the crankshafts as well as absorb the energy generated by the engine.

2.1.2 Problem Formulation

The brake efficiency of the hybrid OP engine system is defined as

$$\eta_b = \frac{W_{\text{out}}}{m_f Q_{\text{LHV}}} \tag{2.1}$$

where W_{out} is the output work of the system, including any engine or motor losses. The amount of work put into the system is denoted as the mass of fuel, m_f, multiplied by the lower heating value of the fuel, Q_{LHV}. If the amount of fuel used is fixed, the output power can be denoted as the difference of motor torque multiplied by the motor speed and any power losses from the motor. Therefore, the system efficiency can be maximized using the cost function

$$\begin{aligned}\max_{u\in U} J = \int_{t_0}^{t_1} \Big(& T_{\text{exh}}(u(t))\omega_{\text{exh}}(x(t),u(t)) - \\ & P_{\text{loss}_{\text{exh}}}(x(t),u(t)) + T_{\text{int}}(u(t))\omega_{\text{int}}(x(t),u(t)) - \\ & P_{\text{loss}_{\text{int}}}(x(t),u(t)) \Big) dt\end{aligned} \tag{2.2}$$

with the integral term being an expansion of the system output work. Here, T represents the motor torque for either the exhaust or intake motor, ω denotes the motor and crankshaft speed, and P_{loss} is the instantaneous power loss of the motors. The power loss is defined as

$$P_{loss} = \frac{3}{2} i^2 R + C\omega^2 \tag{2.3}$$

which accounts for the resistive losses and frictional losses, respectively. The current, i, used in the equation represents the quadrature current of the motor and is approximately proportional to the motor torque while R is the motor resistance. The coefficient C is used to scale the friction losses of the motor and is set to 0.038 here, estimated from the efficiency map of the electric motors used in experimentation. Any losses from the engine are included in the engine torque for a given setpoint and thus the motor torque through the torque balance on each crankshaft. It is important to note here that the motor losses are included as a power loss rather than an efficiency applied to the torque and speed term as $T * \omega * \eta_{\text{motor}}^{sgn(T)}$. If using an efficiency term as shown, there is a discontinuity in the cost function when there is a zero crossing of the motor torque. By defining the power loss term that is always positive as in Eqn. 2.3, the cost function is more well conditioned with the inclusion of a quadratic term with respect to torque and speed.

The system constraints are defined as

$$\dot{x} = f(x(t), u(t), t) \quad \forall t \in [t_0, t_1] \tag{2.4a}$$

$$|T(t)| \leq T_{\max} \tag{2.4b}$$

$$|\theta_{\text{exh}}(t) - \theta_{\text{int}}(t)| \leq ECL_{\text{lim}} \tag{2.4c}$$

$$|u(t)| = 2.56e5 \frac{Nm}{s} \tag{2.4d}$$

$$P(t_0) = P_0 \tag{2.4e}$$

$$\omega(t_1) - \omega(t_0) = 0 \tag{2.4f}$$

$$T(t_1) - T(t_0) = 0 \tag{2.4g}$$

$$\theta_{\text{exh}}(t_0) + \pi = 0 \tag{2.4h}$$

$$|\theta_{\text{exh}}(t_0) - \theta_{\text{int}}(t_0)| - ECL_{\text{set}} \leq ECL_0 \tag{2.4i}$$

$$\theta_{\text{exh}}(t_1) - \pi = 0 \tag{2.4j}$$

$$t_1 = \frac{2\pi}{\omega_{\text{set}}} \tag{2.4k}$$

where Eqn. 2.4a denotes the system dynamics with x representing the states, defined further in Eqn. 2.5. Constraint Eqn. 2.4b limits the instantaneous torque magnitude to

$\pm$1200Nm. The ECL at any point over the cycle is limited by Eqn. 2.4c, considered to be approximately 0.2 radians (12 degrees) here. The input, defined as $u(t) = \frac{dT(t)}{dt}$ which is the rate of change of motor torque, is bounded in Eqn. 2.4d. This ensures the trajectory reference obtained from the optimization process can be tracked in the high fidelity simulation. The limit is set to 2.56e5$\frac{Nm}{s}$, which allows the motor torque to change from a maximum torque of 1200Nm to a minimum of -1200Nm in approximately 90 crank angle degrees at 1600 RPM. The initial time t_0 is assumed to be time 0 and the initial pressure $P(t_0)$ is constrained to the value P_0 in Eqn. 2.4e, which is obtained from the high fidelity simulation. The initial and final speed and torque values in Eqn. 2.4f and 2.4g are held equal as the process should be repeatable for a steady state engine operating point. Note, subscripts denoting intake and exhaust crankshaft and motor are not included for speed and torque as the constraints are identical for each assembly. The initial position of the exhaust crankshaft, $\theta_{\text{exh}}(t_0)$ is set to bottom dead center in Eqn. 2.4h. The intake crankshaft is then initialized in Eqn. 2.4i near the ECL setpoint, with a slight deviation of $ECL_0 = 0.0175$ radians (1 degree) allowed. The final position in Eqn. 2.4j ensures a full revolution of the exhaust crankshaft, and similarly, the intake crankshaft due to the ECL constraint. Further, the final time is fixed in Eqn. 2.4k to ensure a constant average engine speed, denoted as ω_{set}. The model states represented as x are defined as

$$x = [\theta_{\text{exh}}, \omega_{\text{exh}}, \theta_{\text{int}}, \omega_{\text{int}}, P, T_{\text{exh}}, T_{\text{int}} \; t_{\text{comb1}}, t_{\text{comb2}}, AI]^T \tag{2.5}$$

where θ and ω define position and velocity of each crankshaft and motor, respectively. To reduce the number of states in the model, the motor and crankshaft position and velocity are considered identical, meaning the shafts are rigidly coupled, which in reality they are not. The cylinder pressure is denoted by P and torque by T. The states t_{comb1} and t_{comb2} are used to reference the duration of each stage of the combustion process and AI denotes the value of the auto-ignition integral. Further details will be provided in the modeling section.

2.1.3 Solving Methodology

The numerical optimal control software used to solve Eq. 2.2 was GPOPS-II [36], which implements a version of the Legendre-Gauss-Radau collocation method with adaptive mesh refinement techniques to discretize the optimal control problem. The resulting finite dimensional optimization problem is solved using IPOPT [37]. The system dynamics referred to in Eqn. 2.4a, is a simplified version of the modeling described elsewhere [27]

in regards to the coupling between engine crankshaft and motor as well as the open cycle breathing and thermodynamic models. However, despite this simplification, discrete changes are still present in the system dynamics due to the intake and exhaust port actuation, fuel injection, and the combustion process. To accommodate the changes in system dynamics over a single engine cycle, the problem was constructed as five sequential phases, each linked through identical state and input values at the terminus and start of adjacent phases. The phases, in order are:

1. intake
2. compression
3. pilot heat release
4. main heat release and expansion
5. exhaust

The start of the intake phase is considered to be at $\theta_{\text{exh}} = -\pi$ radians after top dead center (aTDC) for the exhaust crankshaft while the starting location for the intake crankshaft can vary ± 0.0175 radians (1 degree) around the ECL setpoint.

To ensure a continuous and well conditioned optimization problem, the gas exchange process is neglected in the model used for numerical optimization. While several semi-empirical models exist that adequately capture the scavenging dynamics [38], these models require crank angle resolved values for mass flow from the intake manifold and into the exhaust manifold. Modeling these flow can produce complex values and discontinuities that are not well suited for optimization. Therefore, we employ an iterative optimization scheme wherein a high-fidelity co-simulation provides the closed cycle boundary conditions of the pressure (P_{tr}), temperature (T_{tr}), and mass (m_{tr}) of the trapped mass to the optimization problem. As the cylinder pressure during the gas exchange process has little impact on the crankshaft dynamics, the assumption of constant cylinder pressure is used during this portion of the optimization problem. In the high-fidelity model, a 1D GT-Power simulation [39] captures the gas exchange process and thermodynamics while a 0D Matlab/Simulink model provides the unique crankshaft dynamics and combustion profile, in this case the mass fraction burned (MFB) fitted to experimental results, to supply boundary conditions to the optimization problem. The workflow for this process is shown in Figure 2.2 with the superscript * denoting the solution to the optimal control problem. The modeling framework provided in the following sections first describes the modeling used in the optimization problem. Then, a description of the portion of the model unique to the

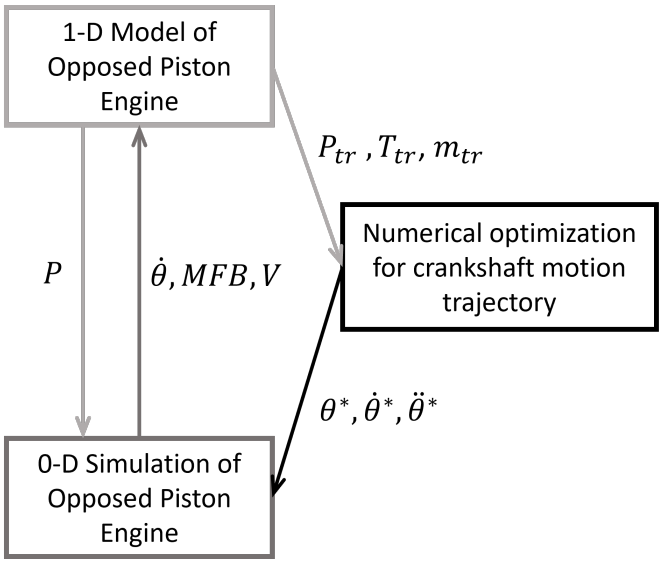

Figure 2.2: Realization of the iterative optimization of crankshaft motion

high-fidelity co-simulation is given. Iterations between the high-fidelity modeling and the optimization process are repeated until the pressure and temperature of the high-fidelity model at the port closing event are within 0.01 bar and 0.1 K, respectively, of the previous iteration values. Further, the peak cylinder pressure in the optimization model must be within 0.1 bar of the previous cycle, showing convergence of the optimization process.

As the optimization problem presented here is non-convex, the solution provided by the numerical software is possibly a local extrema rather than the globally optimal solution. Thus, the initial guesses of a constant rotational velocity as well as a constant motor torque were compared. Both cases converged to the same results, substantiating the optimization methodology. Note, for the constant torque case, the average torque was taken from the constant velocity case and used as the motor torque setpoint. However, this is only an approximation of constant torque control and over a single cycle, the ECL and average velocity in the open loop unstable system were not identical to the desired setpoint. This, however, is not critically important for the initial guess.

2.2 Optimization Problem Modeling

An outline of the model used in the optimal control problem is provided in Fig. 2.3 with the alternative dynamics for each model phase listed. Note that the crank angle reference is shown with respect to degrees after minimum volume (aMV), where the pistons are closest together. For an OP engine, using top dead center of a single crankshaft can be misleading,

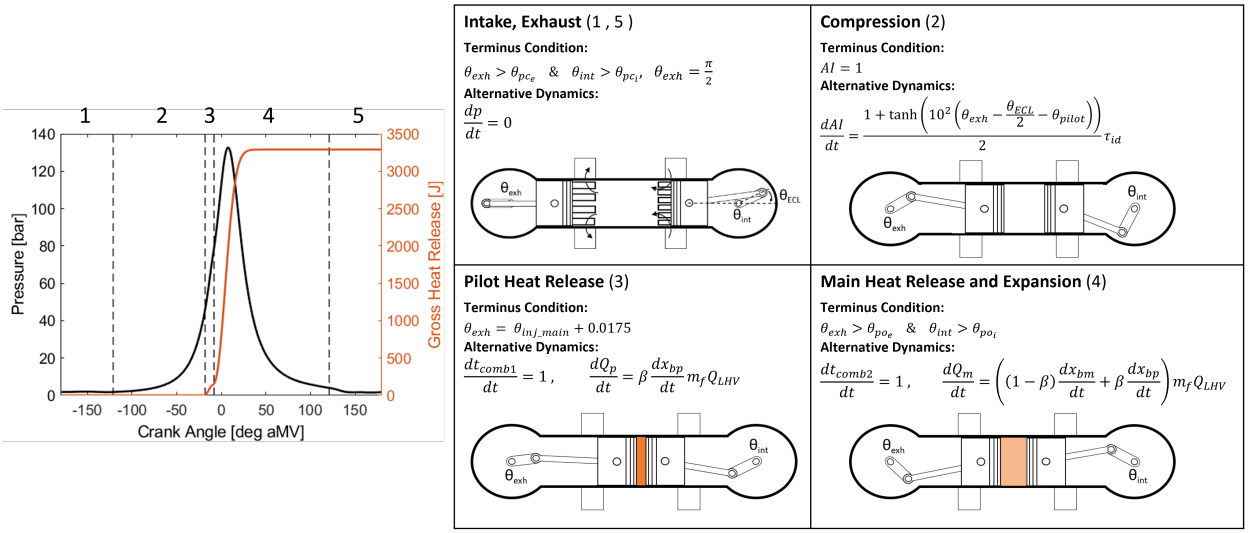

Figure 2.3: Outline of the modeling phases in the numerical optimization problem. Each phase is temporally sequential with identical state and input values at the transition of connected phases. Highlighted here are the varying dynamics defined in each phase of the model.

especially in the case presented here where the ECL is not a fixed value. This section will provide a short description of the relevant features of the model while discussion of the specific dynamics of each subsystem is provided in the following subsections.

During the intake and exhaust phases, the pressure dynamics are neglected as previously discussed. The effect of pressure on the rotational dynamics of the crankshafts during this portion of the cycle is negligible as the torque required to change the velocity profile is largely dependent of the system inertia as compared to the relatively low cylinder pressure. It is worth noting that this assumption does eliminate the impact of changes in ECL at port opening and closing on the scavenging process in the optimization problem. However, the optimal ECL setpoint during port actuation is highly dependent on the operating point [12]. Further, as will be shown in the results, the torque input required to drastically shift the ECL over a single cycle is detrimental to brake efficiency. Therefore, optimization of the ECL is well suited to a simple sweep of initial conditions. The intake phase ends when both the intake and exhaust pistons have completely covered the respective ports. The exhaust phase ends when the exhaust crankshaft reaches $\theta_{\text{exh}} = \pi$ radians, which corresponds to $t = \frac{2\pi}{\omega_{\text{set}}}$

In the compression phase, a hyperbolic tangent function is used to activate the auto-ignition integral only after the exhaust crankshaft has passed the pilot injection reference θ_{pilot}. For the OP engine considered in this work, we utilize a model of gasoline compression ignition (GCI) using a pump gasoline with an 87 anti-knock index (AKI)

due to the advantages detailed previously by Salvi et al. [14]. Therefore we consider a pilot and main heat release event where the start of combustion for the pilot heat release is governed by the chemical kinetics of the fuel and is modeled here using an ignition delay correlation. The ignition delay value in this case, τ_{id}, is provided by the ignition delay correlation where the parameters were selected based on previous experimental data with the same 87 AKI gasoline. The use of the hyperbolic tangent function smooths the discontinuity of introducing the ignition delay value. However, the dynamics for the auto-ignition integral have no impact on the cylinder pressure or rotational dynamics of the crankshafts and simply provide a means to estimate the start of the pilot heat release. The compression phase ends when the auto-ignition integral reaches 1.

The start of the pilot and main heat release are separated into two phases as the combustion process is represented using a double Weibe function to describe the mass fraction of fuel burned, denoted as x_{b}. The term β in Figure 2.3 refers to the percentage of the total fuel mass consumed by the pilot heat release. During phase 3, only the pilot heat release is active and contributing to the heat release rate. This phase ends when the exhaust crankshaft has gone 0.0175 radians, or 1 degree, past the crank angle at which the main injection starts. At this time, the rate of heat release contains the differential form of the Wiebe function for both the pilot and main heat release. The heat release process is completed as the mass fraction of fuel burned reaches 1 and the volume of the cylinder continues to expand. The main heat release and expansion phase ends when either the intake or exhaust ports are opened.

It should be noted here that the end conditions for each phase are dependent on the position of the crankshafts or other relevant dynamics. The independent variable of time can vary at the beginning of each phase from iteration to iteration. Thus, as the combustion process is modeled with respect to a given duration of time, additional states t_{comb1} and t_{comb2} are used to create a time reference for each combustion process that starts at 0 for each of the respective phases.

The following subsections provide the detailed modeling used for the numerical optimization problem described in this work and will define the dynamics and the state values θ, ω, P, and AI defined in Eqn. 2.5. Note however, that the states of motor torque and time for each combustion phase are left out as torque can be obtained directly from the control input and the time simply requires an integrator in the respective model phase. The majority of this model is described previously [27] with a modification of the in-cylinder thermodynamic model for use in the optimization process. This engine model combines the thermodynamic and kinematic models presented by Eriksson et al. [25] and Yar et al. [40], respectively. The parameters for the OP engine used in this work are provided in Table 2.1.

Table 2.1: Single cylinder OP engine parameters

Parameter	Value	Units
Displacement	1.64	L
Crank Radius	54	mm
Connecting Rod Length	258	mm
Bore	98.425	mm
Clearance Volume	7.6e4	mm^3
Inlet Port Closing	-129.5	deg
Exhaust Port Opening	121.0	deg

2.2.1 Pressure

Using the first law of thermodynamics, the energy balance for the closed cylinder system can be described as

$$\mathrm{d}U_\mathrm{s} = \mathrm{d}Q_\mathrm{comb} - \mathrm{d}Q_\mathrm{ht} - \mathrm{d}W \tag{2.6}$$

where the derivatives are with respect to time unless otherwise specified. Note this is a representation of the closed system as a constant pressure is assumed during the open portion of the cycle. The high-fidelity model provides the boundary conditions of trapped pressure temperature, and charge mass when the ports close. The crevice flow introduced by Eriksson et al. [25] is neglected and a constant charge mass is assumed. The change in sensible internal energy is denoted by $\mathrm{d}U_\mathrm{s}$, heat transfer is denoted as $\mathrm{d}Q_\mathrm{ht}$, and heat addition due to combustion is denoted as $\mathrm{d}Q_\mathrm{comb}$. Work extracted from the system, represented as $\mathrm{d}W$, is equal to

$$\mathrm{d}W = p\mathrm{d}V. \tag{2.7}$$

Using the ideal gas assumption, the change in internal sensible energy is given as

$$\mathrm{d}U_\mathrm{s} = m_\mathrm{c} C_\mathrm{v}(T)\mathrm{d}T \tag{2.8}$$

where m_c is the charge mass, T is the temperature, and the mass average specific heat at a constant volume, C_v is a function of charge temperature. Using the differential form of the ideal gas law with a constant mass

$$m_\mathrm{c} R\mathrm{d}T = p\mathrm{d}V + V\mathrm{d}P \tag{2.9}$$

where R is the gas constant. Here the gas constant of air (287 J/kg K) is used, similar to the 290 J/kg K used by Eriksson et al. [25]. Solving for dP, the pressure dynamics can

be explicitly given as

$$\mathrm{d}P = \frac{\mathrm{d}Q_{\mathrm{comb}} - \mathrm{d}Q_{\mathrm{ht}} - \frac{C_{\mathrm{v}}(T)+R}{R} p\mathrm{d}V}{\frac{C_{\mathrm{v}}(T)}{R} V} \tag{2.10}$$

Due to the opposed piston architecture of the engine, the change in volume is dependent on the dynamics of both the exhaust and intake crankshafts. This can be solved for explicitly from knowledge of the position and velocity of the crankshafts as

$$\mathrm{d}V = \frac{\mathrm{d}V}{\mathrm{d}\theta_{\mathrm{int}}}\omega_{\mathrm{int}} + \frac{\mathrm{d}V}{\mathrm{d}\theta_{\mathrm{exh}}}\omega_{\mathrm{exh}} \tag{2.11}$$

where volume and rate of volume change with respect to the crankshaft position can be derived from the engine properties given in Table 2.1.

Now, models for the gas property C_v, combustion Q_{comb}, and heat transfer Q_{ht} are provided. The constant volume specific heat, C_v, is estimated using the gas property model from Eriksson et al. [25] where

$$\begin{aligned} C_{\mathrm{v}}(\lambda,\tilde{T}) = \frac{1}{1000}(&l_1\lambda + 2l_2\lambda\tilde{T} + 2l_3\lambda^2\tilde{T} + \\ &c_1 + 2c_2\tilde{T} + 3c_3\tilde{T}^2 + 4c_4\tilde{T}^3 + 5c_5\tilde{T}^4) \end{aligned} \tag{2.12}$$

where λ is the air to fuel equivalence ratio and $\tilde{T}$ is given as

$$\tilde{T} = \frac{T - 300}{1000} \tag{2.13}$$

with T in Kelvin calculated as

$$T = T_{\mathrm{pc}}\frac{pV}{p_{\mathrm{pc}}V_{\mathrm{pc}}}. \tag{2.14}$$

The pc subscript denotes port closing. The constant terms in Eqn. 2.12, are

c_1 = 8.26159·10^5	l_1 = -0.39486·10^5
c_2 = 1.65422·10^5	l_2 = -0.90978·10^5
c_3 = 1.02150·10^5	l_3 = 0.26322·10^5
c_4 = -0.85770·10^5	
c_5 = -0.21236·10^5	

2.2.1.1 Heat Transfer

Heat transfer is assumed to occur purely through convection and is estimated using the Woschni correlation [41]. As such, the rate of heat transfer is given as

$$\mathrm{d}Q_{\mathrm{ht}} = h_{\mathrm{c}} A (T - T_{\mathrm{w}}). \tag{2.15}$$

where A is the surface area of the cylinder and can be calculated using the knowledge of cylinder geometry and piston position. The wall temperature, T_{w}, is held at a constant 450K. The coefficient h_{c} is obtained from the correlation

$$h_c = \frac{0.013 p^{0.8} \left(C_1 u_{\mathrm{p}} + \frac{C_2 (p - p_0) T_{\mathrm{pc}} V}{p_{\mathrm{pc}} V_{\mathrm{pc}}} \right)^{0.8}}{B^{0.2} T^{0.53}}. \tag{2.16}$$

The cylinder pressure, p, is in [Pa], p_0 is considered the motored pressure trace in [Pa] and can be estimated as an isotropic process. The mean charge temperature represented as T is in [K], and the mean piston speed u_{p} is in [m/s]. The coefficient C_1 has a unitless value of 2.28 and C_2 has a value of $3.24 \cdot 10^{-2}$ with units assumed to be [m/(s K)]. These values were tuned to match the GT-Power model in previous work to account for differences in the relative velocity of the boundaries in an OP engine due to the motion of two pistons [27]. The volume of the system, V, is in $[m^3]$ and any value with the subscripts pc are again reference conditions at port closing.

2.2.1.2 Combustion

The combustion process modeled here is based on experimental results from an Achates Power single cylinder OP engine utilizing gasoline compression ignition including sweeps of the speed, load, ECL, injection timing, and intake pressure. The values swept for each parameter are given in Tab. 2.2. The intake pressure sweep was only performed at SOI values of 12 degrees before minimum volume (bMV). A double injection strategy is used with a constant 38 degree split between the pilot and main injection. It is worth noting here that the crankshafts in experimentation were linked by a crankshaft, making the ECL a static parameter.

The heat release, modeled as a pilot and main heat release due to the split injection strategy implemented, is represented as

$$\mathrm{d}Q_{\mathrm{comb}} = (\beta \mathrm{d}x_{\mathrm{bp}} + (1 - \beta)\mathrm{d}x_{\mathrm{bm}}) m_{\mathrm{f}} Q_{\mathrm{LHV}}. \tag{2.17}$$

Table 2.2: Swept parameters for the geared OP engine experiments used to fit the heat release and ignition delay models

Parameter	Swept Values
Speed [RPM]	1600, 1800, 2000
Brake Power [kW]	20, 35
ECL [deg]	0, 4, 8, 12
SOI [deg bMV]	10, 11, 12, 13, 14
Intake Pressure [bar]	1.9, 2, 2.1, 2.2

The rate of heat release is made up of the pilot and main rates, represented as $\mathrm{d}x_{\mathrm{bp}}$ and $\mathrm{d}x_{\mathrm{bm}}$ respectively. The fraction of heat released in the pilot combustion process is represented as β and is dependent upon the engine setpoint as well as the trapped conditions. Using the experimental results discussed, the value of β was determined for each setpoint given a double Wiebe approximation for the heat release. Then, a linear function for β was determined using a forward step-wise regression over all the swept parameters. This ensures there is an appreciable linear relationship between the predictor, the swept variables, and the response variable β. The resulting function for β is

$$\beta = a_1 + a_2 ECL + a_3 N + a_4 L + a_5 \theta_{\mathrm{SOI}} + a_6 P_{\mathrm{ipc}} \tag{2.18}$$

where ECL is the exhaust crankshaft lead, N is the engine speed in [RPM], L is the load or power setpoint in [kW], θ_{SOI} is the start of injection timing in degrees, and P_{ipc} is the cylinder pressure in [bar] at intake port closing. All variables in this case were found to have a nonzero coefficient.

The magnitude of energy input is determined from the mass of the fuel, m_{f}, and the lower heating value of the fuel, Q_{LHV}. The $\mathrm{d}x_{\mathrm{bp}}$ and $\mathrm{d}x_{\mathrm{bm}}$ in this work are prescribed with the derivative of the well known Wiebe function [42]

$$\mathrm{d}x_{\mathrm{b}} = \frac{a(m+1)}{\Delta t}\left(\frac{t_{\mathrm{comb}} - t_{\mathrm{ign}}}{\Delta t}\right)^{m} e^{-a\left(\frac{t_{\mathrm{comb}} - t_{\mathrm{ign}}}{\Delta t}\right)^{m+1}}. \tag{2.19}$$

The value of a is used to fix the burn fraction x_b at the end of combustion and is set to $a = 6.908$ [42]. Equation 2.19 is calculated with respect to time to fix the combustion duration, Δt, independent of crankshaft position. As the velocity of the crankshafts can fluctuate, the assumption is made that the combustion duration will be with respect to time, not position. As with β, the variables of m and Δt are first fit to each experimental setpoint. For the fitting, a brute force methodology is used, comparing a range of possible

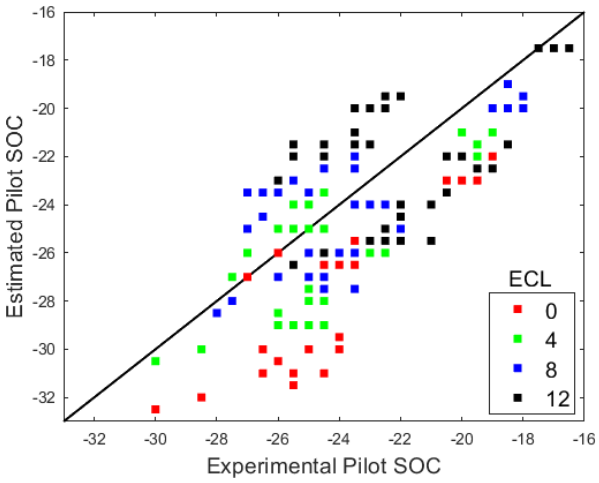

Figure 2.4: Parity plot comparing the estimated and measured start of combustion for the experimental data set used to tune the ignition delay model. The points are colored according the the ECL setpoint. Good agreement is shown between experimentation and estimated pilot SOC, with a maximum error of 6 degrees.

m and Δt values and selecting the best fit. Then, both variables are regressed over all the experimental values using the same forward step-wise regression technique to obtain linear approximations of Δt and m similar to Eqn. 2.18.

The value of t_{comb} is obtained from the state values defined in Eqn. 2.5 and will be the main or pilot heat release, depending on the phase of the model. The value of t_{ign} for the main heat release is a function only of the main injection timing as combustion of the pilot injection has already started. To find the start of combustion for the pilot injection, an ignition delay correlation with an Arrhenius form was adapted from Zhou et al. [43] and has the form

$$\tau = 2.5 * 10^{-3} p^{-5} \phi_{\text{pilot}}^{-3} \chi_{0_2}^{-1.41} exp\left(\frac{E_{\text{a}}}{RT}\right) \tag{2.20}$$

where p is the pressure in bar, ϕ_{pilot} is the fresh air equivalence ratio after the pilot injection, χ_{0_2} is the oxygen molar percentage, set to 21%, the activation energy E_{a} is coupled with the gas constant R and set to $\frac{E_{\text{a}}}{R} = 8198K$, and T is temperature of the charge. This correlation is used to provide the ignition delay for the Livengood, Wu integral [44]

$$AI = \int_{t_0}^{t_1} \frac{\mathrm{d}t}{\tau} \tag{2.21}$$

When the auto-ignition integral value reaches 1, t_1 is considered to be t_{ign}. A comparison between the estimated and actual start of combustion for the pilot injection is shown in Figure 2.4 with the color of each point denoting the ECL for that point.

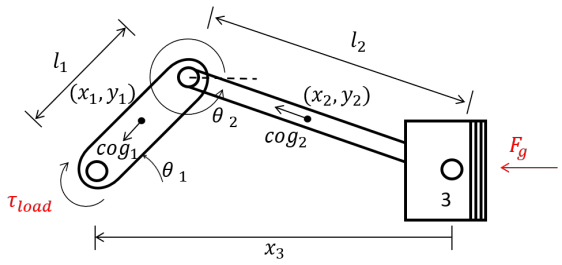

Figure 2.5: Configuration of the crank slider with inputs highlighted in red.

2.2.2 Crankshaft Dynamics

Each crankshaft has an individual trajectory while the pressure is assumed to be identical on each piston and is the only force coupling the two crankshafts. Here, equations for only a single crankshaft will be presented, but note the simulation contains two crankshaft models.

The electric motor is used to supply the load torque to the engine and control the crankshaft to the desired motion through what will be considered here as a rigid coupling. A positive motor torque, T_{m}, denotes work extraction from the engine. The motor shaft and crankshaft dynamics are then given as

$$J\alpha = T_{\mathrm{eng}} - T_{\mathrm{m}} \tag{2.22}$$

where α is the motor shaft and engine acceleration and J is the combined rotational inertia of the motor and crankshaft. To calculate the motion resulting from the balance between cylinder pressure creating the engine torque, T_{eng}, and the load torque, a crank slider mechanism is used, and a representation is given in Fig. 2.5. The crankshaft converts the gas force in the cylinder to torque at the crankshaft which the motor extracts as work. The mechanism here was modeled using the dynamics given by Yar et al. [40] where the motion of the crankshaft is described as

$$m_1\ddot{x}_1 + \lambda_1 = 0 \tag{2.23a}$$

$$m_1\ddot{y}_1 + \lambda_2 = 0 \tag{2.23b}$$

$$\begin{aligned} J_1\alpha_1 + \lambda_1\left(\frac{l_1}{2} - cog_1\right)\sin\theta_1 - \lambda_2\left(\frac{l_1}{2} - cog_1\right)\cos\theta_1 + \\ \lambda_3 l_1 \sin\theta_1 - \lambda_4 l_1 \cos\theta_1 - \lambda_5 l_1 \sin\theta_1 + \lambda_6 l_1 \cos\theta_1 = T_{eng} \end{aligned} \tag{2.23c}$$

and the motion of the connecting rod is described as

$$m_2\ddot{x}_2 + \lambda_3 = 0 \tag{2.24a}$$

$$m_2\ddot{y}_2 + \lambda_4 = 0 \tag{2.24b}$$

$$\begin{aligned} J_2\alpha_2 + \lambda_3\left(\frac{l_2}{2} - cog_2\right)\sin\theta_2 - \lambda_4\left(\frac{l_2}{2} - cog_2\right)\cos\theta_2 + \\ \lambda_5 l_2\sin\theta_2 + \lambda_6 l_2\cos\theta_2 = 0 \end{aligned} \tag{2.24c}$$

The rotational inertia of each component about its axis of rotation is denoted as J, l_1 is the crank radius, l_2 is the connecting rod length, and the *cog* term refers to the distance between the center of gravity and the center point of the crankshaft and connecting rod, (x_1, y_1) and (x_2, y_2), respectively. The angular position of the crankshaft and connecting rod are represented as θ_1 and θ_2 with the acceleration of each given as α. Note, the torque due to bearing or piston ring friction is neglected. The piston motion is described as

$$-m_3\ddot{x}_3 + \lambda_5 = F_{\text{gas}} \tag{2.25}$$

where m_3 is the mass of the piston and x_3 is the distance of the piston from the crank axis. F_{gas} is the gas force calculated using cylinder pressure and the piston surface area. The Lagrangian multipliers λ_i, $i = 1, 2, ..., 6$ can be replaced using six kinematic constraints of the crank slider mechanism, as shown in Eqn. 2.26, which limit the crank slider to 1 degree of freedom. A second order differential equation for θ_1 can then be obtained to model the state of crankshaft position. The full derivation of these terms can be found elsewhere [40].

$$x_1 - \frac{l_1}{2}\cos\theta_1 = 0 \tag{2.26a}$$

$$y_1 - \frac{l_1}{2}\sin\theta_1 = 0 \tag{2.26b}$$

$$x_2 - \left(l_1\cos\theta_1 + \frac{l_2}{2}\cos\theta_2\right) = 0 \tag{2.26c}$$

$$y_2 - \left(l_1\sin\theta_1 + \frac{l_2}{2}\sin\theta_2\right) = 0 \tag{2.26d}$$

$$-x_3 + l_1\cos\theta_1 + l_2\cos\theta_2 = 0 \tag{2.26e}$$

$$l_1\sin\theta_1 + l_2\sin\theta_2 = 0 \tag{2.26f}$$

Then, the value of crankshaft velocity, defined by the state value ω can be obtained by directly differentiating θ_1. By combining the thermodynamic and kinematic models

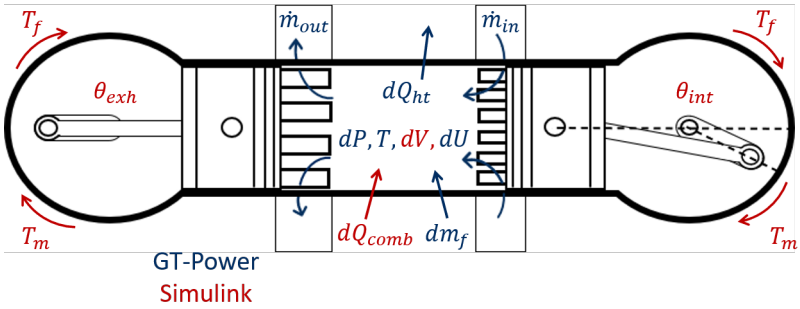

Figure 2.6: Representation of a uniflow scavenged OP engine detailing the source of each modeling subsystem term.

provided in the previous sections, state values θ, ω, P, and AI defined in Eqn. 2.5 can be calculated for use in the numerical optimization procedure presented in this thesis.

2.3 High Fidelity Modeling

As stated previously, a GT-Power model [39] is used to capture the 1D manifold gas dynamics, scavenging and port flow results, heat transfer, and other details required for an accurate engine simulation. However, capturing the instantaneous crankshaft dynamics for two independent crankshafts is difficult in this framework. As our application is structured around decoupled motion of the two crankshafts, the dynamics are modeled in a separate yet parallel simulation. The crankshaft motion is calculated using a model in Matlab/Simulink using the pressure from GT-Power and the control torque from the electric motors. This co-simulation also allows for the use of the same combustion model fitted to experimental results to be implemented in Matlab/Simulink with the signal sent to GT-Power for the pressure modeling. Figure 2.6 identifies the source of each modeling term within the high fidelity model. The following sections provide a description for the relevant subsystems modeled in GT-Power. The subsystems contained in Simulink are identical to the models used for the optimization problem modeling defined previously.

2.3.1 Open Cycle Breathing

A GT-Power model using inlet flowrate and exhaust back pressure as the boundary conditions was used to capture the 1D gas dynamics, port flow behavior, and scavenging performance of a single cylinder OP engine. The model contains the intake and exhaust plenum volume as well as individual connections for each port in the cylinder wall. A position dependent lookup table of port areas is used to quantify the cross sectional flow

area according to port geometry. A more detailed description of the experimental engine setup used to validate the model has been published elsewhere [15].

The most significant contribution of this portion of the model is the quantification of the scavenging performance. This allows for an accurate estimate of the concentration of fresh air and residuals within the cylinder when the ports close. As detailed in Regner et al. [15], a correlation between scavenging ratio and scavenging efficiency was determined experimentally using in-cylinder sampling of CO_2. Consider the scavenging ratio defined as

$$SR = \frac{\text{mass of air delivered}}{\text{mass of trapped cylinder charge}} \tag{2.27}$$

and the scavenging efficiency as

$$\eta_{\text{sc}} = \frac{\text{mass of delivered air retained}}{\text{mass of trapped cylinder charge}} \,. \tag{2.28}$$

The scavenging ratio can be calculated directly from the modeled flow through the intake and exhaust ports. The scavenging efficiency, obtained from the experimental correlation, can be used to determine the cylinder residual ratio as scavenging efficiency is a measure of how effectively the delivered air replaces the burned gases in the cylinder.

Thermodynamic Model

As the GT-Power model is responsible for providing the cylinder pressure calculation, we introduce the pertinent variables with the first law of thermodynamics, written as

$$\mathrm{d}U = -\mathrm{d}Q_{\text{ht}} - \mathrm{d}W + \mathrm{d}m_{\text{f}} h_{\text{f}} \tag{2.29}$$

where the derivatives are with respect to time. Note the only mass flow considered here is the fuel injection and the corresponding enthalpy is given by $\mathrm{d}m_{\text{f}}$ and h_{f} as this defines only the closed portion of the engine cycle. The change in internal energy is denoted by dU and heat transfer as dQ_{ht}. Work extracted from the system, represented as dW, is equal to

$$\mathrm{d}W = p\mathrm{d}V \tag{2.30}$$

As fuel is the only mass flow in the system, we can expand $\mathrm{d}U = \mathrm{d}m_{\text{f}} u + \mathrm{d}u m_{\text{f}}$. By representing the internal energy as the sum of chemical and sensible components, $u = u_{\text{c}} + u_{\text{s}}$, heat addition due to combustion be introduced as

$$\mathrm{d}Q_{\text{comb}} = m_{\text{f}} \mathrm{d}u_{\text{c}} \tag{2.31}$$

Using Eqns. 2.30 and 2.31 in Eqn. 2.29 we obtain

$$\mathrm{d}Q_{comb} - \mathrm{d}Q_{ht} = p\mathrm{d}V + \mathrm{d}m_f(u_s - h_f) + m_f\mathrm{d}u_s \tag{2.32}$$

from which we can derive the pressure dynamics that drive the engine crankshaft. For the sake of brevity, this derivation is not included here as the variable of pressure is given explicitly from GT-Power. However, it is relevant to note the source of the heat transfer term. Heat transfer is estimated using the Woschni correlation and this term is provided by GT-Power [41]. The convection multiplier is scaled in the formulation to account for the relative velocity of the boundaries in an OP engine being twice that of a conventional engine operating at the same average RPM.

The combustion event is modeled in the Matlab/Simulink environment using the same fitted model as provided in Section 2.2 and the mass fraction burned value is used in GT-Power as an input. Similarly, the crankshaft dynamics supplying the cylinder volume and crankshaft torque in the Simulink model are previously defined in Section 2.2.

2.4 Optimal Control Problem Solutions

2.4.1 Comparison of Loss Mechanisms

Using the optimization methods as modeling presented above, the baseline case of a nominally 0 degree ECL, 1600 RPM average speed setpoint, and a constant fueling rate of 78 mg per cycle is investigated. The brake thermal efficiency (BTE) of the system is defined as in Eqn. 2.1 and the indicated thermal efficiency (ITE) is defined as

$$\eta_{\mathrm{i}} = \frac{\int_{-\pi}^{\pi} P\mathrm{d}V}{m_{\mathrm{f}}Q_{\mathrm{LHV}}} \tag{2.33}$$

where P is the cylinder pressure and V is the cylinder volume. The integral is the complete two stroke cycle as this refers to the net indicated efficiency. In the following discussion, the efficiency values are calculated from the results of the high-fidelity simulation rather than the optimization model, meaning they will include the effects of system losses whether or not the optimization model accounts for them. Further, trajectories are typically shown with respect to degrees aMV.

Shown in Figure 2.7 are the optimal trajectories for a lossless case, a case considering the heat transfer losses of the OP engine (Q_{ht}), and a case considering both the heat transfer losses as well as the electrical losses of the motor extracting the work from the engine (P_{ML}). It is first interesting to consider the ideal case, meaning no losses from the engine

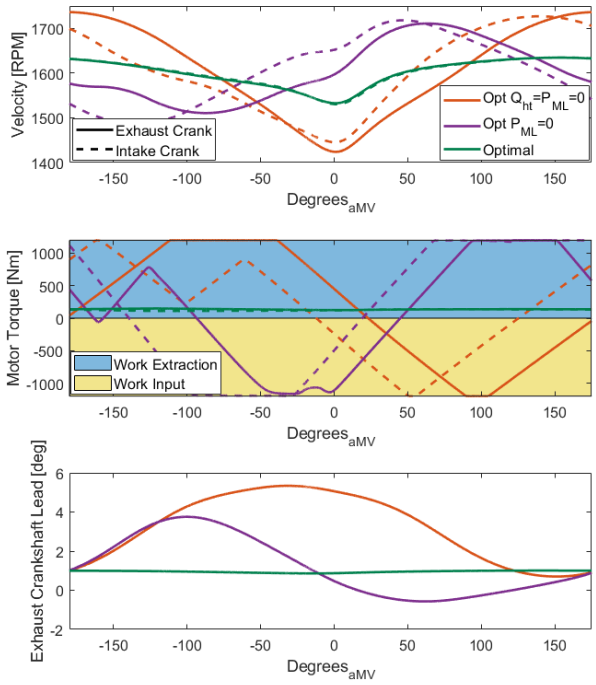

Figure 2.7: Optimal trajectories of the engine cycle.Top to bottom: crankshaft velocity, motor torque, exhaust crankshaft lead. Results from a lossless case (red), a case including heat transfer (purple), and the optimal case considering both heat transfer and motor losses (green) are provided for each subfigure, illustrating the impact of the individual losses.

or motor are included in the optimization problem with heat transfer and the motor loss set to zero. For both crankshafts in this case, the minimum velocity is near minimum volume. The motor input torque during the compression stroke is positive, indicating the decrease in velocity is not only due to the increase in cylinder pressure, but the motor is also extracting work from the system. For a lossless optimization case, these results are expected as the relatively longer time near minimum volume due to the lower crankshaft velocity shifts the combustion regime closer to a constant volume approximation. This also increases the pressure at minimum volume as shown in the pressure-volume plot from the high-fidelity model given in Figure 2.8. This higher pressure in turn increases the peak temperature and thus the work output of the cycle, if considering an ideal cycle.

The ECL trajectory, conversely, is slightly counter-intuitive. An ECL of 0 degrees would produce the smallest minimum volume possible for the engine, increasing the compression ratio. Despite this, the ECL is approximately 5 degrees at minimum volume, which is an increase of about 0.95cm^3 for the miminum volume compared to a 0 degree

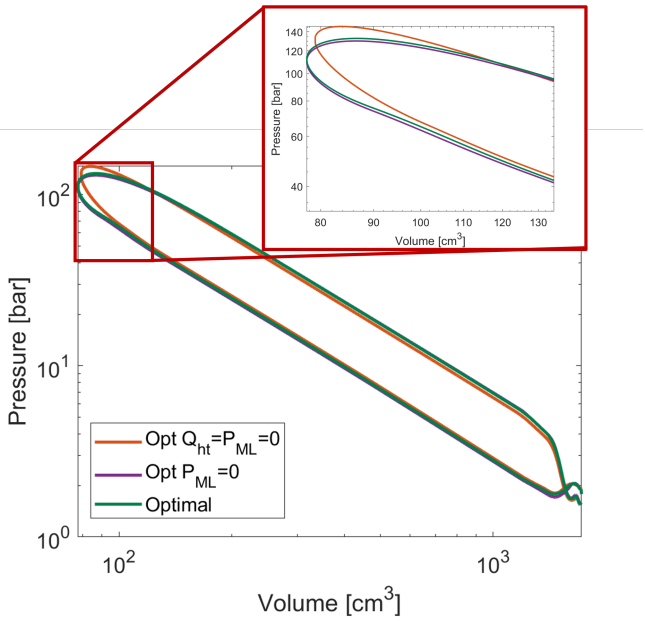

Figure 2.8: Cylinder pressure with respect to volume for multiple optimization cases. After introducing heat transfer to the optimal control problem, peak cylinder pressure is significantly reduced to lower in cylinder temperatures.

Table 2.3: Indicated and brake thermal efficiency for optimization cases

	ITE [%]	BTE [%]
OPT $Q_{\text{ht}} = P_{\text{ML}} = 0$	46.9	4.1
OPT $P_{\text{ML}} = 0$	49.1	1.8
Optimal	48.6	45.1

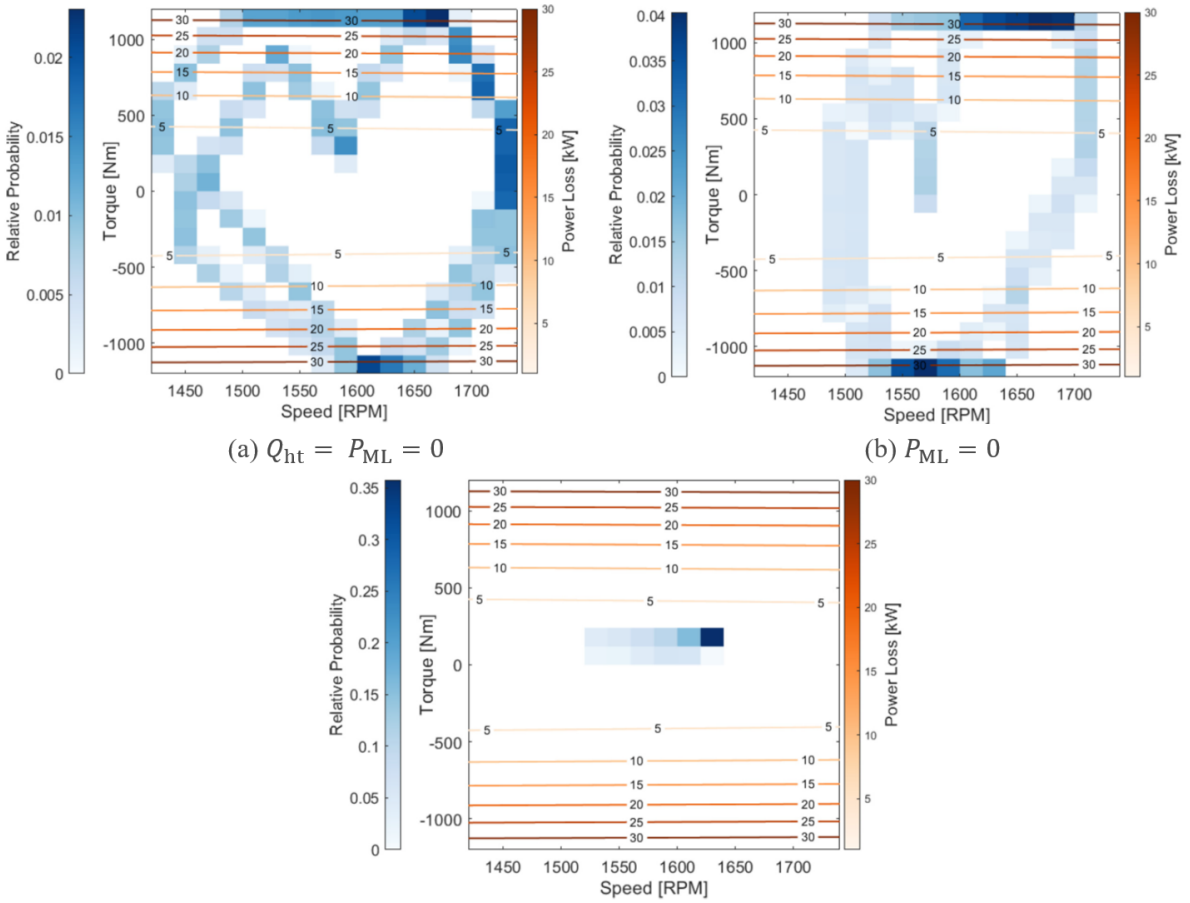

Figure 2.9: Distribution of torque and speed operating points for trajectory optimization case with the respective power loss overlaid. By introducing motor losses, the range of motor torque values is drastically reduced to improve the work extraction efficiency of the system. This can be seen by comparing the reduced range of torques for the optimal case in subplot c. (a) $Q_{ht} = P_{ML} = 0$, (b) $P_{ML} = 0$, and (c) optimal

ECL setpoint. However, due to the offset nature of the intake and exhaust ports where the intake port closes before the exhaust ports, an ECL of around 4 degrees increases the trapped volume of the engine by 21.26 cm^3 compared to a 0 degree ECL case. While the motor input to the system could reduce the ECL as the pistons approach minimum volume, this would require speeding up the exhaust crankshaft and reducing the residence time of the pistons near minimum volume. During expansion, the ECL goes to 0, increasing the expansion ratio, similar to an Atkinson cycle.

Despite all of the intended thermodynamic improvements from the optimized motion profile, the results from the high-fidelity simulation in Table 2.3 for the ideal case where $Q_{\text{ht}} = P_{\text{ML}} = 0$ show the ITE result is the lowest of the three cases investigated. The

increase in peak pressure and temperature that improve the ideal cycle efficiency actually decrease the ITE for the simulation due to increased heat transfer losses. When including heat transfer in the optimization process, the resulting torque profile is nearly a reflection of the lossless torque profile over the x-axis. As the pistons approach minimum volume, the motors put work into the system to increase the velocity past minimum volume. As shown in Fig. 2.8, the case with only heat transfer considered has the lowest peak pressure. This is similar to the findings of Eriksson et al. [25]. In their work, the reduction in peak pressure is achieved by extending the heat release profile in the crank angle domain. Here, the $\Delta\theta$ over which the heat release takes place is not directly controllable. Instead, increasing the crankshaft velocity effectively increases $\Delta\theta$, assuming the heat release profile in the time domain is relatively constant. As such, the results in Tab. 2.3 show the case considering only heat transfer losses to have the highest ITE.

However, for the cases of both $Q_{\text{ht}} = P_{\text{ML}} = 0$ and $P_{\text{ML}} = 0$, the BTE is near zero. The motor torque input for each case is a rough approximation of bang-bang control, switching between the minimum and maximum motor torque of $\pm$1200Nm. Noting that quadrature current, I, is approximately proportional to motor torque in Eqn. 2.3, operating at the peak torque values for the motor will be highly inefficient as the power loss is a function of I^2. Therefore, when including P_{ML} in the optimization problem, the operating regime moves toward constant torque control. As shown in Fig. 2.7, the optimal case, where both heat transfer and motor losses are considered, the motor torque remains close to 125 Nm the entire cycle and the velocity profile fluctuates naturally with the cylinder pressure. The ECL does not increase near port closing to increase the trapped volume, as this would require the motors to move away from the nominal operating torque. The impact of power losses from the motor on the optimal operating regime can be visualized in torque density plots for each case, shown in Fig. 2.9. While there is a decrease in ITE due to the longer residence time of the pistons near minimum volume, the optimal case shows motor efficiency to be the dominant factor when maximizing the system efficiency.

2.4.2 Exhaust Crankshaft Lead

From the previous results, it is clear that intra-cycle variation of the ECL through manipulation of the motor torque is severely detrimental to the motor efficiency, and therefore brake system efficiency. However, the optimal crankshaft motion profile at different ECL setpoints and the corresponding system efficiency is of interest as the ECL can still be varied between steady state operating points on an inter-cycle basis.

Using the optimal case structure from the previous section where both motor loss

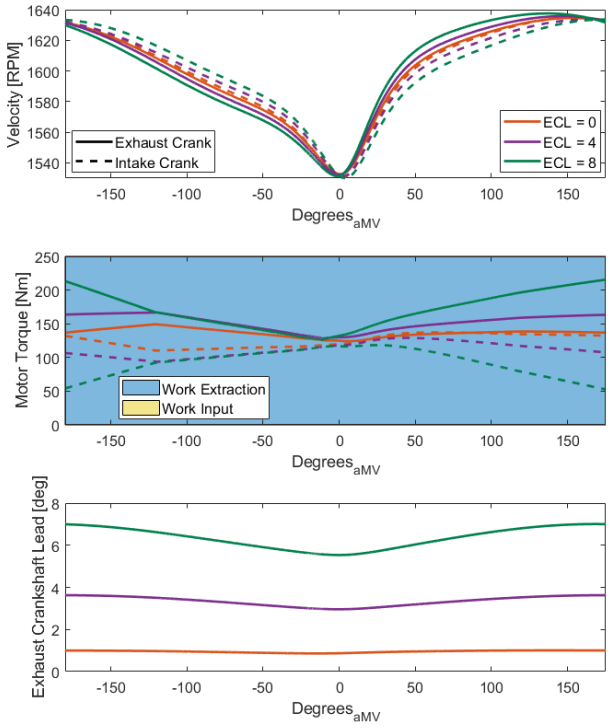

Figure 2.10: Optimal trajectories of the engine cycle for varying exhaust crankshaft lead setpoints at 1600 RPM. Top to bottom: crankshaft velocity, motor torque, exhaust crankshaft lead. At higher ECL initialization points, the ECL decreased during the compression stroke, but must increase during expansion to meet the continuity constrains for the engine cycle.

and heat transfer are considered in the system, ECL setpoints of 0, 4, and 8 degrees are investigated. It should be noted again that the ECL setpoint is implemented at the start of the trajectory, where $|\theta_{\text{exh}} - \theta_{\text{int}}| \leq ECL_{\text{lim}}$ where $ECL_{\text{lim}} = 1$ degree. Therefore, for example in the 8 degree ECL case, the optimal profile actually starts at an ECL of 7 degrees. The resulting crankshaft motion and torque trajectories are shown in Fig. 2.10. As expected, the motor torque required to produce the resulting crankshaft motion is relatively constant to reduce motor losses. However, as an ECL is introduced to the system, the proportion of energy extracted from the engine is no longer evenly split between the intake and exhaust crankshaft. Due to the exhaust crankshaft passing top dead center ahead of the intake crankshaft, more work is extracted by the exhaust motor as the ECL increases, as illustrated in the motor torque shown in Fig. 2.10.

From the efficiency results given in Tab. 2.4, the ECL setpoint of 0 degrees again shows the highest ITE and BTE. This is also reflected in the ECL profiles for the higher ECL

Table 2.4: Indicated and brake thermal efficiency for sweep of exhaust crankshaft lead at 1600 RPM

	ITE [%]	BTE [%]
ECL = 0	48.8	45.1
ECL = 4	48.3	44.8
ECL = 8	47.7	44.2

Table 2.5: Indicated and brake thermal efficiency for sweep of exhaust crankshaft lead at 2000 RPM

	ITE [%]	BTE [%]
ECL = 0	47.5	42.2
ECL = 4	47.6	42.5
ECL = 8	47.2	42.1

cases, where the ECL decreases toward minimum volume to increase the compression ratio. However, as the final ECL must meet the initial condition for the cyclic process, the ECL must increase again during expansion, reducing the expansion ratio of the engine.

While the 0 degree ECL case does maintain a higher BTE than the other two cases, the margin is less than 0.4% BTE. Further, as the engine speed setpoint is increased, this margin is reduced, and the 4 degree ECL case in fact achieves a higher BTE, as shown in Tab. 2.5. At the higher speed setpoint, the blowdown process becomes more influential as the time the engine has to replace the burned gasses with fresh air is reduced. Therefore, as speed increases, the trapped temperature at port closing increases for the 0 degree ECL case, resulting in higher cylinder temperatures and increased heat transfer.

However, what is not captured in this optimization framework is the air handling system. In an OP engine, the scavenging process is largely controlled by the exhaust crankshaft lead and pressure ratio between intake and exhaust manifold as the pistons are decoupled from the pumping process. Thus, a compressor upstream of the engine, whether that is in the form of a supercharger or turbocharger, must supply boost pressure to meet the airflow demands of the engine operating point. Therefore, if changing the ECL has little impact on the thermodynamic efficiency, benefits in the form of reduced pumping losses, coupled with a reduced trapped cylinder temperature, may be obtained by increasing ECL and reducing the boost pressure required to meet the airflow demands at high power or speed setpoints.

2.5 Conclusions

The optimal control of the crankshaft motion for an OP engine in a novel hybrid architecture is investigated in this Chapter. To adequately capture the gas exchange process, an iterative optimization technique was utilized, using a high-fidelity simulation to provide the boundary conditions of trapped pressure, temperature, and charge mass to the numerical optimization problem. The optimization problem was then constructed as five sequential phases including intake, compression, pilot heat release, main heat release and expansion, as well as exhaust processes. Direct collocation and a Gauss Psuedo-Spectral method are used to reduce the optimization problem to a finite dimensional problem which can then be solved using an interior points method.

The results from this optimization process show indicated thermodynamic benefits can be achieved through manipulation of the crankshaft velocity with the torque of the electric motors. However, these improvements in ITE come at a high cost in motor efficiency. When the efficiency of work extraction is neglected during the trajectory optimization, the BTE is near 0%.

With the elimination of the conventional geartrain linking the two OP engine crankshafts, the ECL can also be dynamically varied during engine operation. The motor losses incurred from the large torque input required to alter the ECL over a single cycle limit the practicality of large changes in ECL during a single cycle. However, when engine speed and power setpoints are increased, increasing the ECL to reduce pumping losses and trapped cylinder temperature can provide provide a system level efficiency increase.

The following chapter will define the position controller used to regulate the position of each crankshaft, experimentally verify the control algorithm, and compare the experimental results with the modeling results for a given trajectory. The purpose is to investigate the performance of the optimal crankshaft motion references derived in this chapter on an experimental engine.

CHAPTER 3

Control Design, Implementation, and Experimental Validation of a Hybrid OP Engine

In this Chapter, the position control architecture used to regulate the motion of the two independent OP engine crankshafts is introduced. Experimental validation of the controller and proof of concept for the entire hybrid OP engine architecture is then provided with a comparison to the modeled results for identical operating points. This comparison reveals the significant sensitivity to model uncertainty due to high cylinder pressure and the reversal of piston motion near minimum volume of the engine. To evaluate the feasibility of this proposed architecture and further evaluate the integration of the electric machines with the OP engine, detailed electrical loss simulations were used to compare this dual motor design to a single motor design which includes a geartrain to link the two crankshafts. While the single motor design presents a more robust system design, the dual motor design is capable of higher maximum system efficiencies. This peak efficiency, however, is highly dependent on the electric machine operation.

3.1 Position Regulator

In a single cylinder engine, significant crankshaft velocity fluctuations are expected over a single cycle [45]. Therefore, to maintain the stability of this system and track the desired crankshaft motion trajectory, a feedback controller is designed with an additional feedforward estimation of the motor torque to provide the instantaneous torque demand to the electric motors. This control design assumes measurements of cylinder pressure and crankshaft position are available. The velocity and position tracking references are supplied in lookup tables with cycle time as the independent variable. This tracking reference is derived from the work in Chapter 2. It is important to note here that a constant speed and load setpoint refers to the average speed and power over a cycle. However, as

noted previously, the instantaneous engine speed and torque will fluctuate with the cylinder pressure and motor torque applied to the crank slider mechanism. The demanded motor torque input, u_{m}, can therefore be given as

$$u_{\mathrm{m}} = u_{\mathrm{feedback}} + u_{\mathrm{feedforward}} \tag{3.1}$$

where each of these components are described in the following sections. A field-oriented controller [46] is used to regulate the motor torque. Further discussion of this low level controller is outside the scope of this work.

3.1.1 Feedback Control

A discrete time linear quadratic regulator (LQR) is used for the feedback control. The states for this controller are given as $x = [\theta_{exh}\ \theta_{int}\ \omega_{exh}\ \omega_{int}]^T$ where ω represents rotational velocity and the inputs are $u = [T_{m_{exh}}\ T_{m_{int}}]^T$ with the subscripts of exh and int denoting the exhaust and intake crankshafts. The discrete control model used is shown below. The feedback model is a set of double integrators used to represent the crankshaft motion with motor torque as the input.

$$\begin{aligned} x_{k+1} &= \underbrace{\begin{bmatrix} 1 & 0 & \Delta t & 0 \\ 0 & 1 & 0 & \Delta t \\ 0 & 0 & 1 & 0 \\ 0 & 0 & 0 & 1 \end{bmatrix}}_{A} x_k + \underbrace{\begin{bmatrix} 0 & 0 \\ 0 & 0 \\ \frac{\Delta t}{J} & 0 \\ 0 & \frac{\Delta t}{J} \end{bmatrix}}_{B} u_k \\ y_k &= \underbrace{\begin{bmatrix} 1 & 0 & 0 & 0 \\ 0 & 1 & 0 & 0 \end{bmatrix}}_{C} x_k \end{aligned} \tag{3.2}$$

However, as the goal is for $Cx_k \to r$ where r is the reference, a new set of variables are defined as

$$\begin{aligned} \zeta_k &= x_k - x_{k-1} \\ e_{k+1} &= Cx_k - r = C\zeta_k + e_k \end{aligned} \tag{3.3}$$

where e denotes the position tracking error. Note, in the following derivation r is assumed constant. In practical applications however, it can vary with time and indeed does later in this work. With these new variables, an augmented system with the state and error

dynamics can be given as

$$\begin{bmatrix} \zeta_{k+1} \\ e_{k+1} \end{bmatrix} = \begin{bmatrix} A & 0 \\ C & I \end{bmatrix} \begin{bmatrix} \zeta_k \\ e_k \end{bmatrix} + \begin{bmatrix} B \\ 0 \end{bmatrix} (u_k - u_{k-1}) \tag{3.4}$$

Consider a control law for this system to be

$$u_k - u_{k-1} = K \begin{bmatrix} \zeta_k \\ e_k \end{bmatrix} \tag{3.5}$$

where the feedback gain K can be calculated using LQR control design with an infinite horizon. The cost function is defined as

$$J = \sum_{k=0}^{\infty} e_k^T Q e_k + \Delta u_k^T R \Delta u_k \tag{3.6}$$

where Q and R are positive semi-definite and positive definite matrices, respectively, used for tuning the controller. The control law can now be given as

$$u_k = u_{k-1} + K_1(x_k - x_{k-1}) + K_2 e_k \tag{3.7}$$

assuming a decomposition of K following Eqn. 3.5. Substituting in the control expression for values of u_{k-n} for $n = 1, .., k$, the feedback control simplifies to

$$u_{fb} = u_k = u_0 + K_1(x_k - x_0) + K_2 \sum_{i=1}^{k} e_i \tag{3.8}$$

To track a time varying trajectory as mentioned previously, x_0 is replaced with x_r.

3.1.2 Feedforward Control

To account for the engine torque's impact on crankshaft dynamics and provide a faster response to the tracking demand, a feedforward estimate of the required motor torque is calculated, u_{ff}. Here the effect of the torsional crankshaft coupler is neglected as the natural frequency of the coupler is well above the controller bandwidth. The motor torque can then be estimated directly through the torque balance

$$u_{\text{ff}} = \hat{T}_{\text{m}} = \hat{T}_{\text{eng}} - J\alpha_k \tag{3.9}$$

where J is the rotational inertia of the flywheel, shaft coupling system, and electric motor and α_k is the acceleration of the crankshaft at that sample point. The desired acceleration can easily be obtained from differentiation of the velocity trajectory. The engine torque, T_{eng}, can be calculated using Eqns. 2.23 through 2.25. As Eqn. (2.25) contains the gas force calculated from cylinder pressure and piston surface area, the feedforward term can adapt to fired or motored traces using the in-cylinder pressure measurements.

3.2 Experimental Validation for Control and Optimization Process

To validate the engine model and optimization process constructed in Chapter 2 as well as the controller developed for the crankshaft motion, simulation predictions of steady state operating points were compared to experimental data. The experimental engine used in this study was provided by Achates Power and the specifications are listed on Tab. 2.1. A gasoline compression ignition strategy using pump gasoline with an 87 anti-knock index was used for this testing. A split injection strategy consisting of a pilot injection 38 degrees advanced from the main injection identical to the strategy used for creating the combustion model detailed in Chapter 2 was adopted. Each crankshaft was coupled to an Avid AF240 axial flux surface mount permanent magnet (SMPM) motor/generator with Semikron SKiiP 1814 GB17E4-3DUW V2 switching units for the inverter. An HBM T40B torque transducer was mounted inline with the shaft coupler for the electric machine and engine crankshaft to provide instantaneous torque measurements for model validation. An image of the engine and motors installed in the test cell is shown below in Fig. 3.1(a) and Tab. 3.1 details the relevant electric machine parameters of the AF240s used.

An external air handling system as well as an external oil and coolant system are used to maintain relevant operating conditions for the hybrid system. Air is supplied by an external screw type compressor which maintains a 250 gallon air tank to the desired reservoir pressure (350 kPa). This then feeds the conditioning system consisting of a 20 kW air heater, and a pressure regulation valve as shown in Fig. 3.1(b). The engine intake air pressure at the intake plenum is controlled via the pressure regulation valve to a value of 2 bar while the intake air temperature is maintained at 50°C, or 323 K for all tests. Air flow through the engine is controlled with the exhaust throttle valve.

To implement the control strategy, an AVL GH14D pressure sensor was used to measure the cylinder pressure and a Heidenhain ROD 420 TTL quadrature encoder with 720 lines was used measure each crankshaft position. The initial experimental and modeling results

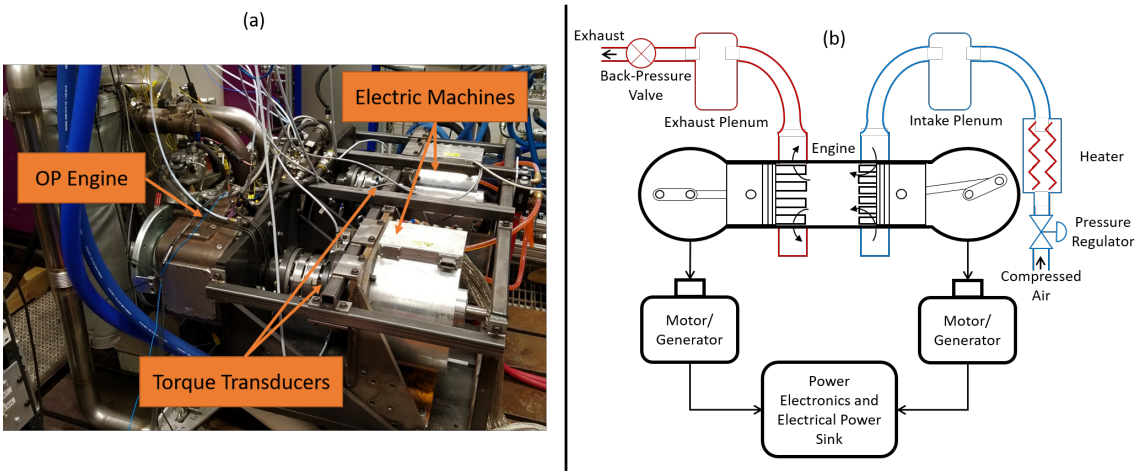

Figure 3.1: (a) Gearless series hybrid OP engine design installed in the test cell. Torque transducers are installed inline with each crankshaft between the engine and electric machines to validate the estimated engine torque produced by the engine and input by the electric machines. (b) Layout of the experimental testcell including the air handling system.

Table 3.1: Electric Machine Parameters

Parameter	Value
Maximum Speed	5000 RPM
Peak Torque	$\pm$1200 Nm
Nominal Power	188 kW

were compared at an operating setpoint of 1600 rpm, a constant fueling rate generating approximately 35kW of power, measured at the engine crankshafts, and an exhaust crankshaft lead of approximately 0 degrees. The mass flow rate of air through the engine as well as the injection quantity and timing in the model are set to match the experimental values. As single engine cycles are being compared for the intra-cycle dynamics, it is relevant to note that the coefficient of variation for the indicated mean effective pressure was approximately 1% for the setpoint being analyzed.

Figure 3.2 presents the apparent heat release rate and cylinder pressure around minimum volume. The results are shown with respect to minimum volume as the independent crankshafts may not reach top dead center at the same time. The model captures the split between pilot and main heat release events well with the double Wiebe function used to represent the combustion process. However, the small premixed spike in the main heat release event is not captured in the modeled combustion event, leading to

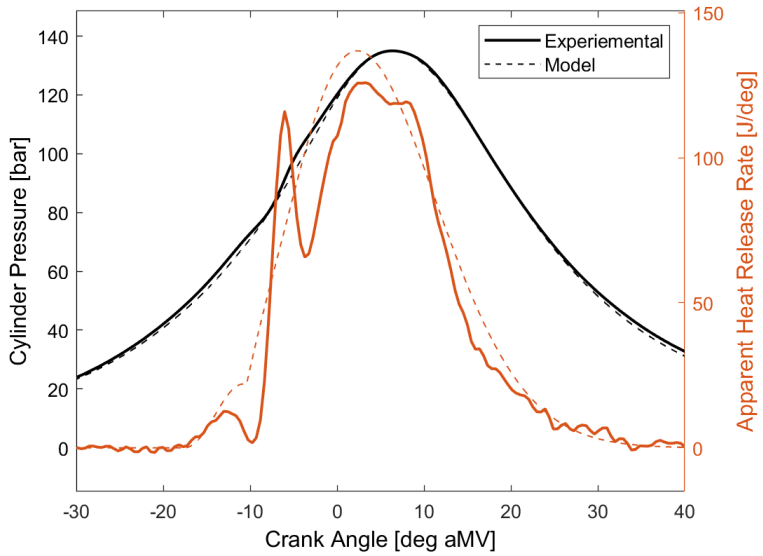

Figure 3.2: Apparent heat release and cylinder pressure profile for model and experiemntal results.

some small discrepancies in the pressure trace.

The advantage of the hybrid OP engine design is largely in the capability of independently regulating the crankshaft motion. Thus, the instantaneous crankshaft dynamics and tracking control capabilities are of great interest. The crankshaft rotational profile used as the controller reference for this initial validation is provided in Fig. 3.3 along with the resulting velocities for the model and experiment. This profile is a result of the optimization process defined in Chapter 2. The experimental velocity is filtered here using a cubic spline to remove the noise generated by differentiation. Note that this tracking profile has significant variation in instantaneous crankshaft velocity. As expressed in Eqn. 3.9, the amplitude of motor torque required to follow the desired motion trajectory is a function of the engine torque and crankshaft acceleration. If a constant velocity for the crankshaft trajectory was selected and perfect tracking was achieved, the acceleration would be zero and the instantaneous motor torque demand would be equal to that of the instantaneous torque generated by the engine. Filipi and Assanis [45] showed that the instantaneous torque of a single cylinder engine exhibits large fluctuations over an engine cycle. Further, the peak torque corresponds to the peak cylinder pressure during combustion. Therefore, the velocity profile used here is roughly a reflection of the pressure trace, reducing the demand on the electric motors. The velocity reference as well as the resulting velocity profile are shown in the top plot in Fig. 3.3 as well as the tracking error of the crankshaft position in the bottom plot for both the exhaust (exh) and intake (int) crankshafts. As the

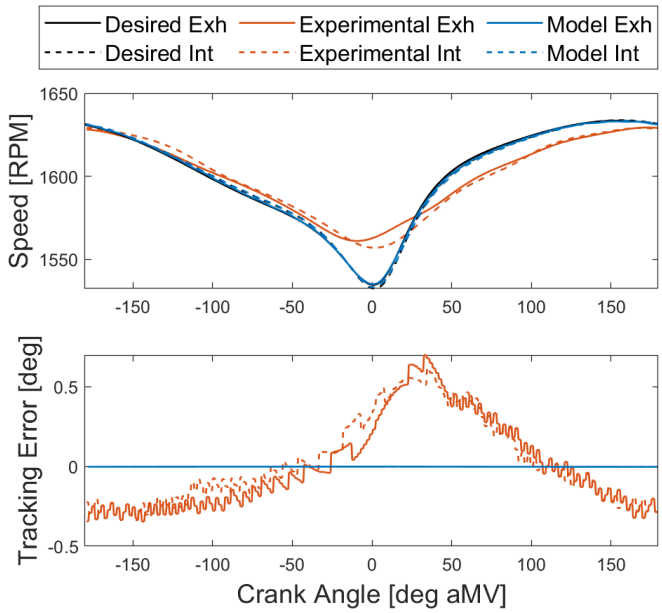

Figure 3.3: Rotational velocity of the exhaust (Exh) and intake (Int) crankshaft for the model and experimental results, including the shared reference and the positional tracking error.

tracking error is maintained within approximately ± 0.5 degrees for the crankshaft position, these results validate the proposed control architecture and the feasibility of controlling the motion of the OP engine crankshafts with electric motors.

However, it is important to note the increased velocity error near minimum volume for the experimental results, which is not present in the modeled results. From the difference in the velocity profile, it is apparent there are unmodeled dynamics resisting the change in velocity of the crankshaft. The modeled torque input as well as the raw experimental motor torque signal for both crankshafts are shown in Fig. 3.4. The modeling results can be considered the nominal torque profile required to track the given trajectory and the experimental profile is the result of disturbances and model uncertainty. As the pistons approach minimum volume, the combustion process begins and the cylinder pressure increases rapidly. The experimental velocity does not experience as dramatic of a decrease in velocity as the model. The motor torque spikes to extract more work from the engine and slow the crankshafts. Similarly, as the crankshafts pass minimum volume, the expected increase in velocity is largely damped in the experimental results, indicating a larger rotational inertia than in the model.

From the near 700 Nm discrepancy in motor torque around minimum volume and the difference in crankshaft velocity between modeled and experimental results, it is apparent

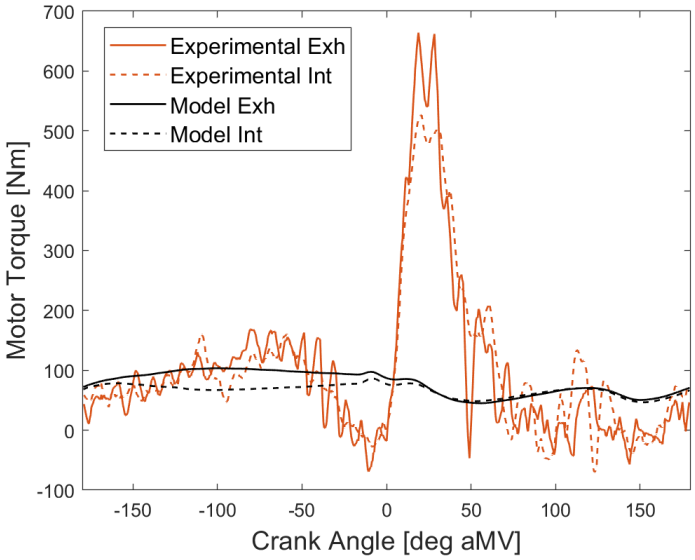

Figure 3.4: Instantaneous torque required to track the desired crankshaft motion profile.

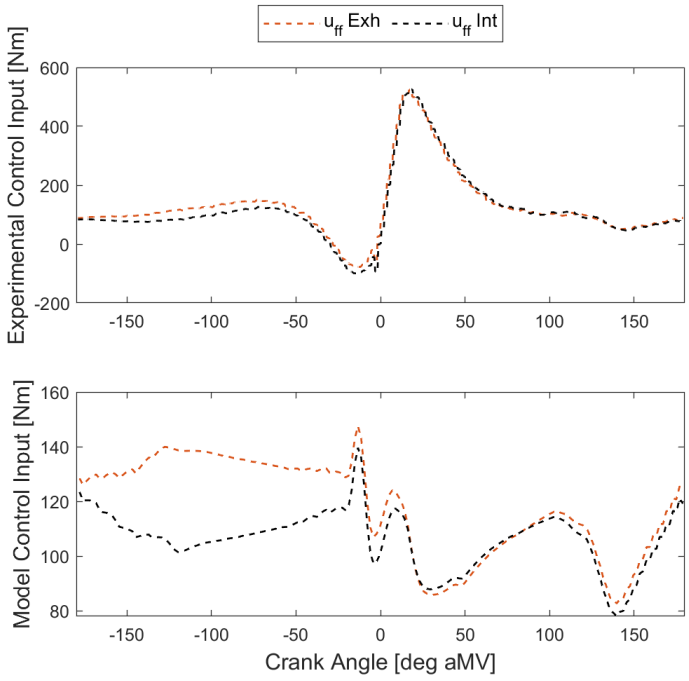

Figure 3.5: Feedforward control inputs for the experimental and modeling results.

there is parametric uncertainty in the system inertia. However, the discrepancy can also be attributed to differences in the cylinder pressure. Indeed, as the cylinder pressure increases, the system becomes ill-conditioned [34]. This means small variations in the system parameters or states can cause the control input to deviate significantly from the nominal value. As noted previously, the complex nature of the GCI combustion event was not completely captured in the modeled combustion event, leading to a small deviation in the cylinder pressure. The pressure trace shown in Fig. 3.2 exhibits a modest pressure error during compression and a smaller pressure rise rate after combustion in the modeled results due to the lack of a premixed spike in the modeled heat release. While these errors appear visually to be insignificant, the feedforward control terms, shown in Fig. 3.5, highlight the large impact on instantaneous motor torque that this error can have. Recall from Eqn. 3.9 that the feedforward term is simply an estimation of the motor torque required to balance the engine torque and follow the reference trajectory. As the reference trajectory is the same for both the experimental and modeled cases, the $J\alpha_k$ term will be identical. Similarly, the same parameters are used to estimate the engine torque in Eqns. 2.23 through 2.25. The large difference in the feedforward control shown in Fig. 3.5 is then generated purely from the position and pressure measurements used to make this estimate. Therefore, the small perturbations in cylinder pressure with respect to piston position have a remarkably large impact on the instantaneous engine torque generation and thus, the motor torque required to track a crankshaft motion profile.

The significant sensitivity of the experimental system to model uncertainty limits the effectiveness of a direct translation of offline optimization trajectories to online implementation. Further, the need to maintain crankshaft phasing requires position control over the entire cycle and prevents the use of simple speed control with inter-cycle torque control updates to smooth the torque profile. Therefore, future chapters will develop a method of defining optimal crankshaft motion trajectories during engine operation, eliminating the model uncertainty from the optimization process. However, it is first important to evaluate the theoretical performance benefits even possible with this dual motor controlled OP engine design. Therefore, utilizing experimental results from this section combined with detailed electric machine simulations, a parametric study of motor and engine characteristics was conducted to project the efficiency potential of this dual motor controlled hybrid OP engine design compared to a hybrid OP engine design that retains the conventional geartrain linking the two crankshafts.

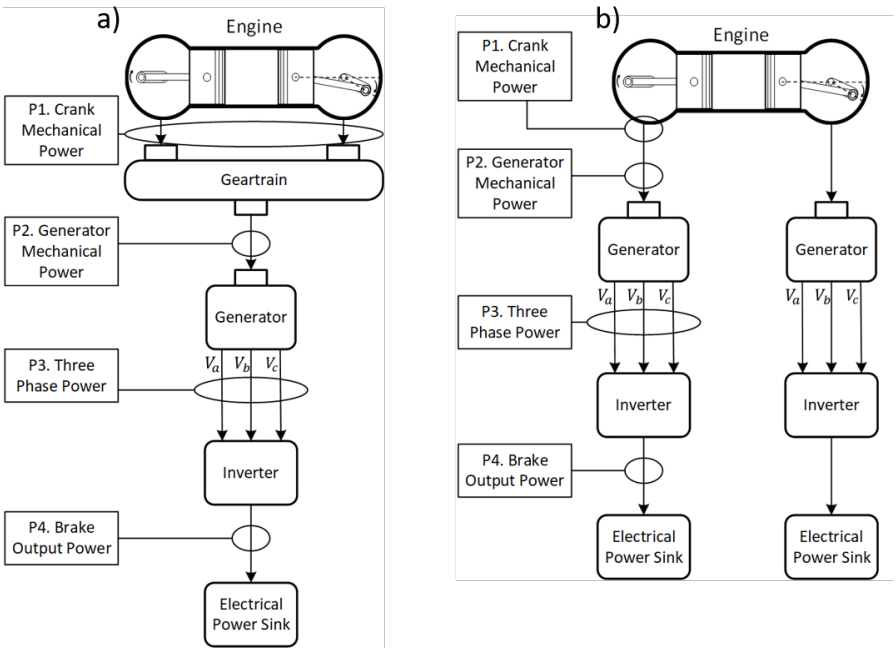

Figure 3.6: Hybrid opposed piston engine a) utilizing a geartrain and b) directly coupling the engine to motor/generators.

3.3 Feasibility of a Dual Motor Hybrid OP Engine

The purpose of this section is to investigate two hybrid designs utilizing electric machines attached directly to the power takeoff (PTO) of the OP engine. The electric machines can operate as both a generator, extracting the work from the crankshaft, and as a motor to input work to the crankshaft to regulate the engine speed. The first design, shown in Fig. 3.6(a) utilizes a conventional geartrain to link the crankshafts of the engine. The second design in Fig. 3.6(b) eliminates the geartrain, directly coupling an electric machine to each crankshaft. Before evaluating drive cycle efficiencies for this type of system, it is important to understand the interaction between the OP engine and the electric machines in the novel hybrid powertrain. While the OP engine itself may provide a high efficiency power generation platform [14], the means by which the work is absorbed from the crankshafts will highly influence the overall efficiency of the system, as detailed previously. Therefore, the focus in this analysis is the extraction efficiency of each concept.

In the following sections, the potential benefits and tradeoffs of each design are discussed and experimental results for a steady state operating condition of the engine are presented for both designs. A model of the electric components of the hybrid powertrain is then introduced to evaluate the power losses associated with each component of the electrical system. By combining the results of the engine testing, including torque and

speed measurements, with the electrical loss model, insights into the dynamic coupling between the OP engine and electric machines are developed. As expected, removing the geartrain of the OP engine significantly reduces the friction losses of the driveline and the maximum possible system efficiency is increased. A breakdown of frictional losses in a three-cylinder OP engine is provided by Salvi et al. [14], and shows the geartrain represents approximately 8% of the frictional losses. This percentage is substantially higher in a single cylinder engine as the friction due to the piston assembly, which is the main contributor of friction losses, is reduced proportionally to the number of cylinders, increasing the percentage of losses contributed by the geartrain. However, without the inertia of the geartrain, the electric machines must absorb the undamped torque pulsations of a single cylinder engine. The rapid change in torque demand from the electric machines to maintain stability of the OP engine can have a significant impact on the operating efficiency if not mitigated, and can negate any potential benefits of friction reduction.

3.3.1 Hybrid Opposed Piston Engine Systems

To analyze the trade-off in robustness and friction losses produced by the geartrain, two hybrid designs are considered. As shown in Fig. 3.6 (a), the first design, denoted here as the geared design, implements a geartrain to couple the crankshafts of the OP engine, and a single electric machine is coupled to the PTO of the geartrain. In this study, the geartrain is made up of five gears, one attached to each crankshaft, one gear used as the PTO, and an idler gear between each crankshaft gear and the PTO. The torque balance of the system between points P1 and P2 in Fig. 3.6 (a) can be described as

$$T_{\text{exh}} + T_{\text{int}} - T_{\text{g}} - T_{\text{fric}} = J\alpha \tag{3.10}$$

assuming the gear ratio of the geartrain is 1:1, T_{exh} and T_{int} represent the torque of the exhaust and intake crankshaft, T_{g} is the torque applied by the electric machine, and T_{fric} is the torque generated by the friction in the geartrain. Due to the relatively large magnitude of the inertia, J, for this design, small accelerations in the crankshaft are amplified. The fluctuations in electric machine torque required to regulate the changes in average engine speed is therefore reduced as the large inertia of the system resists changes in speed. The electric machine efficiency, which for steady-state operation can be mapped by speed and load, is also adversely affected by transience in the electric machine operation, meaning the increase in inertia improves work extraction efficiency. The efficiency loss due to transient operation will be quantified in the results section. Further, the ECL is fixed regardless of the torque balance in Eqn. 3.10, adding stability to the OP engine's operation as the electric

machine does not have to precisely regulate the relative crankshaft position.

In the second design considered, shown in Fig. 3.6(b) and denoted as the gearless design, the geartrain is removed and an electric machine is coupled directly to each crankshaft. This design exhibits a higher supremum of system efficiency due to the reduced frictional losses, but the electric machines are now required to control the instantaneous crankshaft dynamics. With the relative motion between the two crankshafts no longer fixed, the electric machines must now control the crankshaft motion to ensure the ECL is maintained. For each crankshaft, the torque balance is

$$T_{\mathrm{c}} - T_{\mathrm{g}} = J\alpha \tag{3.11}$$

where T_{c} is the engine torque on one crankshaft and α is the corresponding crankshaft acceleration. However, because this torque balance is applied independently on both crankshafts, the electric machine torque must regulate the system to follow a specific acceleration profile so the intake and exhaust pistons remain synchronized and can still facilitate combustion. Furthermore, a disturbance in the torque to one crankshaft impacts the other through cylinder pressure, which in turn depends on the individual crank positions and the state of combustion. In the geared design, the electric machine only has to maintain an average constant speed. It should be noted here that the decoupling of the crankshafts can pose other benefits specific to the engine operation, such as varying the ECL setpoint to adjust the engine operating regime between maximum power output or maximum indicated efficiency. However, this section focuses on the impact of the geartrain on work extraction efficiency over a single cycle of the engine and assumes the indicated thermodynamic efficiency of the engine as well as the frictional losses due to the piston and crankshafts remains constant in both designs.

The points of interest when comparing the work extraction efficiency of each design are given in Fig. 3.6. These represent the points of instantaneous power either measured or simulated and are defined as follows:

P1. Mechanical power delivered at each crankshaft of the OP engine (measured)

P2. Mechanical power delivered to the shaft of the electric machine (measured)

P3. Electrical three-phase power developed by the electric machine and delivered to the inverter (simulated)

P4. Electrical DC power output from the inverter and considered the final output power (simulated)

The geartrain efficiency, η_{gt}, is defined as P_2/P_1 and is only relevant to the geared design as P_2 and P_1 are equivalent in the gearless design. Similarly, the electric machine efficiency, η_g, is defined as P_3/P_2 and the inverter efficiency, η_i, is defined as P_4/P_3.

3.3.2 Baseline Engine Testing

To provide the experimental baseline results for each hybrid configuration, testing was completed using the same Achates Power single cylinder OP engine detailed in previous sections utilizing gasoline compression ignition (GCI). The objective of the engine testing was to supplement experimental torque and speed measurements for modeling of the electrical components of the system. Additionally, with the geartrain implemented on the OP engine, it is difficult to measure the torque of the individual crankshafts. Without a measured torque at the crankshafts, the friction losses due to the geartrain cannot be distinguished from the other friction losses of the engine. Therefore, steady state operating points were replicated between the geared and gearless designs to determine the friction losses attributed to the geartrain. The geared design testing was completed first and the fueling was adjusted to provide a 35 kW power output measured at P2. The same points were then run with the gearless design using the same fueling rate. The indicated thermal efficiency between the two tests showed good agreement with a difference of less than 1.5% for each point tested. These points included three speeds of 1600, 1800, and 2000 RPM. The injection timing was swept to include five different test points at each speed setting including -10, -11, -12, -13, -14 degrees after minimum volume (aMV). All tests were completed using an ECL of 0 degrees, as this is the setpoint typically used in low load, high fuel efficiency applications.

For the geared design testing, a dynamometer was used in place of the electric machine to regulate the speed of the engine. The position and speed of each crankshaft was measured along with the torque at the location of P2, between the geartrain and dynamometer. It should be noted that the velocity of the dynamometer is assumed constant due to the large inertia of the geartrain as well as the inertia of the dynamometer. With this assumption, the torque measured with the torque flange can be used as the torque from the electric machine in the geared design without having to account for changes in acceleration.

In the gearless design testing, each engine crankshaft was coupled to an Avid AF240 electric machine and the same instrumentation as in the geared experimentation is utilized for position and speed determination. A torque transducer was mounted inline with the motor and crankshaft coupler to measure the instantaneous torque on the shaft and calculate the power at P1. To determine the torque delivered by or to the electric machine, the

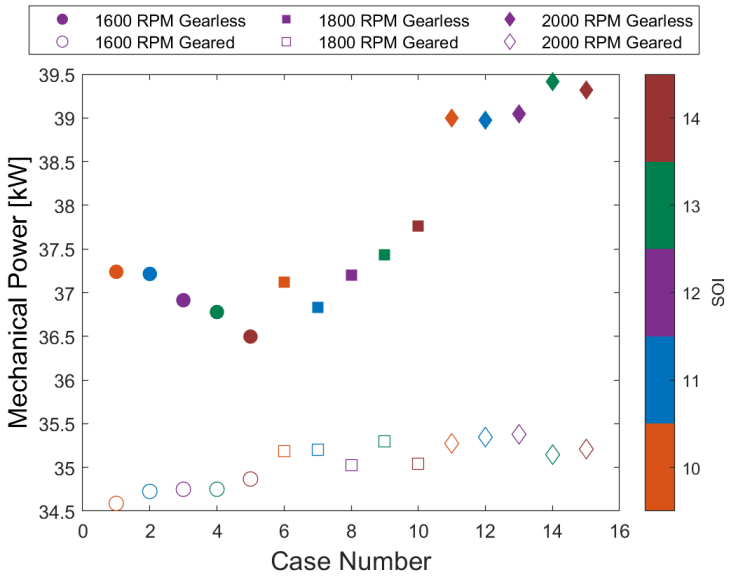

Figure 3.7: Cycle average mechanical power measured at point P2 for both configurations. Filled points represent the gearless design and unfilled points represent the geared design.

quadrature current of the motor rather than the torque measured on the engine crankshaft is used. The quadrature current of the electric machine is essentially proportional to the electric machine torque. Using the measured torque on the crankshaft would require the acceleration of the crankshaft to be computed, as noted in Eqn. 3.11 due to the velocity fluctuations present in this design, to relate the shaft torque to the electric machine torque. This can be noisy due to differentiation of the velocity signal.

As noted earlier, the electric machines in the gearless design are required to regulate the motion of the OP engine crankshafts. The velocity reference for both the intake and exhaust crankshafts are the result of the optimization process detailed in Chapter 2. Due to model uncertainty and the ill conditioned nature of the system, the electric machine torque still experiences large changes in instantaneous values, though significantly less than if trying to track a constant velocity reference. The significance of these torque fluctuations will be illustrated in the following sections.

The resulting cycle-averaged power for both series hybrid configurations is shown in Fig. 3.7. While the friction losses of the geartrain are similar for the 1600 and 1800 RPM test cases, averaging around 2.1 kW, it clearly scales with speed when engine velocity is increased to 2000 RPM, where the average losses are 3 kW. It should be noted, however, that the geartrain in use here is a prototype, meaning the gears are oversized and not optimized for efficiency.

While the gearless design clearly benefits from reduced frictional losses, the torque

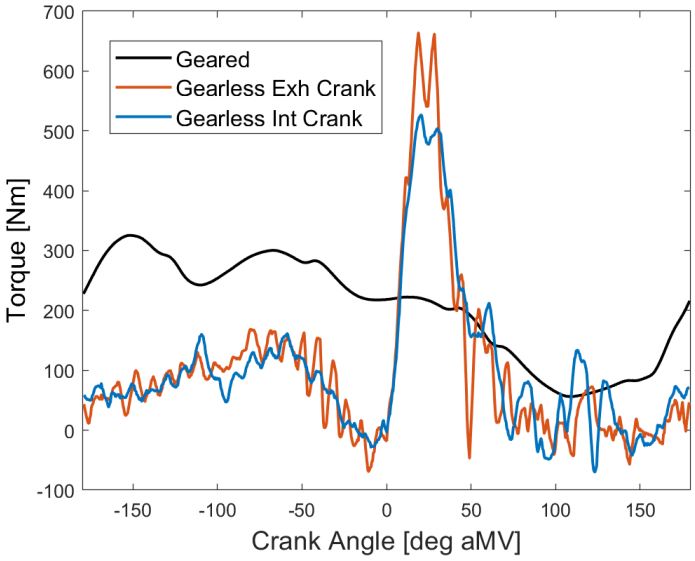

Figure 3.8: Electric machine torque used to regulate the motion of the power takeoff from the engine.

waveform which the electric machine is required to absorb from the PTO in each configuration is significantly different. Shown in Fig. 3.8, the torque profile for the geared design is relatively smooth, fluctuating ±125 Nm around the average 200 Nm value. In the gearless design however, the torque experiences a large spike just after minimum volume due to combustion. While only half the power is being delivered from each crankshaft in the gearless design as compared to the single PTO in the geared design, the peak torque from the electric machine is doubled. The following section will discuss the electrical loss simulation used to assess the performance of the electric machine and inverter for these different torque profiles. Using this tool, we then further investigate the impact of electric machine and engine parameters on work extraction efficiency using the setpoint of 1600 RPM and an SOI of -10 deg after minimum volume (aMV) as the representative operating point. This was chosen due to the frictional losses of approximately 2.5 kW, which represents a median value of the losses observed in testing.

3.3.3 Modeling of Work Extraction

To evaluate the power loss of each electrical component in the proposed series hybrid designs, a simulation of dynamic models for the electric machine, three phase inverter, and torque regulator were implemented in Simulink. In the geared design, the full power generated by the engine is passed through a single electric machine and inverter. In the

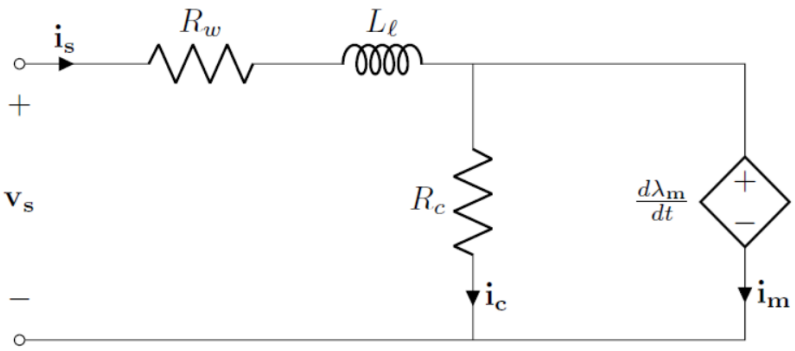

Figure 3.9: Two-phase equivalent model of a three-phase permanent magnet machine including winding and core losses.

gearless design, however, the power level is halved as each crankshaft is coupled to an electric machine, as depicted in Fig. 3.6(b).

3.3.3.1 Electric Machine

The permanent magnet motor/generator (Avid AF240) model is shown in Fig. 3.9, where the electrical variables are the two-phase equivalents of the three-phase machine in vector form. The vector λ_m represents the flux-linkage of the machine windings due to the permanent magnets and iron in the machine. This flux linkage is a nonlinear function of the magnetizing current i_m and rotor position θ_r and was determined through an off-line characterization experiment and implemented in the simulation via a lookup table. The inductance L_l represents leakage inductance associated with the machine and cables connecting the machine to the electric drive. The resistances R_w and R_c capture the losses in the machine windings and iron core, respectively, and were extracted from the efficiency map provided in the machine's datasheet using a least-squares parameter fitting. The instantaneous machine winding and core losses are therefore estimated as

$$P_{\mathrm{loss-winding}} = \frac{3}{2} R_\mathrm{w} ||i_\mathrm{s}||^2 \tag{3.12}$$

$$P_{\mathrm{loss-core}} = \frac{3}{2} R_\mathrm{c} ||i_\mathrm{c}||^2 \tag{3.13}$$

3.3.3.2 Three-Phase Inverter

The Simulink model of the three-phase inverter used in this work was originally presented by Song and Hofmann [47]. This model accurately captures the voltages and currents of the insulated-gate bipolar transistors (IGBT) of the inverter in their "on" and "off" states.

The instantaneous conduction power loss of the IGBTs is given by

$$P_{\text{loss}-\text{conduction}} = \sum_{x=a,b,c} (v_{x+} i_{x+} + v_{x-} i_{x-}) \tag{3.14}$$

where v_x and i_x denote the individual phase voltage and current while the + and - subscripts denote the high and low side of the half bridge switching unit, respectively. Energy loss is also generated during the switching transitions of the transistors. However, accurately capturing the voltage and current waveforms of the transistors during a switching transition would require a more complex transistor model as well as relatively small time steps in the simulation, both of which would dramatically increase the simulation time. To avoid this, the switching energy loss of the two transistors in a phase leg is calculated based upon the phase current and voltage at the time of the switching transition

$$E_{\text{loss}-\text{switching}} = f(i_x, v_b us) \tag{3.15}$$

where i_x is the phase leg output current. This energy is then extracted from the simulation. The IGBT v-i curves in the "on" and "off" states and switching loss function are generated using lookup tables with the datapoints extracted from the datasheet of the IGBTs (Semikron SKiiP 1814 GB17E4-3DUW V2). A junction temperature of 150°C was assumed due to the availability of data.

3.3.3.3 Torque Regulator

A field-oriented controller is used in the simulation to determine the switching transitions of the inverter IGBTs in such a way as to cause the output torque of the permanent magnet machine to track a torque reference. The performance of the electrical system in the proposed application was then determined by using the experimental torque profile (such as those in Fig. 3.8) as the torque reference of the regulator and integrating the corresponding crankshaft velocity to determine the rotor position θ_r of the permanent magnet machine. Average power and power losses in the electrical system are then calculated as

$$P = \int_0^{\tau} p(t) dt \tag{3.16}$$

where τ is the period of the crankshaft rotation and $p(t)$ represents the power losses previously described.

An outline of the electrical simulation is provided Fig. 3.10, combining each of the subsystems discussed in the previous sections. From the provided torque and rotational

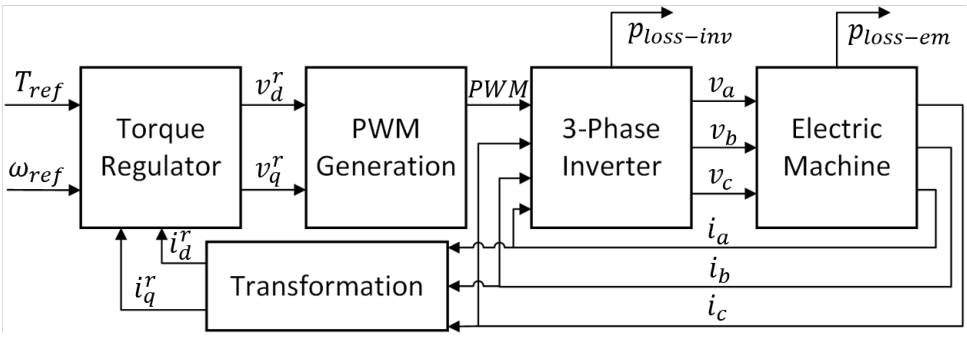

Figure 3.10: Schematic of electrical simulation using a torque and speed reference as inputs.

velocity profile, the torque regulator calculates the direct and quadrature voltage in the rotor reference frame using current feedback to decouple the equivalent two-phase motor dynamics. Using an inverse park transformation and space vector modulation, a pulse width modulation (PWM) reference is developed from the voltage signals to drive the inverter model. The resulting three-phase voltages are used to drive the electric machine model and the losses from both the inverter and electric machine are extracted from the respective subsystems.

3.3.4 Results

The operating point of 1600 RPM and an SOI of -10 aMV, labeled as case 1 in Fig. 3.7, along with a frictional loss of 2.5 kW for the geartrain is used for the detailed design comparison. To eliminate any impacts of indicated efficiencies of the OP engine and to provide a straightforward comparison of the work extraction efficiency, the brake power at point P1 for a single crankshaft in each design is considered to be 18.6 kW. Note however that P1 for the geared design encompasses both crankshafts, so P1 is 37.2 kW. This value comes from the cycle average power measured experimentally at the crankshafts for the gearless design. The electrical component efficiencies are obtained by applying the electrical loss simulation to the experimental torque and speed waveforms of each design.

Table 3.2 provides a summary of the results for the baseline designs. Initially, the overall efficiencies are similar. However, the motor efficiency for the geared system is much higher due to the smaller torque fluctuations. In fact, the magnitude of core losses in the electric machine are larger for the gearless design, despite this configuration transferring only half of the total power through the individual motors. As mentioned previously, the geartrain implemented on this engine is also of research grade, suggesting the 93.3% geartrain efficiency can be improved upon. If we consider the peak efficiency of the

Table 3.2: Electrical loss simulation results at baseline operating conditions for both hybrid OP engine designs

	Geared Design	Gearless Design
P1 [kW]	37.2	18.6
P2 [kW]	34.7	18.6
P3 [kW]	31.7	16.0
P4 [kW]	30.1	15.1
Total Electrical Losses [kW]	4.6	3.5
Electric Machine Losses [kW]	3.0	2.6
Winding; Core Losses [kW]	1.7;1.3	0.4;2.2
Inverter Losses [kW]	1.6	0.9
Geartrain η_{gt} [%]	93.3	n.a.
Electric Machine η_g [%]	91.3	86.0
Inverter η_i [%]	94.8	94.7
Overall η [%]	80.8	81.4

geartrain to be 98%, approximately the maximum efficiency of a spur or helical gear, the overall efficiency of the geared design can be improved to 85%, well above the gearless design efficiency of 81.4% for the baseline motor and engine parameters. From this point forward, the geartrain efficiency of 98% will be used to illustrate the ceiling for efficiency potential in the geared design.

3.3.4.1 Motor Sizing

The electric machines initially selected for this work, the Avid AF240s, were oversized to allow for a large domain of crankshaft motion profiles to be investigated. However, this selection is not ideal for maximizing the system efficiency. Therefore, a downsized motor/generator is considered in this section. Due to the nature of the AF240, which operates essentially as two smaller AF140 electric machines coupled in parallel, simulating a downsized motor can be achieved simply by doubling the magnitude of the torque demand from experimentation. This also allows the experimentally determined parameters in the electrical loss simulation to remain constant rather than reverting to manufacturer specified electric machine parameters. Results for the simulation using a downsized motor with half of the capacity previously utilized are given in Tab. 3.3. Note, the downsized motor inertia is considered identical to the full-sized motor. This allows the simulation to use the same experimental velocity profiles. The gearless case experiences the largest improvement in electric machine efficiency of approximately 3%. This is expected as the electric machines

Table 3.3: Electrical loss simulation results for both hybrid OP engine designs with downsized electric machines and improved geartrain efficiency for the geared design.

	Geared Design	Gearless Design
P1 [kW]	37.2	18.6
P2 [kW]	34.7	18.6
P3 [kW]	31.7	16.5
P4 [kW]	30.0	15.6
Total Electrical Losses [kW]	4.7	3.0
Electric Machine Losses [kW]	3.0	2.1
Winding; Core Losses [kW]	1.7;1.3	0.8;1.3
Inverter Losses [kW]	1.6	0.9
Geartrain η_{gt} [%]	98.0	n.a.
Electric Machine η_g [%]	91.4	88.8
Inverter η_i [%]	94.6	94.3
Overall η [%]	84.7	83.7

in the gearless design experience only half of the power levels than that of the single machine in the geared design and can therefore benefit more from downsizing.

While the overall efficiency of the gearless design improved, it is still less efficient than the geared design when considering the improved geartrain. Again, the core losses are proportionally much larger for the gearless design than for the geared design. The core losses in the electric machine occur due to time varying magnetic fields which are applied to the stator to produce the torque demanded from the machine. The large fluctuation in electric machine torque in the gearless design then leads to an increase in time varying magnetic field, and thus, the core losses of the machine. The significance of the magnitude of torque fluctuation on electric machine efficiency is captured by the ratio of peak to mean torque. For the geared design, the ratio is 1.67, and in this case the winding losses are greater in magnitude than the core losses. The ratio for the gearless design is nearly 4 times that at 6.56 and the core losses are then the dominant loss term for the electric machine. The following section provides a discussion for methods of reducing these core losses to improve the gearless design efficiency.

3.3.4.2 Engine Inertia

From the previous results, it is apparent the motor efficiency can be greatly improved by smoothing the electric machine torque required to control the piston motion. The most straight forward approach to achieve this would be to allow the engine crankshaft speed

to fluctuate such that the acceleration in Eqn. 3.11 accounts for change in torque from the engine, allowing the electric machine torque to maintain a constant value of the average engine out torque. However, due to the constraints of maintaining the ECL, this type of control remains infeasible. The system requires a predefined tracking reference over the entire cycle with which the feedback control strategy discussed previously can regulate the electric machine torque. The next possible means of smoothing the torque is to define a tracking reference for the crankshaft motion a priori. This is complicated by the sensitivity of the system to model uncertainty, as discussed in previous sections. Therefore, to fully develop the efficiency potential for the gearless series hybrid design, the hybrid OP engine model used Chapter 2 was implemented to explore the benefits of increased flywheel inertia and torque smoothing on the electric machine efficiency for the same 1600 RPM and 0 degree ECL setpoint as studied experimentally here. By increasing the inertia of the flywheel from 0.24 kg/m^2 to 0.49 kg/m^2 for the exhaust crankshaft and from 0.20kg/m^2 to 0.45 kg/m^2 for the intake crankshaft, the crankshaft motion becomes less sensitive to nonperiodic disturbances to the engine torque. Note the motor and crankshaft inertias are identical to the previous cases. The gains for the tracking controller can therefore be reduced, dampening the changes in electric machine torque demanded. Further, it should be noted that by using the model to complete this testing, the factor of model uncertainty is eliminated for the design of the crankshaft motion. The efforts described in the engine testing section for creating a crankshaft motion profile to reduce the demands on the electric machine are therefore more impactful in smoothing the torque as well.

The resulting torque and speed profiles from the model using the same setpoint as the experimental tests are provided in Fig. 3.11. The electric machine torques vary slightly as the inertia of the original flywheels are different. When an ECL is introduced to the system, the exhaust crankshaft experiences a larger peak in torque as the exhaust piston is past its respective top dead center (TDC) at minimum volume while the intake piston is still approaching its TDC. Thus, in the OP engine used in this study was designed with a larger inertia on the exhaust flywheel.

By employing this methodology, the full potential of the gearless hybrid OP engine design can be evaluated against the geared design. The efficiency predictions obtained by applying the electrical simulation to this torque and speed profile are provide in Tab. 3.4 for the gearless design and compared to previous geared design results, again defining P1 based on the experimental power level for the gearless design. Note that these results also include the benefits of the downsized electric machines. Of all the design changes, the smoothing of the electric machine torque created the largest system efficiency improvement at 10%. As expected with the smoothed torque profile, the core losses of the electric machine are

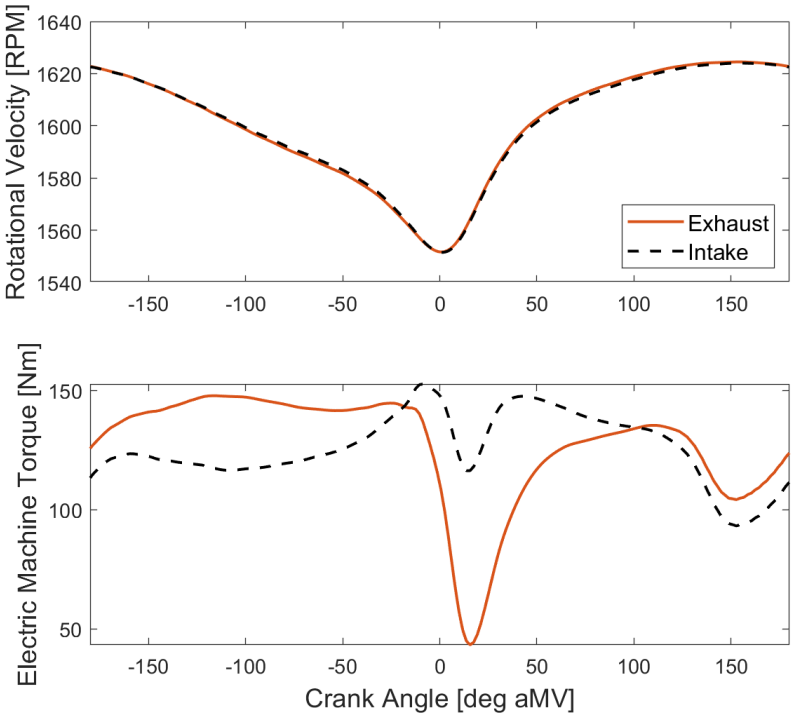

Figure 3.11: Crankshaft velocity and electric machine torque from the OP engine simulation with increased crankshaft inertia.

Table 3.4: Electrical loss simulation results for downsized electric machines and the gearless OP engine simulated with increased crankshaft inertia.

	Geared Design	Gearless Design
P1 [kW]	37.2	18.6
P2 [kW]	34.7	18.6
P3 [kW]	31.7	18.1
P4 [kW]	30.0	17.4
Total Electrical Losses [kW]	4.7	1.2
Electric Machine Losses [kW]	3.0	0.5
Winding; Core Losses [kW]	1.7;1.3	0.2;0.3
Inverter Losses [kW]	1.6	0.7
Geartrain η_{gt} [%]	98.0	n.a.
Electric Machine η_g [%]	91.4	97.1
Inverter η_i [%]	94.6	96.3
Overall η [%]	84.7	93.5

reduced by nearly one kilowatt. Similarly, the winding losses are also reduced. As the winding losses are created by the resistance in the motor and are proportional to the squared magnitude of current, a more constant torque demand on the electric machine correlates to a more constant current, and therefore a reduction in the winding losses. Another improvement in the gearless design efficiency is the inverter efficiency. Previous results have all maintained inverter efficiencies near 94%. However, while these losses are heavily dependent on the phase current, the transistor voltage drop also slightly increases with current. This can be attributed to the v-i relation of the conduction power loss. As the magnitude of the phase currents increase, so does the voltage. Therefore, as shown in Eqn. 3.14, the losses are not simply proportional to the current but also a function of phase voltage and will be minimized if the magnitude of the current and voltage is constant.

3.4 Conclusions

In this Chapter, particular focus was given to the feasibility of the dual motor controlled hybrid opposed piston architecture. A proof of concept experimental test cell was first constructed and a feedback controller with feedforward estimation of the motor torque was shown to adequately control the independent motion of the two crankshafts. However, the sensitivity of the system to model mismatch diminished the ability of the optimal crankshaft motion profiles developed in Chapter 2 to translate well to the experimental engine. Therefore, to evaluate the work extraction efficiency of the system, two designs for a series hybrid architecture utilizing an opposed piston engine were compared. By utilizing a detailed electrical loss simulation, the efficiency of the components responsible for extracting work from the engine were evaluated in each design. The design implementing a geartrain to couple the motion of the OP engine crankshafts presents a more robust system with the large inertia of the geartrain dampening speed fluctuations and reducing the fluctuations in electric machine torque required to maintain a constant average engine speed. Further, the crankshaft adds stability to the OP engine operation by fixing the ECL for the two crankshafts, regardless of the torque generated on each crankshaft. However, the peak system efficiency is limited by the frictional losses in the geartrain. By eliminating the geartrain and coupling electric machines directly to the OP engine crankshafts, the maximum work extraction efficiency can be significantly improved. This improvement, however, is highly dependent on the electric machine operation and any work extraction efficiency gains can be diminished by poor electric machine performance, as highlighted in Tab. 3.5. In the baseline case, the large electric machines and rapidly fluctuating torque used to control the motion of the engine crankshafts resulted in an overall efficiency lower

Table 3.5: Electric machine and inverter efficiency of the gearless hybrid OP engine for the alternative design parameters.

	Baseline	Motor Sizing	Motor Sizing and Increase Inertia
Electric Machine η_g [%]	86.0	88.8	97.1
Inverter η_i [%]	94.7	94.3	96.3
Overall η [%]	81.4	83.7	93.5

than that of the geared design. When sizing the electric machine appropriately for the power level of the engine and, more significantly, implementing some methodology to smooth the electric machine torque, the full potential of the gearless design for a series hybrid OP engine is realized.

As the peak electric machine efficiency was obtained for a near constant torque profile, the following Chapter details the methodology used to define optimal crankshaft motion profiles to smooth the motor torque as opposed to increasing the inertia and therefore the mass of the system.

CHAPTER 4

Maximizing Work Extraction Efficiency of a Hybrid Opposed Piston Engine Through Iterative Trajectory Optimization

This Chapter presents the real-time optimization of the crankshaft motion in a hybridized opposed piston (OP) engine using an iterative learning-based trajectory optimization scheme. The powertrain is oriented in a series hybrid design with each crankshaft directly coupled to electric motors, eliminating the conventional geartrain linking the two crankshafts along with the associated friction and weight. In this way, the electric motors can directly extract the work generated by the engine and regulate the crankshaft dynamics, introducing the capability to dynamically vary compression ratio, combustion volume, and scavenging dynamics on an inter-cycle basis. This control freedom increases the system's maximum potential efficiency, yet requires highly optimized intra-cycle crankshaft motion profiles to realize the improved work extraction efficiency of the dual motor-controlled OP engine. Leveraging the repetitive nature of the internal combustion engine, an iterative trajectory optimization (ITO) algorithm is used to define the optimal crankshaft motion profile in real-time for steady state operation. First, an algorithm to optimize the parameterized trajectory of a system in real time utilizing constrained optimization of a cost function generated from the performance values of the previous cycle is developed. Then, simulation results are used to illustrate the implementation of this iterative trajectory optimization framework on a toy problem while also benchmarking the performance against a norm optimal iterative learning controller with perfect system knowledge. Finally, this algorithm is applied to the problem of developing motion trajectories of the crankshafts in a hybrid OP engine. The rapid convergence and near optimal crankshaft motion profiles for the ITO strategy as well as its proficiency under both motored and fired cycle operation is demonstrated experimentally. Note, the theory presented in the first portion Chapter was published as [35].

4.1 Introduction

There are several applications performing repetitive processes such as airborne wind energy systems [48], robotic manipulators [49, 50], series hybrid powertrains [27], and UAV surveillance missions [51] where the shape of the trajectory used as a tracking reference has a dramatic impact on system performance. Typically, these applications use *offline* optimization to find the desired trajectory. However, these trajectories may not perform well on the actual system due to model mismatch and uncertainty. Further, this offline strategy does not take advantage of the information from previous cycles. When considering a repetitive process, the information rich signals from previous cycles can help to mitigate the effects of model uncertainty as well as adapt to slowly varying environmental disturbances or sensor drift [52].

A well documented strategy to improve the performance of repetitive systems is iterative learning control (ILC) [53, 54]. ILC has been effectively used in several applications where the optimal tracking reference in each application is know a-priori [55–57]. This work, however, focuses on applications where the system performs a repetitive task, but the performance of the system is not wholly dependent on the reduction in tracking error as it is in traditional ILC schemes. Rather, we focus on an economic performance index resembling that of offline trajectory optimization.

Recently, norm optimal ILC has enabled other control objectives to be incorporated into the ILC framework and leverage the flexibility in point-to-point applications [58–60]. In such cases, opportunity exists in the time between the mission-critical points to incorporate secondary task objectives, such as minimizing energy consumption in pick and place operations [50]. However, these algorithms are memory intensive and generally require a lifted representation of the system [61]. This again relies on the model fidelity. Several instances of ILC exist in literature which do not require the use of a lifted system, and therefore reduce the computational burden but still retain knowledge of the control or plant dynamics. In work published by Gorinevsky et al. [62], the ILC design problem is formulated in the frequency domain using a Fourier coordinate transform to represent the plant dynamics. In Tang et al. as well as Qin and Cai [63, 64], the inverse plant dynamics and desired tracking reference were parameterized using a Fourier series approximation, which was then used to update the ILC feedforward control law by matching the inverse plant dynamics to minimize tracking error. Further, Blanken et al. [56] used a norm-optimal ILC formulation to find the optimal parameters of non-causal rational orthonormal basis functions defining a feedforward control law to minimize tracking error. However, control signal parameterizaiton lacks the ability to prioritize tracking at certain waypoints as is

possible in the lifted system description and point-to-point ILC [58].

Therefore, rather than parameterizing the control input, it is suggested to parameterize the reference trajectory directly and use measured performance variables to optimize the next cycle reference *trajectory*, rather than the next cycle *control*. Previous work from Cobb et al. [52] demonstrated this iterative trajectory learning for the application of an airborne wind energy system. A parametric form of the desired trajectory reference was optimized using a gradient descent algorithm according to the prescribed cost function. While the figure eight trajectory parameterization proposed by Cobb et al. [52] is specific to their application, a more generic parameterization could be implemented. However, as the learning technique implements a gradient descent optimization strategy, trajectory constraints could not be included when using a more generic parameterization.

In the following sections, a novel method of iterative learning based online trajectory optimization is presented, referred to here as iterative trajectory optimization (ITO). To reduce the computational expense of a lifted system description, we utilize the Fourier series to provide a parameterization of the system trajectory where only the basis parameters are optimized rather than all the discrete points contained in the reference trajectory. A Fourier series was selected due to its inherent ability to approximate periodic functions, as is noted in previous ILC work [63, 64]. The optimization problem is then formulated as a quadratic programming (QP) problem which presents the opportunity to integrate constraints on the optimized trajectory, similar to the online trajectory generation presented by Mellinger and Kumar [65] which optimizes the parameterized path of a quadrotor while ensuring constraint satisfaction. However, by utilizing performance values from the previous cycle iteration, the influence of model uncertainty and slowly varying, non-periodic disturbances can be significantly reduced.

4.2 Problem Description

Here we will consider a system of discrete time dynamics defined by

$$\begin{aligned} x_j(k+1) &= f(x_j(k), u_j(k), k) \\ y_j(k) &= g(x_j(k), u_j(k), k) \end{aligned} \tag{4.1}$$

where j represents the iteration index and $k = 1, 2, ..., N$ is the cycle time index. The system states are given as $x \in \mathbb{R}^n$, the outputs of interest are $y \in \mathbb{R}^p$, and the inputs are $u \in \mathbb{R}^q$. The value of $u_j(k)$ represents the control input required for following the desired output trajectory $r_j(k) \in \mathbb{R}^p$, which, in the ideal case with no tracking error, is equivalent to $y_j(k)$.

To simplify notation, we will assume $p = 1$. Also, assume the system is stable or stabilized through feedback control with bounded input and output. The objective in this Chapter is to alter the time varying trajectory reference $\mathbf{r}_{j+1}$ of the next cycle, which is defined as the vector

$$\mathbf{r}_{j+1} = [r_{j+1}(1) \quad r_{j+1}(2) \quad \dots \quad r_{j+1}(N)]^T \tag{4.2}$$

so as to minimize a given cost function subject to the pertinent system constraints. We assume a stabilizing low level controller with good tracking performance already exists.

The cost function for trajectory optimization is

$$\begin{aligned} \min_{r(k)} \quad & L = \sum_{k=1}^{N} l(x(k), r(k), k) \\ \text{s.t.} \quad & m_i(x(k), r(k), k) \leq 0 \end{aligned} \tag{4.3}$$

where $i = 1, 2, \dots, w$ with w representing the number of constraints. The discrete-time trajectory optimization problem defined in Eqn. 4.3 can be solved by transcribing the problem as a finite dimensional mathematical programming problem. The variables being optimized and the state variables of the model, in this case $r(k)$ and $x(k)$, can be stacked in a vector, $\mathbf{X}$, and the system dynamics between the reference $r(k)$ and states $x(k)$ are enforced in the problem constraints. This method, however, is not well suited for real-time applications. Significant computational resources are required as the vector $\mathbf{X}$ can become large depending on the number of steps N. Further, convexity is not guaranteed in the cost function Eqn. 4.3 which makes it impossible to guarantee convergence. The results are also subject to model uncertainty as the relation between $\mathbf{x}$ and $\mathbf{r}$ is assumed to be explicitly known. Therefore in this section, an iterative learning algorithm is developed to exploit measurements of the previous cycle's performance to improve the reference trajectory for the next cycle. The formation of a cost function and path parameterization are presented so as to meet the following requirements:

(R1) A relatively small number of basis parameters are needed compared to discrete sampling points in an iteration.

(R2) The parameters of the basis function explicitly define the reference trajectory and its higher order derivatives.

(R3) The basis parameters can be found by solving a constrained, convex optimization problem.

4.3 ITO Structure

In this section, the proposed iterative trajectory optimization scheme is defined along with the properties that satisfy the requirements listed above.

4.3.1 Path Parameterization

The parameterization used to defined the reference trajectory variable $\mathbf{r}$ is key to the formulation of the ITO problem. While parameterization of the trajectory variable may result in a sub-optimal trajectory reference, as discussed by Cobb et al. [52], this allows for a reduction in the optimization terms and trajectory design space. A Fourier series is used to represent the approximate trajectory variable as

$$\hat{r}(k) = \gamma_0 + \sum_{n=1}^{m} \left(\gamma_{n,1}\cos(n*wk) + \gamma_{n,2}\sin(n*wk)\right) \tag{4.4}$$

which now becomes the tracking reference for the lower level tracking control. The $\hat{r}(k)$ notation is used to denote the sub-optimality associated with the parameterization of $r(k)$. For this approximation, $w = 2\pi f \Delta t$ where f is the frequency of the periodic function and Δt is the sampling period. The number of frequencies contained in the Fourier series parameterization is denoted as m. Factoring out the γ coefficients, the trajectory variable can be written as

$$\hat{r}(k) = h(k)^T \Gamma \tag{4.5}$$

where $h(k)$ and the basis parameters Γ are

$$\begin{aligned} h(k) = [1 \;\; \cos(wk) \;\; \sin(wk) \;\; \cos(2wk) \;\; \sin(2wk) \\ \ldots \;\; \cos(m*wk) \;\; \sin(m*wk)]^T \end{aligned} \tag{4.6}$$

$$\Gamma = [\gamma_0 \;\; \gamma_{1,1} \;\; \gamma_{1,2} \;\; \gamma_{2,1} \;\; \gamma_{2,2} \;\; \cdots \;\; \gamma_{m,1} \;\; \gamma_{m,2}]^T. \tag{4.7}$$

Remark 1. The trajectory reference using $\hat{r}(k)$ can be defined using only a $2m+1$ quantity of γ parameters rather than the N discrete points required to define the trajectory in Eqn. 4.2. Increasing the number of harmonic frequencies, m, improves the ability of $\hat{r}(k)$ to approximate the ideal trajectory but increases the number of basis parameters. Shown in the example provided, satisfactory results can be obtained with values of $m = 4, 6$ compared to $N = 100$, satisfying (R1). Additionally, it is important to note that the bandwidth of the stable closed loop system defined in Eqn. 4.1 limits the benefits of increasing the number of frequencies contained in the reference trajectory beyond the bandwidth frequency.

Remark 2. Using the notation of Eqn. 4.5, it is straight forward to differentiate the trajectory as

$$\hat{r}^{(d)}(k) = h^{(d)}(k)^T \Gamma \tag{4.8}$$

where d is the order of the derivative as $h(k)$ is continuously and infinitely differentiable while Γ remains constant, therefore satisfying (R2).

Remark 3. For practical applications, it may be beneficial to define $h^{(d)}(k)$, with d being the highest order derivative, as the trigonometric function vector given in Eqn. 4.6. Then, integration, rather than differentiation, can be used to find the lower order terms where $h^{(d-1)}(k)$ is now

$$\begin{aligned} h^{(d-1)}(k) = \Bigg[& k \;\; \frac{\sin(wk)}{w} \;\; \frac{-\cos(wk)}{w} \;\; \frac{\sin(2wk)}{2w} \\ & \frac{-\cos(2wk)}{2w} \cdots \;\; \frac{\sin(m*wk)}{m*w} \;\; \frac{-\cos(m*wk)}{m*w} \Bigg]^T . \end{aligned} \tag{4.9}$$

Now, the non-periodic time dependent term k in the lower order trajectory variable term relaxes the necessity of the trajectory to be periodic for such instances where the repetitive process is non-continuous.

4.3.2 ITO Update Scheme

The iterative trajectory optimization scheme proposed in this Chapter is formulated as a QP problem and can be solved as a linear system of equations when only equality constraints are considered [66]. Therefore, the optimization problem is posed as

$$\begin{aligned} \min_{\Gamma} \quad & J = \frac{1}{2}\Gamma_j^T \Omega_j \Gamma_j + \Psi_j \Gamma_j + c_j \\ s.t. \quad & A\Gamma_j - b = 0. \end{aligned} \tag{4.10}$$

The trajectory update law utilizes the resulting parameters Γ_j to update the next cycle reference and is given as

$$\hat{r}_{j+1}(k) = h(k)^T(\Gamma_j). \tag{4.11}$$

with the definitions of $h(k)$ and Γ from Eqn. 4.6 and 4.7. The weighting matrices Ω_j and Ψ_j are defined as

$$\begin{aligned} \Omega_j = 2\sum_{k=1}^{N} & \beta_{q0,j}(k)h(k)h(k)^T + \beta_{q1,j}(k)\dot{h}(k)\dot{h}(k)^T + \\ & \ldots + \beta_{qd,j}(k)h^{(d)}(k)h^{(d)}(k)^T \end{aligned} \tag{4.12}$$

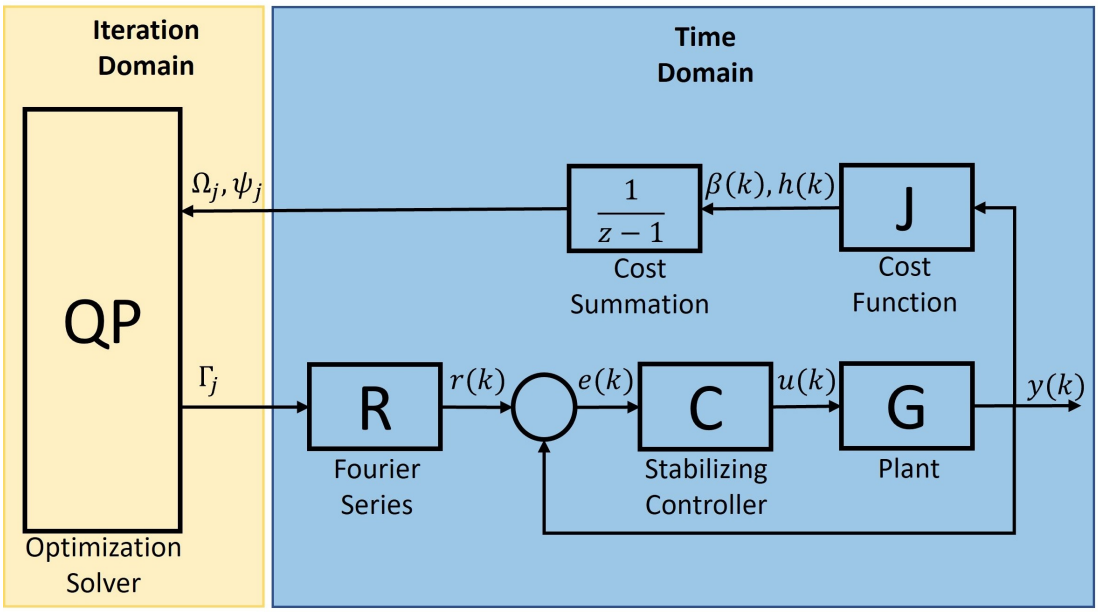

Figure 4.1: Block diagram showing interaction between the optimization process in the iteration domain and the lower level control system in the time domain.

$$\Psi_j = \sum_{k=1}^{N} \beta_{l0,j}(k) h(k)^T + \beta_{l1,j}(k) \dot{h}(k)^T + \\ \ldots + \beta_{ld,j}(k) h^{(d)}(k)^T \tag{4.13}$$

and the derivation of these matrices will be provided in the following section. The block diagram illustrating this ITO strategy is shown in Fig. 4.1, where the summation of the cost parameters at each time step in the cyclic process is then provided to the optimization solver as Ω_j and Ψ_j. The solution of the optimization problem then provides Γ_j to define the following cycle reference.

Remark 4. The optimization problem defined in Eqn. 4.10 provides strict convexity under certain, rather mild, assumptions, as will be discussed later for the convergence of Γ_j. With feasible A and b constraints, this satisfies (R3).

4.3.3 ITO Derivation

The formulation of a trajectory optimization problem defined in Eqn. 4.3 with the cost function L is not well suited for online implementation. Therefore, this section presents the transformation of the simplified cost function into the ITO scheme defined by Eqn. 4.10. The derivation considers only the base trajectory $\hat{r}(k)$ for simplification, but extension to higher order derivative terms is trivial, as shown in Eqn. 4.12 and 4.13.

First, the cost function is given in terms of the trajectory variable $r(k)$ and is shown as

$$J = \sum_{k=1}^{N} \beta_{q,j}(k) r_{j+1}(k)^2 + \beta_{l,j}(k) r_{j+1}(k) + \beta_{c,j}(k). \tag{4.14}$$

It should be noted that this form of the cost function is more limiting than that of the form given by L in Eqn. 4.3, but improves the solution properties. The new cost in Eqn. 4.14 is formulated as a QP problem that is linear with respect to the trajectory variable $r(k)$. The coefficients of $\beta_{c,j}(k)$, $\beta_{l,j}(k)$, and $\beta_{q,j}(k)$, collectively referred to as $\beta_j(k) = [\beta_{c,j}(k) \quad \beta_{l,j}(k) \quad \beta_{q,j}(k)]^T$, are applied as coefficients for a constant term, a linear trajectory variable term $r_{j+1}(k)$, and a quadratic trajectory variable term $r_{j+1}(k)^2$ respectively. The determination of these β terms is application specific. These values can represent constant parameters such as component mass or lengths, time varying terms such as torque, or a combination required to formulate the cost J. For the sake of the generic problem derivation, $\beta_j(k)$ will be considered time dependent.

Using the path parameterization defined by Eqn. 4.5, the cost can be written as

$$\begin{aligned} J = \sum_{k=1}^{N} \Gamma_j^T (\beta_{q,j}(k) h(k) h(k)^T) \Gamma_j + \\ \ldots \quad \beta_{l,j}(k) h(k)^T \Gamma_j + \beta_{c,j}(k). \end{aligned} \tag{4.15}$$

Here, $h(k)$ as well as the $\beta(k)$ terms are time dependent over a given cycle. However, Γ_j is time invariant over each cycle, which means it can be removed from within the summation. Now, using the notation

$$\Omega_j = 2 \sum_{k=1}^{N} \beta_{qj}(k) h(k) h(k)^T \tag{4.16}$$

$$\Psi_j = \sum_{k=1}^{N} \beta_{lj}(k) h(k)^T \tag{4.17}$$

the QP problem outlined in Eqn. 4.10 can be recovered. The derivation for any higher order derivative terms of the trajectory reference, $\hat{r}^{(d)}(k)$, follows from above and are included as in the forms of Ω_j and Ψ_j used in Eqn. 4.12 and 4.13.

4.4 ITO Convergence Analysis

This section provides a discussion of convergence for the ITO scheme given in Eqn. 4.10 and 4.11. Here, convergence of the path parameters Γ to the optimal parameters Γ^*, which minimize the cost function J, is of interest. This is similar to the convergence analysis

presented by Cobb et al. [52] where the *tracking reference*, not the control input, is being optimized. First, the definitions and assumptions required are stated, then Proposition 1 is used to show the positive definiteness of Ω and the strict convexity of J in Eqn. 4.10, leading to the convergence of Γ_j.

The following assumptions are made for this analysis:

Assumption 1. The values of β_{qi} used in the quadratic term Ω, where $i = 0, 1, ..., d$, are strictly positive and the number of sample points, N, in a cycle is larger than the number of parameters in the Γ vector, $2m+1$.

Assumption 2. The constraints defined in Eqn. 4.10 are feasible at Γ^* and the Linear Independence Constrain Qualification (LICQ) condition holds for A^T [66].

Assumption 3. The initial conditions, $x(0)$, and any disturbances to the system are iteration invariant and $\beta_j(k)$ for $k = 1, 2, ..., N$ converges to $\beta_\infty(k)$ as $\hat{r}_j(k) \to \hat{r}_\infty(k)$.

Assumption 1 is used to show the positive definiteness of Ω. Assumption 2 simplifies the solution of the QP problem as well as the convergence proof as the active set of constraints are known. Assumption 3, the most severe assumption made, ensures the values of β, which define the response surface J, converge to some fixed point $\beta_\infty(k)$. Under these assumptions, it is possible to guarantee convergence of Γ_j to Γ^*.

Proposition 1. (Convergence of Γ): Suppose Assumption 1, 2, and 3 hold. Then, under the Γ_j update from the QP problem defined in Eqn. 4.10 and the reference trajectory update in Eqn. 4.11, the sequence of Γ_j converges to Γ^*

Proof. Consider a single instant k in the summation denoted in Eqn. 4.12. Taking the outer product of the vector h, it can be shown that $\forall x \in \mathbb{R}^{2m+1}$

$$x^T h h^T x = (h^T x)^T (h^T x) = (h^T x)^2 \geq 0$$

meaning hh^T is symmetric positive semi-definite. Similarly, any derivatives of the vector h with respect to sample time are also symmetric positive semi-definite due to the nature of the outer product.

Now, consider the summation of these terms for $k = 1, 2, ..., N$. It is important to note that the vector $h(k)$ is composed of $\cos(wk)$ and $\sin(wk)$ terms. As these terms, for different values of k, are mutually orthogonal functions, the summation of the

$$\Omega_j = \sum_{k=1}^{N} h(k) h(k)^T$$

is rank $2m+1$, or full rank, for any $N > 2m+1$. As the value of β_{qi}, $\forall i = 0, 1, .., d$ is a scalar, and from assumption 2, strictly positive, this does not affect the linear independence

or positive semi-definiteness of any of the individual outer product values. Therefore, as the nullspace of Ω_j is now only the zero vector, $x^T\Omega_j x > 0\ \forall x \neq 0 \in \mathbb{R}^{2m+1}$ given $N > 2m+1$.

As the constraints are affine and linearly independent from Assumption 2 and the cost function J is strictly convex using the positive definiteness of Ω_j, the first order conditions for optimality are sufficient. Therefore, the Γ_j update from the QP problem defined in Eqn. 4.10 is immediately Γ_j^* for the parameters $\beta_j(k)$. From Assumption 3, we can assume $\beta_j(k)$ converge to $\beta_\infty(k)$. Thus, it follows Γ_j converge to Γ^*. □

4.4.1 Discussion of ITO Convergence

The first two assumptions rely on the formulation of the cost function and system constraints, which can be satisfied relatively easily. Assumption 3, however, will almost certainly be violated in practical applications, especially for continuous applications where the final conditions of the previous cycle become the initial conditions of the next cycle. Firstly, identical initial conditions are difficult to guarantee when the tracking of the reference is dependent upon a lower level, stabilizing controller. Further, external disturbances can vary from iteration to iteration, affecting the initial conditions and creating non-periodic disturbances. Lastly, and most importantly, it can not be assumed the unique β_∞ at Γ^* are the values which allow for the global minimization for the response surface J. Rather, it is a local approximation based on the initial guess of the optimal trajectory. If the $\beta_j(k)$ values in the cost function are time varying functions of the path $\hat{r}(k)$, changes in the path geometry can change the values of $\beta_j(k)$. Therefore, when designing a cost function for ITO applications, care must be given in the selection of the $\beta_j(k)$ terms to ensure they are at least bounded in their response to changes in Γ_j.

4.5 Example Problem

To demonstrate this ITO scheme, a comparison to norm-optimal ILC is provided as a benchmark for performance. A problem similar to the one posed by Lim and Barton [58] illustrates the proposed algorithm's capabilities as well as limitations. In this example, a servo-positioning system is considered with a discrete-time transfer function of

$$G(z) = \frac{z-0.5}{(z-1)(z-0.925)} \tag{4.18}$$

for the plant with a sample time of 1 second. This plant is stabilized using a proportional feedback controller with a gain of 0.425. The premise of this problem is a traditional

position tracking control problem where a reference trajectory for position is provided over a 100 second period. However, only 3 specific points at time 40, 65, and 100 seconds in the predefined trajectory are critical for tracking as shown in Fig. 4.2(a). Therefore, it is desired to leverage the additional control freedom during the rest of the cycle to minimize the energy consumption of the system for a cycle period. Here, the energy of the system is taken to be $E = \frac{1}{2}mv^2$ where m is the system mass and v is the velocity.

4.5.1 Benchmark Control Design

In reference Lim and Barton [58], a modified norm optimal ILC algorithm is proposed utilizing a Pareto optimization approach wherein both point-to-point tracking performance and energy consumption are included in the cost function. The resulting ILC update law and cost function are given as

$$\mathbf{u}_{j+1} = \mathbf{L}_u\mathbf{u}_j + \mathbf{L}_e\mathbf{e}_j + \mathbf{L}_v\mathbf{v}_j \tag{4.19}$$

$$\begin{aligned} J =& (\Psi\mathbf{e}_{j+1})^T Q(\Psi\mathbf{e}_{j+1}) + \mathbf{u}_{j+1}^T S\mathbf{u}_{j+1} \\ &+ (\mathbf{u}_{j+1} - \mathbf{u}_j)^T R(\mathbf{u}_{j+1} - \mathbf{u}_j) + \mathbf{v}_{j+1}^T W\mathbf{v}_{j+1} \end{aligned} \tag{4.20}$$

where $\mathbf{L}_u$, $\mathbf{L}_e$, $\mathbf{L}_v$ are the learning matrices applied to the control, error, and velocity vectors of each iteration to provide the next iteration's control input. The velocity, $\mathbf{v}_j$, is related to the control input $\mathbf{u}_j$ through $\mathbf{v}_j = \mathbf{X}\mathbf{H}\mathbf{u}_j$ where $\mathbf{X}$ is the first difference matrix and $\mathbf{H}$ is the lifted system representation. Refer to Lim and Barton [58] for a detailed derivation.

4.5.2 Iterative Trajectory Optimization Design

As this methodology alters the reference trajectory and the tracking control is completed with the lower level proportional control, the cost function no longer contains control input values and can simply be represented as

$$J = \sum_{k=1}^{N} v_j(k)^2 \tag{4.21}$$

where the $\frac{1}{2}m$ terms have be dropped as they remain constant and $v_j(k)$ represents the true system velocity. Therefore, it is of interest to use the reference and tracking error to approximate the true velocity. To include reference velocity in the trajectory parameterization, we define the reference velocity as $\hat{\dot{r}}_{j+1}(k) = \dot{h}_j(k)^T\Gamma_{j+1}$ where $\dot{h}_j(k)$ replaces $h_j(k)$ in Eqn. 4.6. Similarly, as the reference provided to the closed loop system

is in terms of position, the position reference is defined as $\hat{r}_{j+1}(k) = h_j(k)^T \Gamma_{j+1} + C_1$ with $h_j(k)$ defined in Eqn. 4.9 and C_1 is the constant of integration. In this case, as the initial position is assumed to be 0, this values becomes

$$C_1 = \frac{\gamma_{1,2}}{w} + \frac{\gamma_{2,2}}{w} + ... + \frac{\gamma_{m,2}}{w} \tag{4.22}$$

As the constant is a function of Γ, it can be combined into Eqn. 4.9. Then, by defining $v_j(k) \approx \dot{r}_{j+1}(k) - e^v_j(k)$ where e^v is the velocity error, we can define Ω and Ψ as

$$\Omega_j = 2 \sum_{k=1}^{N} \dot{h}(k) \dot{h}(k)^T \tag{4.23}$$

$$\Psi_j = 2 \sum_{k=1}^{N} e^v_j(k) \dot{h}(k)^T \tag{4.24}$$

which can be used in the QP problem in Eqn. 4.10 and defines $\beta_{q1,j} = 1$ and $\beta_{l1,j}(k) = e^v_j(k)$. All other β_j terms are 0. As the duration of the repetitive process is 100 seconds, w for this application is taken as $w = \frac{2\pi}{100}$. Additionally, to ensure the critical points of the tracking task are met, three equality constraints are introduced for $r_{j+1}(40, 65, 100) = p_c$. Note, by integrating to find position, the position profile is no longer constrained as periodic and the initial and final points of the position trajectory can differ to meet these constraints as discussed in remark 3. To account for any steady state tracking error that may be present for the closed loop system at these points, the iterative nature of the system can again be leveraged to adjust the constraints using the update

$$p_{c,j+1} = p_{c,j} + e_j(40, 65, 100) \tag{4.25}$$

where e_j is the position tracking error and $p_{c,1} = [7, -5, 10]$.

4.5.3 Results

The Pareto ILC and the ITO results are shown in Fig. 4.2(b). Two different ITO trajectory parameterizations containing 4 and 6 frequencies are shown after 15 cycle iterations. The optimized position trajectories which reduce energy consumption are all similar, but deviate significantly from the baseline feedback controller tracking the full reference trajectory shown in the top subplot. The Pareto optimization-based ILC has perfect knowledge of the system and therefore the lowest cost which results in a constant velocity trajectory between critical points, shown in Fig. 4.2(b). Further, it is able to converge in one cycle.

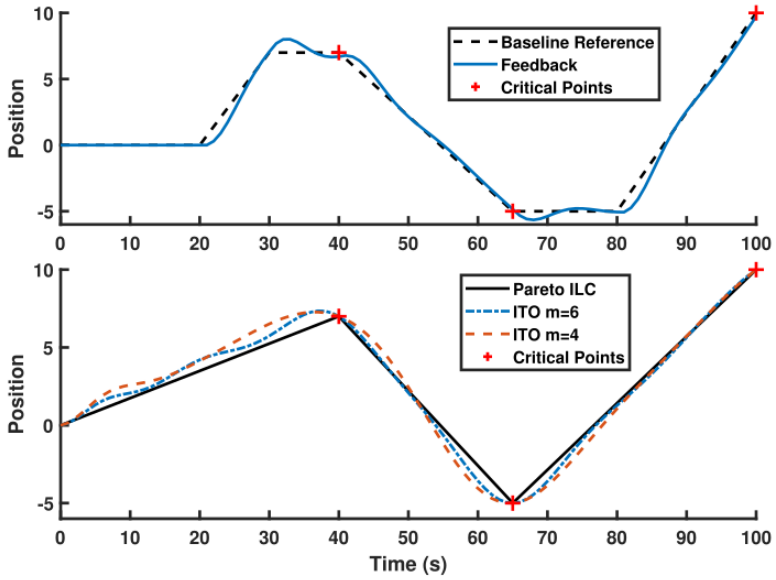

Figure 4.2: Baseline tracking reference for the system and the three critical position points at 40, 65, and 100 seconds. Simulation results for the ILC and ITO schemes with reference to the baseline feedback control. Critical points are denoted with an + and m represents the number of frequencies in the trajectory parameterization.

However, this performance degrades as model uncertainty is introduced resulting in a trade-off between robustness and performance [61]. The ITO scheme has no knowledge of the system, yet provides a close approximation of the ILC results after only 15 iterations.

The quantitative metrics of root mean square error (RMSE) at the critical points and the cost function value described in Eqn. 4.21 are used to compare the ITO to the ILC in to Tab. 4.1. Note, as the true model is assumed known, the learning gains of S and R for the ILC scheme are set to 1e-8 in Eqn. 4.19. This provides a direct comparison of the energy consumption of the system, assumed here to be $\sum_{k=1}^{N} v_j(k)^2$. For both the ITO and ILC, the RMSE at the critical points and cost function value are significantly reduced from the baseline feedback controller. As the number of harmonics included in the ITO is increased, the optimal parameterized trajectory converges to that of the ILC and the cost reduces. However, this trend is not monotonic due to bandwidth limitations for the closed loop system as well as the presence of tracking error in the cost function.

Clearly, increasing the frequency content of the reference above the system bandwidth of 0.885 rad/s, which in this case corresponds approximately to $m = 14$, will not provide any appreciable benefit to system. However, when using $m = 14$ in this application, the cost value after 15 iterations is 41.530 due to the inability to track the reference, and does not improve with increased iteration counts. The ITO method obtained the minimum cost

Table 4.1: RMSE and Cost Function Results

Method	RMSE	Cost
Feedback	0.250	12.688
ITO m=4	2.29e-4	7.716
ITO m=6	1.60e-3	7.334
Pareto ILC	6.92e-4	6.705

value of 7.323 with $m = 7$ after 15 iterations, which results in a highest harmonic frequency of 0.440 rad/s in the reference trajectory which is below the system bandwidth.

The proposed ITO framework was implemented for a servo positioning application and benchmarked against Pareto-optimization based ILC. Without any prior knowledge of the system, ITO was able reduce the cost by 42%, relative to the feedback controller, using $m = 7$ frequencies and only 15 iterations. The ITO method achieved approximately 90% of the ILC performance, which utilized perfect knowledge of the closed loop system. Now, in the following sections this online trajectory optimization scheme will be applied to the problem of finding the optimal crankshaft motion profile for the dual motor controlled OP engine powertain.

4.6 ITO for a Hybrid OP Engine

As discussed in Chapter 3, the dual-motor system efficiency is highly dependent on the operation and required control torque from the electric motors. Any gains in efficiency from removing the geartrain can be lost to poor motor performance. Results from Chapter 2 show a near constant motor torque profile maximizes the work extraction efficiency of this system. Yet, the necessity to maintain the relative positioning between the two pistons requires control over the instantaneous crankshaft position and prohibits the use of constant intra-cycle torque control to maintain the desired engine speed. The challenge then is not in controlling the crankshaft to a desired position trajectory. Rather, it is defining the optimal position and velocity trajectory to control to. However, the system has shown significant sensitivity to model uncertainty, limiting the effectiveness of offline optimization. Instead, the repetitive motion of the reciprocating IC engine can be leveraged to implement a learning-based scheme for ITO. In this way, the information rich signals from the previous engine cycle can be used to improve the tracking reference of the next cycle based on the performance criteria. Further, the use of the previous cycle data reduces the reliance of the optimization process on the fidelity of the system model while still maintaining the required

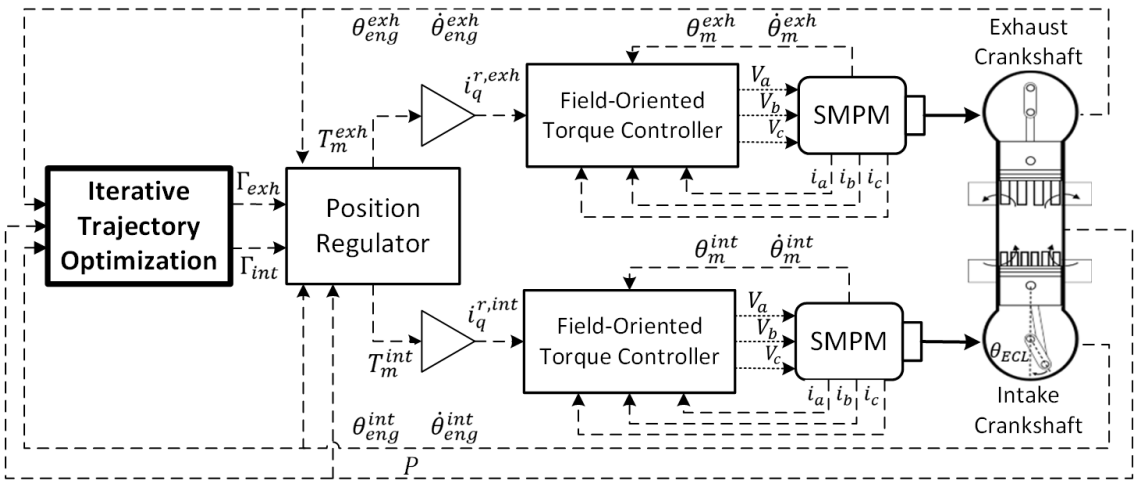

Figure 4.3: Control architecture of the hybridized OP engine. Solid lines represent mechanical connections, dotted lines represent electrical connections, and dashed lines represent control or measurement signals. The trajectory optimization algorithm provides the basis parameters Γ defining the tracking reference to the lower level controls.

constraint on the relative phasing of the two crankshafts. This method of defining the crankshaft motion on an experimental engine test-bench represents a complex combination of the operating principles outlined in Chapter 2, feedback control and feasibility analysis completed in Chapter 3, and the ITO theory defined earlier in this Chapter. The resulting control structure to be implemented is shown in Fig. 4.3.

The following sections derive the path parameterization and cost function coefficient necessary to implement the ITO scheme on a dual motor controlled hybrid OP engine. Note, however, the derivation of this ITO problem will be completed with respect to a single crankshaft as the problem objective and dynamics for each crankshaft are identical. Then, as the ECL must be constrained, the final form of the optimization problem will be given with respect to both the intake and exhaust crankshafts.

4.6.1 Crankshaft Path Parameterization

With the trajectory of the system, rather than the control input, used as the optimization variable, it is necessary to parameterize the the trajectory variable. This variable is defined as $\theta_d(k)$, the desired position of the crankshaft, and replaces $r_{j+1}(k)$ in Eqn. 4.11. Again, the subscript j denotes the cycle index and k denotes the time index within the cycle. Rather than directly optimizing $\theta_d(k)$ for all discrete points $k = 1,2,\ldots,N$ in a cycle, parameterization reduces the design space and optimization terms for this problem, creating a tractable problem for online implementation. The Fourier series was selected

to parameterize $\theta_d(k)$ due to its innate ability to approximate periodic functions. Further, as the Fourier series is made up of infinitely differentiable trigonometric functions, $\theta(k)$ and all of its higher order derivatives can be defined using the same basis parameters, increasing the cost function design space without increasing the number of optimization variables. However, it should be noted that any type of parameterization restricts the form of the path and may result in a sub-optimal reference.

The highest order derivative of the trajectory variable, in this case $\ddot{\theta}_d$, is defined using the Fourier series and the lower order terms $\dot{\theta}_d$ and θ_d are defined through integration, where

$$\ddot{\theta}_d(k) = \ddot{h}(k)^T \Gamma \tag{4.26a}$$

$$\dot{\theta}_d(k) = \dot{h}(k)^T \Gamma + \omega \tag{4.26b}$$

$$\theta_d(k) = h(k)^T \Gamma + \omega k + \sum_{n=1}^{m} \frac{\gamma_{n,1}}{(n\omega)^2} - \pi \tag{4.26c}$$

with $\ddot{h}(k)$ and the basis parameters Γ given as

$$\begin{aligned} \ddot{h}(k) = [1 \;\; \cos(wk) \;\; \sin(wk) \;\; \cos(2wk) \;\; \sin(2wk) \\ \ldots \;\; \cos(m*wk) \;\; \sin(m*wk)]^T \end{aligned} \tag{4.27}$$

$$\Gamma = [\gamma_0 \;\; \gamma_{1,1} \;\; \gamma_{1,2} \;\; \gamma_{2,1} \;\; \gamma_{2,2} \;\; \ldots \;\; \gamma_{m,1} \;\; \gamma_{m,2}]^T. \tag{4.28}$$

The form of $\dot{h}(k)$ and $h(k)$ follow directly from integration of Eqn. 4.27. In Eqn. 4.26b, the constant of integration is w which denotes the desired average velocity setpoint. The subscript j is not used for this term as the assumption of a steady state operating point is made. Similarly, in Eqn. 4.26c, the summation of the Γ terms corresponding to cosine terms in $h(k)$ ensures the position at k=0 is $-\pi$ radians, meaning the piston is at bottom dead center (BDC). If a nonzero ECL is desired, the value can then become $-(\pi + ECL)$ for the intake crankshaft, ensuring the intake reference trails the exhaust reference by the desired ECL. In Eqn. 4.27 ω is the same as defined above and can also be given as $\omega = 2\pi f \Delta t$ where f is the frequency of the periodic function and Δt is the sampling period. The number of frequencies contained in the Fourier series parameterization is denoted by m and the number of basis parameters is equal to $2m+1$. This tunable parameter m presents a trade-off between the computational burden and precision of the path parameterization which will be discussed further in the results section. It is also important to note the 0^{th} harmonic, or the DC component, of the Fourier series defining acceleration. This is the first term in the inner product shown in Eqn. 4.26a and is equal to γ_0. This value is used

to set the mean of the Fourier series over a given period and for the following steady state analysis is set to 0.

4.6.2 Cost Function Derivation

The objective of this optimization process is to maximize the system efficiency. This can be approximated by minimizing any losses from the electric motors as they absorb the torque generated by the engine, assuming a fixed fueling input. While this neglects any possible indicated efficiency improvements for the engine, it was shown in Chapter 3 that the motor efficiency is the dominant term for intra-cycle efficiency. This leaves the thermal efficiency to be improved through inter-cycle operation, which is outside the scope of this Chapter. Therefore, this problem, for each crankshaft independently, can be stated mathematically as

$$\min_{\Gamma} J = \sum_{k=1}^{N} P_{loss,j}(k) \tag{4.29}$$

To transcribe this optimization problem into the form provided in Eqn. 4.10, the power loss term, P_{loss}, needs to be expressed in terms of the basis parameters Γ. As this term represents instantaneous power lost through the electric motors when extracting work from the crankshaft, it is defined as

$$P_{loss,j}(k) = \frac{3}{2} i_j(k)^2 R + C(\dot{\theta}_{d,j}(k) - e_j(k))^2 \tag{4.30}$$

which accounts for the resistive and frictional losses of the electric motor. The winding resistance is denoted as R and the coefficient C is used to scale the friction losses by the true rotational velocity where $\dot{\theta}_j(k) = \dot{\theta}_{d,j}(k) - e_j(k)$ with $e_j(k)$ representing velocity tracking error. The quadrature current, $i(k)$, of the electric motors is proportional to the torque generated through the relationship

$$i_j(k) = \frac{T_{m,j}(k)}{9\lambda_m} \tag{4.31}$$

where λ_m represents the flux-linkage of the motor windings due to the permanent magnets and iron in the motors and T_m is the motor torque. For the specific electric motors, the values of $R = 23.3 * 10^{-3}$ Ω, $C = 0.038$ and $\lambda_m = 0.137$ Nm/A are used. Now, we can use Eqn. 4.30 and 4.31 to write the power loss function in terms of $T_m(k)$ and $\dot{\theta}_d(k)$. However, $T_m(k)$ is the control input to the system, obtained from feedback control which is a function of the crankshaft motion defined in Chapter 3. Therefore, the lower level control law for

tracking the desired reference, defined by the expression

$$T_{m,j}(k) = \hat{T}_{eng,j}(k) - I\ddot{\theta}_{d,j}(k) + K_{e,j} \tag{4.32}$$

can be used to replace $T_m(k)$ as a function of $\ddot{\theta}_d(k)$. The value $\hat{T}_{eng}(k) - I\ddot{\theta}_d(k)$ represents the feedforward term based on an approximation of engine torque and the desired crankshaft acceleration multiplied by the rotating inertia of the system, I, while K_e represents the error feedback value accounting for any errors in the torque estimation. Now, changes in $\theta_d(k)$ can be used to manipulate the required $T_m(k)$ for control and improve the work extraction efficiency, resulting in a power loss function of

$$\begin{aligned} P_{loss,j}(k) = &\frac{R(\hat{T}_{eng,j}(k) - I\ddot{\theta}_{d,j}(k) + K_{e,j})^2}{54\lambda^2} \\ &+ C(\dot{\theta}_{d,j}(k) - e_{v,j})^2. \end{aligned} \tag{4.33}$$

Substituting in the trajectory parameterization defined in Eqn. 4.26 and expanding the squared terms in the Eqn. 4.33, the cost function in terms of Γ can be defined as

$$\begin{aligned} J = \sum_{k=1}^{N} \big(&\beta_{q2}\Gamma_j^T \ddot{h}(k)\ddot{h}(k)^T\Gamma_j + \beta_{q1}\Gamma_j^T \dot{h}(k)\dot{h}(k)^T\Gamma_j \\ &+ \beta_{l2,j}\Gamma_j^T \ddot{h}(k) + \beta_{l1,j}\Gamma_j^T \dot{h}(k) + c_j\big) \end{aligned} \tag{4.34}$$

where the β coefficients are defined as

$$\beta_{q2} = \frac{RI^2}{54\lambda^2} \tag{4.35a}$$

$$\beta_{q1} = C \tag{4.35b}$$

$$\beta_{l2,j} = -\frac{2IR}{54\lambda^2}(\hat{T}_{eng,j} + K_{e,j}) \tag{4.35c}$$

$$\beta_{l1,j} = 2C(\omega_{set} - e_{v,j}) \tag{4.35d}$$

$$\tag{4.35e}$$

and the term c, although independent of Γ and not influential on the optimization, is included here for completeness as

$$\begin{aligned} c_j = &\frac{R}{54\lambda^2}\left(T_{eng,j}^2 + K_{e,j}^2 + 2T_{eng,j}K_{e,j}\right) \\ &+ C\left(\omega_{set}^2 + e_{v,j}^2 - 2e_{v,j}\omega_{set}\right). \end{aligned} \tag{4.36}$$

Note, for the β coefficients scaling the quadratic Γ terms, the cycle index dependence can be dropped as these coefficients are constant. Further, as the basis parameters Γ are time invariant during a cycle, they can be moved outside of the summation term in Eqn. 4.34, thus recovering the form provided in Eqn. 4.10.

4.6.3 ECL Constraint

The previous section provides the parameterized cost function for a single independent motor/crankshaft coupling. However, if the relative motion between the two crankshafts in this hybrid OP engine design is to be constrained, the power loss term should be duplicated for the second crankshaft, which is trivial as the dynamics are identical. This results in a cost function

$$\min_{\Gamma} J = \sum_{k=1}^{N} \left(P_{loss,j}^{exh}(k) + P_{loss,j}^{int}(k) \right) \tag{4.37}$$

where the superscripts denote the exhaust and intake crankshafts and each term can be expressed in terms of Γ using Eqn. 4.34 and 4.35. However, each crankshaft will use independent Γ parameters as each motion profile can be unique, increasing the number of basis parameters now to $q = 4m + 2$.

With each crankshaft included in the optimization problem, the ECL reference can be fixed at certain points during the cycle using the parameterized form of $\theta_d^{exh}(k) - \theta_d^{int}(k) = ECL$ to populate $A \in \mathbb{R}^{g \times q}$ and $b \in \mathbb{R}^g$ defined in Eqn. 4.10 where q is the number of parameters and g is the number of constraints. Intake and exhaust port closing was selected as the point to constrain the ECL as this point in the cycle is highly influential on the breathing dynamics while also determining the trapped volume and thus the effective compression ratio of the engine. Additional points could be selected if necessary, but optimization results show little fluctuation elsewhere in the cycle. Additionally, to ensure a constant average velocity during steady state operation, the value of γ_0 for both the intake and exhaust crankshafts is constrained to 0, which sets the total acceleration of a cycle to 0.

4.7 Results and Discussion

This trajectory learning method was tested experimentally under both motored and fired conditions at a speed setpoint of 1600 RPM. For steady state operation, the learning algorithm was triggered once every 30 cycles to reduce the computational load on the dSPACE Microlabbox and allow any tracking error to reach a steady state point before

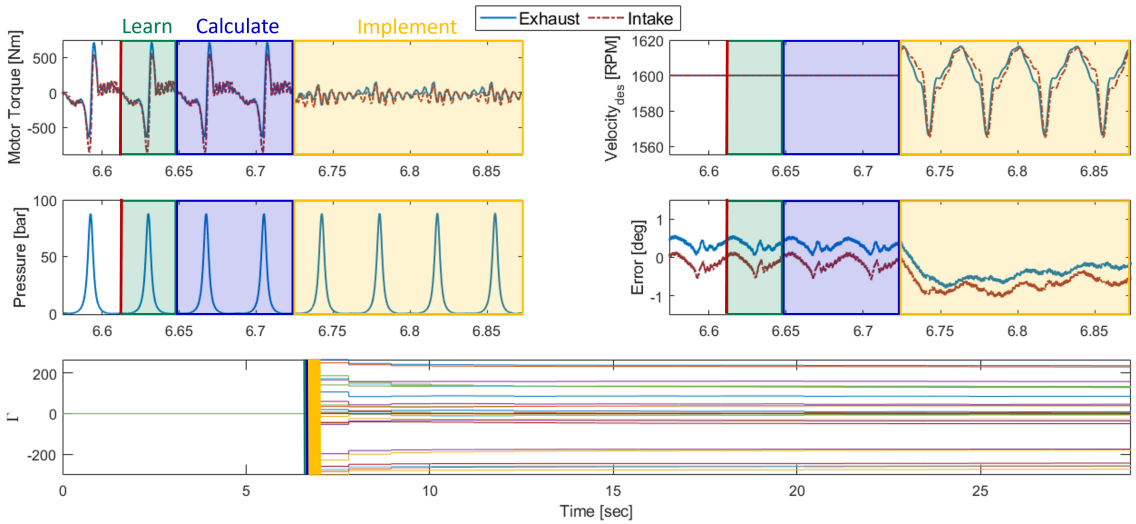

Figure 4.4: Results detailing the transition to a learned motion profile at a 4 degree ECL. (a) Motor control torque used to track desired trajectory. (b) Velocity reference. (c) Cylinder pressure. (d) Tracking error of crankshaft. (e) Evolution of the basis parameters during larger timescale to show the rapid convergence of parameters.

triggering an additional learning cycle. The sampling rate used for collecting measurements for Eqn. 4.23 and 4.24 is 5 kHz. For the motored test, an ECL of 4 degrees was maintained to demonstrate the ability to learn with a nonzero ECL present. A value of $m = 6$ is used for this test. During the fired tests, engine out power was held constant at 35 kW and the ECL was set to 0 degrees. Results quantifying the ITO performance are provided from averaged results of 950 cycles. Note that a positive motor torque denotes work being extracted from the engine, and a negative torque denotes work being put into the engine.

4.7.1 Motored Conditions

The results in Fig. 4.4 showing the transition from a constant velocity crankshaft motion reference to a motion reference learned using the ITO method for a motored case. The first highlighted section identifies the cycle over which Eqn. 4.23 and 4.24 were calculated. The next cycles are then used to calculate Γ_j and then near the 6.72 second mark, the new reference trajectory is implemented at BDC of the exhaust crankshaft. From Fig. 4.4a it is apparent the learned trajectory provides a drastic reduction in the motor torque required for tracking control of the crankshaft motion while still maintaining an acceptable level of tracking error of less than ± 1 degree for crankshaft position, shown in Fig. 4.4d. This follows again the conclusions in Chapters 2 and 3 that a near constant motor torque profile maximizes the work extraction efficiency. The new crankshaft velocity reference, provided

in Fig. 4.4b, shows the optimal velocity reference fluctuates nearly opposite that of cylinder pressure, shown in Fig. 4.4c, with a slight difference between the intake and exhaust crankshaft as each will experience a different engine torque due to the ECL. For a constant velocity reference, the motor is required to supply increasing torque to the crankshaft as cylinder pressure increases, only extracting work as each crankshaft passes top dead center (TDC). Rather, the learned trajectory allows the crankshaft to slow during compression and accelerate during expansion, smoothing out the motoring torque required to maintain an average cycle velocity. Further, as the ECL is maintained with the learned trajectory, there is negligible impact to the cylinder pressure after enabling learning.

The basis parameters, Γ, are shown in Fig. 4.4e over the full recording length rather than only the cycles where learning was enabled. As the quadratic β coefficients in Eqn. 4.35a and 4.35b are positive and the number of samples for each cycle is larger than the number of basis parameters used, the optimization problem given by Eqn. 4.10 is guaranteed to be strictly convex (see Proposition 1 in [35]). As such, the first values obtained for the Γ parameters are near the optimal location. However, as Eqn. 4.35c and 4.35d are time varying and dependent on measured values, a few learning iterations are required before Γ reaches steady state.

4.7.2 Fired Conditions

The ITO method can also be utilized during fired engine cycles to improve system efficiency while extracting positive work from the engine. Figure 4.5 provides a single cycle comparison of ITO method results under fired conditions with increasing values of m which denotes the number of frequencies contained in the Fourier series parameterization. This figure only shows the exhaust crankshaft results as each crankshaft operates similarly for the 0 ECL setpoint. A constant velocity baseline cannot be utilized here as the engine torque which the motor would have to match exceeds the capabilities of the electric motors. As m is increased, the trajectory can better approximate the ideal reference and a significant reduction in the peak-to-peak motor torque is achieved. The mean value of peak-to-peak torque amplitude from 950 engine cycles for each case is quantified in Tab. 4.2.

An additional performance index to quantify these results is the electric machine efficiency, and indeed from $m = 4$ to $m = 8$, there is an increase in efficiency of 9.1% for the mechanical to electrical conversion of power through the electric machines, including the inverter losses, as shown in Tab. 4.2. Further improvement beyond $m = 8$ is limited due to the quadratic computational complexity associated with the matrix multiplication required in Eqn. 4.23 and 4.24 which must be calculated at each sample point for the summation.

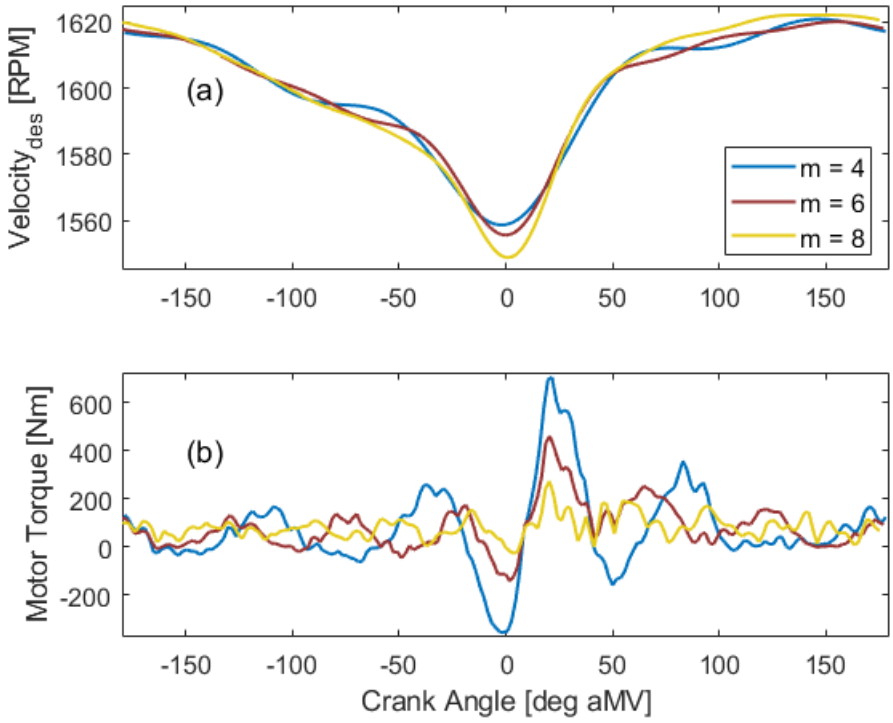

Figure 4.5: Single cycle results for the exhaust crankshaft of the (a) learned velocity reference and (b) required motor torque input for tracking the reference for fired cases at 1600 RPM and 35kW engine out power.

Table 4.2: Cycle average results for the fired cases over 950 cycles.

	$m = 4$	$m = 6$	$m = 8$
Motor Torque Amplitude [Nm]	1072.8	613.8	297.1
Electric Machine η [%]	72.3	78.0	81.4

However, it should be noted that this quantification of efficiency here underestimates the improvements capable for this system as the current motors are extremely oversized for the application. They were sized for peak torque rather than nominal power ratings with each AVID AF240 rated for a nominal power of 188 kW. The engine in this case is operating at a 35 kW setpoint, meaning each crankshaft is producing approximately 17.5 kW.

4.8 Transient Trajectory Planning

The theory behind ITO is largely based on iterative learning control, and as such, the usage of this ITO algorithm has focused on steady state operating conditions for the

hybridized OP engine where the previous cycle is always identical to the current cycle. As the proposed usage of this OP engine powertrain is in a series hybrid architecture, steady state operation characterises the majority of operating conditions for this system. However, there will inevitably be a need for this engine to transition between different operating states depending on the level of power demanded by the system, similar to series hybrid powertrains traversing an "optimal operating line" as discussed by Gupta et al. [67]. Therefore, it is relevant to provide a discussion of the practical capabilities and alterations of this ITO algorithm to change speed setpoints for the engine crankshafts which are outside the theoretical bounds placed on it through convergence proofs.

4.8.1 Inter-cycle Acceleration

In the Eqn. 4.26a, the 0^{th} harmonic is no longer set to 0 when defining the acceleration of the crankshafts. This value is used to set the acceleration, which will be denoted as α, over a single cycle. It is important to denote the distinction between $\ddot{\theta}$ which is the instantaneous crankshaft acceleration at each k point in a cycle, and the average acceleration of a cycle, α. Now, when changing the velocity of the crankshafts, several cycles of the engine will occur during the transition to the new setpoint. The most simple setting for α during this transience would be a constant value for every cycle. However, an instantaneous change in acceleration can be overly demanding for the lower level position regulator of the system. Rather, to smooth the change of speed, a sigmoid function is used to define the velocity trajectory rather than a ramp function, meaning the derivative of a sigmoid function will define the average cycle acceleration over the transient period. The sigmoid function is given as

$$\sigma = \frac{1}{1+e^{-x}} \tag{4.38}$$

and the derivative of the sigmoid function given as

$$\dot{\sigma} = \frac{1}{1+e^{-x}}\left(1 - \frac{1}{1+e^{-x}}\right) \tag{4.39}$$

which, when x is centered around a value of 0, provide a profile as shown in Fig. 4.6. In this figure, σ represents the normalized shape of the inter-cycle velocity trajectory of the engine crankshafts between two engine speed setpoints if the inter-cycle acceleration trajectory is assumed to be represented by $\dot{\sigma}$. Using this function shape, it is clear to see that the velocity presents a smooth transition between two setpoints.

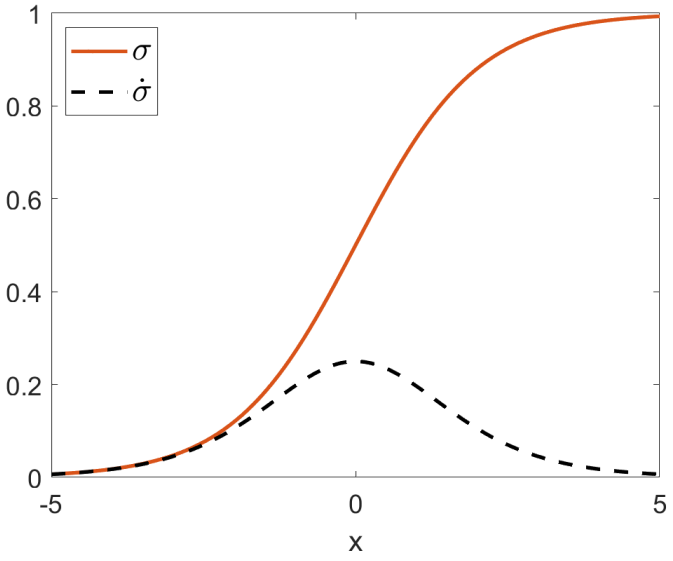

Figure 4.6: Values for σ and $\dot{\sigma}$ when the x value is centered around 0. Here, σ represents the shape of the inter-cycle velocity trajectory between two setpoints, while $\dot{\sigma}$ represents the inter-cycle acceleration trajectory.

To apply this to the crankshaft acceleration term, the variable x_ω is defined as

$$x_\omega = \frac{\Delta\omega}{2} - (\omega - \omega_j) \tag{4.40}$$

which creates an indexing variable centered around 0 and dependent on the new engine speed setpoint, ω, the actual current average cycle engine speed, ω_j, and the magnitude of the speed setpoint change, $\Delta\omega$. It should be reiterated here that the velocity term ω used without a subscript is the desired steady state velocity setpoint. The velocity term with the subscript j denotes the varying, intermediate velocity setpoints used to traverse between steady state setpoints. Then, each time the exhaust crankshaft reaches BDC, the average acceleration for that cycle can be updated using

$$\alpha_{j+1} = m\frac{1}{1+e^{-x_\omega}}\left(1 - \frac{1}{1+e^{-x_\omega}}\right)\text{sgn}(\Delta\omega_{\text{set}}) \tag{4.41}$$

where m is a scaling factor for the engine acceleration and $\text{sgn}(\Delta\omega_{\text{set}})$ is used to account for cases of deceleration. A scaling factor of 400 is used in this case.

4.8.2 Cycle-to-Cycle Transition

With the inter-cycle acceleration profile now defined, it is important to account for the non-zero average intra-cycle acceleration and how that effects the intra-cycle crankshaft motion defined in Eqn. 4.26. While the position of the crankshafts will always traverse through a full 360 degrees of rotation, the time in which that rotation takes will start to change as the engine speed, and therefore the frequency of the periodic functions in Eqn. 4.27, will change from cycle-to-cycle. Therefore, to find the timespan of each new cycle, constant acceleration dynamics of

$$2\pi = \omega_{j+1}\Delta t_{j+1} + \frac{\alpha_{j+1}\Delta t^2}{2} \tag{4.42}$$

can be used to solve for Δt_{j+1}, the time elapsed for cycle $j+1$, using the quadratic form

$$\Delta t_{j+1} = \frac{-\omega_{j+1} + \sqrt{\omega_{j+1}^2 + 4\pi\alpha_{j+1}}}{\alpha_{j+1}}. \tag{4.43}$$

Similarly, as the motion profile defined by Eqn. 4.26 includes a 0^{th} harmonic to induce a non-zero acceleration, the starting value of velocity for a given cycle will not match its ending velocity. Ideally, the average velocity for the intermediate cycles between setpoints, ω_j, could be set to the value defined by the sigmoid function in Eqn. 4.38 similar to the method of defining the average acceleration. However, to avoid over-defining the trajectory, the initial velocity setpoint of the current cycle can be defined by using Eqn. 4.26b with k set to 0 and $\dot{\theta}_{d,j+1}(0)$ set to the value of $\dot{\theta}_{d,j}(N)$ where we are using the subscript j to again define the cycle index and N is the last time index within a cycle. Then, solving for ω_{j+1}, Eqn. 4.26b becomes

$$\omega_{j+1} = \dot{\theta}_{d,j}(N) - \dot{h}(0)^T\Gamma \tag{4.44}$$

However, when Eqn. 4.27 is integrated to find $\dot{h}(k)$ as

$$\dot{h}(k) = \left[k \quad \frac{\sin(\omega_{j+1}k)}{\omega_{j+1}} \quad \frac{-\cos(\omega_{j+1}k)}{\omega_{j+1}} \quad \frac{\sin(2\omega_{j+1}k)}{2\omega_{j+1}} \quad \frac{-\cos(2\omega_{j+1}k)}{2\omega_{j+1}} \cdots \quad \frac{\sin(m*\omega_{j+1}k)}{m*\omega_{j+1}} \quad \frac{-\cos(m*\omega_{j+1}k)}{m*\omega_{j+1}}\right]^T \tag{4.45}$$

it is apparent that $\dot{h}(0)^T\Gamma$ will contain a w_j term, even when $k = 0$. This can be accounted

for by defining $\dot{h}(0)^T\Gamma$ as

$$\dot{h}(0)^T\Gamma = \frac{1}{\omega_{j+1}} \sum_{i=1}^{m} \frac{-\Gamma(2i+1)}{i}. \tag{4.46}$$

Now, the value of ω_{j+1} can be solved for as a quadratic equation similar to the elapsed time for each cycle.

Now that the cycle time, average velocity, and average acceleration can be determined for each cycle, this transient trajectory planning can be applied to the experimental system with the results shown in Fig. 4.7. As the engine speed changes from 1600 to 2000 RPM during fired conditions, the average crankshaft velocity is increasing as required to make the desired speed change. However, the intra-cycle variations of crankshaft velocity are still present to smooth the torque throughout the transient operation. Therefore the motor torque amplitude remains between $\pm$300 Nm. Further, tracking error is maintained at low enough values to maintain combustion and stable engine operation. Note, however that the tracking error does grow as speed changes, as shown in Fig. 4.7. This is due to the increased engine friction at higher speeds. As this is not modeled in the feedforward term detailed in Chapter 3, the integrator in the feedback term must grow to compensate for this DC component in the tracking error. Increasing the integrator gain could reduce the time required for this error to move back to near 0 values.

4.9 Conclusion

In this Chapter, a novel method of optimizing the tracking reference for a repetitive system by formulating the cost as a QP problem was developed. Constraints can then be applied to meet cycle requirements, enabling the use of Fourier series parameterization for the trajectory and reducing the number of optimization variables. Then, this theory was applied as a method for learning, in real-time, the optimal crankshaft motion profile of a hybrid opposed piston engine. The ITO method can be implemented with little prior knowledge of the system and reduces the need for offline optimization and the impact of model uncertainty on online performance. The effectiveness of the learning algorithm is dependent largely on the precision of the trajectory parameterization which is limited by the computational time allowed by the physical system. Utilizing the experimental test cell detailed previous chapters, the rapid convergence and near optimal crankshaft motion profiles for the ITO strategy as well as its proficiency under both motored and fired cycle operation was demonstrated.

This and previous chapters have focused largely on the intra-cycle operation of the dual-

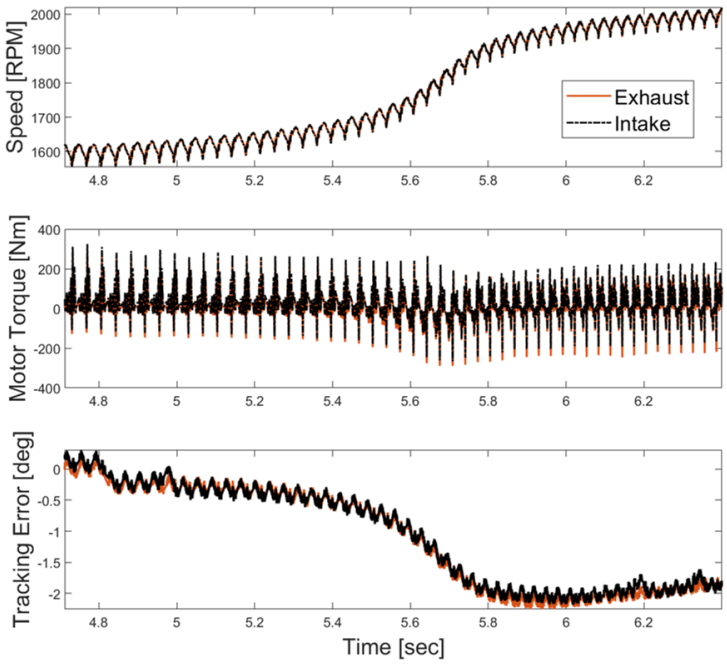

Figure 4.7: Results for a transition between engine speed setpoint of 1600 to 2000 RPM. The average velocity of the crankshafts increase between each cycle, but the intra-cycle velocity trend observed for steady state operation is still present. This allows the motor torque amplitudes to remain small. Further, the tracking error is maintained within sufficient limits to maintain stable operation.

motor hybrid OP engine. With the implementation of the ITO scheme to determine the near optimal crankshaft motion in real time, focus can now shift to the inter-cycle opportunities possible with this powertrain.

CHAPTER 5

Inter-Cycle Operation of an Opposed Piston Engine Range Extender

This chapter presents the exploration and local optimization of the hybridized opposed piston (OP) engine operation at two constant power operating points. In previous chapters, the feasibility of controlling the motion of the two crankshafts separately was demonstrated, introducing the ECL as a controllable parameter in the hybridized OP engine which allows for variation in the effective compression and expansion ratio of the engine, along with scavenging performance. The introduction of this novel control actuation as well as the adjustable speed and load setpoint in a series hybrid OP engine powertrain architecture necessitates intensive calibration effort to realize any possible efficiency improvements. However, the OP engine within this series hybrid powertrain does not operate in highly transient conditions, but rather its operating point is fixed or slowly varying. This property permits using online calibration techniques. After manually sweeping speed and ECL values at two power setpoints, the use of an extremum seeking type inter-cycle optimization algorithm to optimize the operating setpoint is validated.

5.1 Introduction

Rigorous calibration effort is usually carried out during the development phase of an engine to determine the best combination of actuator set points at each operating point. Traditionally, engine calibration was done by discretizing the control parameter space and sweeping the entire resulting grid on an engine dynamometer experimental setup. The calibration goal is to realize the target performance metrics such as fuel consumption, emissions, and transient performance [28]. Nevertheless, this method searches all combinations of control parameters and thus suffers from the curse of dimensionality and clearly is not an economic method to calibrate modern ICEs with various control

actuators. Advanced calibration techniques use Design of Experiments (DOE) [68] along with optimization and extreme seeking methods [30] to reduce the required effort. These methods often use the DOE concept to produce a sizable set of data points for engine operation that will be used for training data driven models or tuning physics-based models of the engine [69, 70]. These models are used as a surrogate for the engine dynamometer testing and are coupled with optimization algorithms in the next step to find the best actuator set points. This process is usually executed offline but the solution is eventually validated through experiments. Different surrogate models are used in literature for this purpose such as 1D GT-Power models [71, 72], data driven models such as neural networks [73], Gaussian process [74], and NARX models [75]. Gradient free approaches such as genetic algorithms are among the most popular optimization algorithms used for offline calibration of ICEs [72, 73]. Yu et al. [28] provides a comprehensive survey on calibration methods for internal combustion engines.

Recently, a new group of intelligent calibration schemes have emerged that are capable of finding the optimal operation parameters on-board [28]. These methods can adapt the engine calibration to aging [76] and driving style of the driver [77, 78] and thus provide a more optimal operation compared to offline calibration. Moreover, in a range extender powertrain as instantaneous vehicle speed and load are decoupled from the engine operating point, the engine's operational envelope can be limited to what is referred to as the optimal operating line rather than a complete operating map [67]. This line defines a single speed and load setpoint that minimizes fuel consumption for each power setpoint of the engine. Therefore, on-board calibration is a suitable choice for the opposed piston engine in a range extender configuration since it would reduce the development time of the engine significantly.

Similar to offline calibration schemes, some on-board calibration methods incorporate a model of the engine in their algorithm. These methods formulate the engine calibration as an optimal control problem to be solved online [79, 80]. These schemes need extensive modeling effort and the quality of the calibration solution that they find depends on the accuracy of the models. The model-free extremum seeking methods address these issues by iteratively perturbing the operating variables and monitoring the response [30, 81, 82]. However, these approaches can be slow for on-board calibration if not designed well. As an example, the automated engine calibration method introduced by Ma et al. [83] takes around 20 minutes to find the best set of actuator set points for one engine operating point. To overcome this deficiency Tan et al. [84] introduced a model guided extremum seeking approach to optimize the fuel injection timing of a diesel engine. In a different direction Malikopoulos et al. [77] modeled the engine operation as a Markov decision problem, in

which the states are the engine operation and the actions are calibration parameters. The authors proposed a Predictive Optimal Stochastic Control Algorithm (POSCA) to solve the Markov decision problem. Although this method is capable of adjusting the engine calibration to the style of the driver, it suffers from the curse of dimensionality and thus the authors proposed a decentralized learning control scheme in a later work to address this issue [32]. Further, this method also requires an initial full exploration of the operating space to populate the reward matrix of the Markov decision problem.

In this chapter, the model-free setpoint optimization strategy proposed by Gupta et al. [67] is leveraged to determine the optimal speed, load, and exhaust crankshaft lead of an opposed piston engine. This method finds the optimal actuator setpoints efficiently by estimating the gradient of the performance metric with respect to control parameters. This calibration approach is modified and adapted for an opposed piston engine and the effectiveness of the method is experimentally demonstrated on an physical engine test bench, which to the authors' knowledge, has not yet been completed. Therefore, an abbreviated experimental sweep of speed and ECL settings are completed at two separate power setpoints to find the optimal combination of speed and ECL. These two points are used to validate the onboard setpoint optimization and evaluate the practicality of this onboard setpoint optimization process for a hybridized opposed piston engine powertrain.

5.2 System Description

A schematic of the experimental test setup used in this work is provided in Fig. 5.1. This is the same experimental setup as used in previous chapters, but Fig. 5.1 now highlights the specific locations for power measurements of interest for this study. A compression ignition strategy using F-24, which is a base of commercial Jet A aviation fuel plus additives, was employed for this testing using a single injection strategy with a fuel rail pressure of 1000 bar. This is an important distinction from previous chapters which utilized gasoline for the compression ignition combustion. An external air handling system as well as an external oil and coolant system are used to maintain relevant operating conditions for the hybrid system. The following sections describe the relevant experimental setup. Discussion of the control structure and trajectory planning for the crankshaft motion regulation through the electric machines can be found in previous chapters.

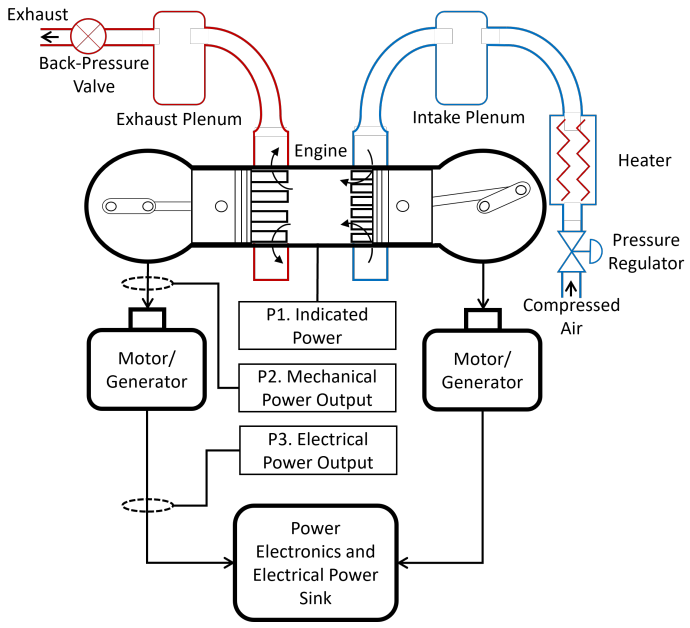

Figure 5.1: Layout of the experimental test cell including the air handling system as well as specific locations of power measurements within the system.

5.2.1 Air Handling System

Air is supplied by an external screw type compressor which maintains a 250 gallon air tank to the desired reservoir pressure (350 kPa). This then feeds the conditioning system consisting of a 20 kW air heater, and a pressure regulation valve as shown in Fig. 5.1. The engine intake air pressure at the intake plenum is controlled via the pressure regulation valve while the intake air temperature is maintained at 30°C, or 303 K for all tests. Air flow through the engine is controlled with the exhaust throttle valve. In-cylinder pressure is measured with an AVL GH14D pressure transducer while the intake and exhaust manifold pressures are measured using Kistler 4045 series sensors.

An objective of this chapter is to evaluate the benefits of dynamically varying ECL and how that impacts the thermal efficiency of the system along with the auxiliary power required to supply sufficient boost pressure to the engine. As air is supplied to the single cylinder engine from an external compressor in this experimental setup, a turbocharger model is augmented onto the experimental setup to determine a realistic back pressure on the engine. Furthermore, the two stroke single cylinder operation cannot sustain the power demanded by the compressor purely through work extracted from the exhaust by the turbine. Therefore, an electric turbocharger (e-turbo) model is assumed which can then quantify the auxiliary power needed to provide the required boost pressure.

First, to determine the back pressure on the turbine, an exponential fit was created to

obtain a pressure ratio across the turbine based on the mass flow through the engine. This fit was created using the turbine map from a Continental turbocharger used with the Ford EcoBoost 1.5L engines and is given as

$$\Delta p_{turb} = x_1 * \exp(\mathrm{x}_1 * \dot{\mathrm{m}}_{\mathrm{par}}) + \mathrm{x}_3 * \exp(\mathrm{x}_4 * \dot{\mathrm{m}}_{\mathrm{par}}) \tag{5.1}$$

where $\dot{m}_{par}$ is the corrected mass flow based on temperature and pressure with the units $[kg/hr * \sqrt{K}/bar]$ and the coefficients of x are given as $x = [0.64, 2.66e-4, 5.00e-15, 8.30e-3]$. The calculated back pressure on the engine is then controlled using the exhaust throttle valve.

The power recuperated through the turbine is calculated as

$$P_{\mathrm{turb}} = \dot{m}_{\mathrm{turb}} C_{\mathrm{p}} T [\Delta p_{\mathrm{turb}}^{\frac{k-1}{k}} - 1] * \eta_{\mathrm{turb}}. \tag{5.2}$$

where C_{p} is the specific heat of the exhaust, T is the temperature of the exhaust gases, and k is the ratio of specific heats, assumed to be 1.35 for the exhaust. The turbine efficiency, η_{turb}, is calculated based on an exponential fit of the same functional form as Eqn. 5.1 but as a function of the turbine pressure ratio rather than corrected mass flow with coefficients $x = [5.84, -1.86, -8.50e-3, 15.00]$. This fit is again based on the Continental turbocharger assuming the e-tubro design can maintain the maximum efficiency for all turbine speeds.

Then, the boost pressure required by the engine is determined by regulating the intake manifold pressure to maintain a desired delivered air-to-fuel ratio (AFR), which also determines the mass flowrate through the compressor. With the boost pressure and flow rate specified, the power consumption of the compressor can be calculated using the same equation as shown in Eqn. 5.2 but with a ratio of specific heats of 1.4 and by dividing by the compressor efficiency. Compressor efficiency is again determined by a exponential fit as in Eqn. 5.1 and as a function of mass flow through the compressor. The coefficients are given as $x = [0.85, -1.27, -1.13, -34.16]$.

At steady state conditions, the power consumed by the compressor can be assumed equal to the power generated by the turbine. However, as this is a two-stroke, single cylinder engine and the power extracted from the exhaust by the turbo may not provide enough power to the compressor to maintain the desired boost pressure, the power balance now becomes

$$P_{\mathrm{comp}} = P_{\mathrm{turb}} + P_{\mathrm{aux}} \tag{5.3}$$

where P_{comp} is the power required by the compressor, and P_{aux} is the auxiliary power required by the e-turbo to provide the remaining power to the compressor. This provides a

quantifiable power loss associated with the demanded boost pressure for the engine.

5.2.2 Efficiency Calculations

Now, the power measurements and efficiencies of interest can be defined using the locations denoted in Fig. 5.1. The net indicated thermal efficiency (ITE) is calculated by integrating the indicated power, denoted as P1 in the figure, and dividing by the fuel energy added to the system as

$$\eta_{\mathrm{ITE}} = \frac{\int_{-\pi}^{\pi} P \mathrm{d}V}{m_{\mathrm{f}} Q_{\mathrm{LHV}}} \tag{5.4}$$

where P is the cylinder pressure, V is the cylinder volume, m_{f} is the quantify of fuel injected each cycle, and Q_{LHV} is the lower heating value of the fuel. Similarly, the mechanical brake thermal efficiency ($\mathrm{BTE}_{\mathrm{mech}}$) is quantified using the cycle average mechanical output power P2 as

$$\eta_{\mathrm{BTE}} = \frac{\mathrm{P2}/\omega_{\mathrm{eng}}}{m_{\mathrm{f}} Q_{\mathrm{LHV}}} \tag{5.5}$$

where ω_{eng} is the engine speed. The auxiliary power consumed by the e-turbo can by included in this BTE calculation by subtracting P_{aux} from P2.

It is worth noting here that the mechanical-to-electrical conversion efficiency of the motors on each crankshaft were neglected in this analysis, meaning the value of P3 in Fig. 5.1 is not used. Due to the severe oversizing of the electric machines, their losses dominate the efficiency map when included. Any sensitivity to changes in ECL is overwhelmed by the efficiency improvement of the electric machine at lower speeds. As such, motor efficiency is neglected here to focus on the OP engine operating characteristics with the ability to dynamically vary the ECL setpoint.

5.3 Engine Performance

For the validation of the onboard setpoint optimization algorithm proposed by Gupta et al. [67] and Filev et al. [31], a set of ECL and engine speed sweeps were completed for a pair of electrical output power setpoints of 16 and 28kW. The range of variables swept is detailed in Tab. 5.1 along with the delivered air to fuel ratio (AFR) and location of 50% fuel mass fraction burned (CA50) maintained over the sweeps. It should be noted that the ECL setpoints of -4 and -2 degrees were not used with the 2000 and 2200 RPM setpoints due to excessive combustion noise. The location of CA50 was controlled rather than the timing of fuel injection to minimize the effect of combustion phasing on system efficiency over a range of speeds. The delivered AFR was set to 30 as this reduced concern for soot

Table 5.1: Experimental Engine Sweeps

Test Variable	Setpoints
Engine Speed [RPM]	1200, 1400, 1600, 1800, 2000, 2200
ECL [deg]	-4, -2, 0, 2, 4, 6, 8
CA50 [deg]	6
AFR [-]	30
Brake Electrical Power [kW]	16, 28

generation. Further, by fixing the delivered AFR, the efficiency trade-off between ECL and boost pressure can be evaluated. In a two-stroke OP engine, there is no pumping stroke for the engine and the air flow through the cylinder is controlled by the pressure ratio between the intake and exhaust manifolds along with the relative area of exposed intake and exhaust ports. Typically, increasing the ECL provides a longer blowdown process and reduces the auxiliary pumping work required by the compressor. However, the advanced timing for opening the exhaust ports also reduces the expansion ratio of the engine, reducing the indicated thermodynamic efficiency [12].

5.3.1 Engine Sweep Results

5.3.1.1 16kW Power Setpoint

The results of the ECL and engine speed sweeps for the power setpoint of 16kW are shown in Fig. 5.2. In each subfigure, the efficiency of the system is evaluated at different power take-off locations. The operating point of 1800 RPM and 4 degree ECL is used as the baseline point with all other points represented as a difference in efficiency from the baseline. In Fig. 5.2 (a), the ITE of the OP engine is shown to be relatively flat with the peak efficiency near the operating point of 1400 RPM and 0 deg ECL. As speed decreases, heat transfer increases, reducing the ITE. Additionally, increasing ECL reduces the expansion ratio of the engine, while decreasing the ECL reduces the trapped volume and therefore the effective compression ratio of the engine.

Figure 5.2(b) shows the variation in the mechanical BTE where the output power is considered the mechanical power output from the engine crankshafts, labeled P2 in Fig. 5.1. While there is little sensitivity in the mechanical BTE to changes in ECL until the low speed range, speed has a larger impact. As speed decreases from 1800 RPM, the mechanical BTE increases, as would be expected due to the reduced frictional losses. Similarly, increasing

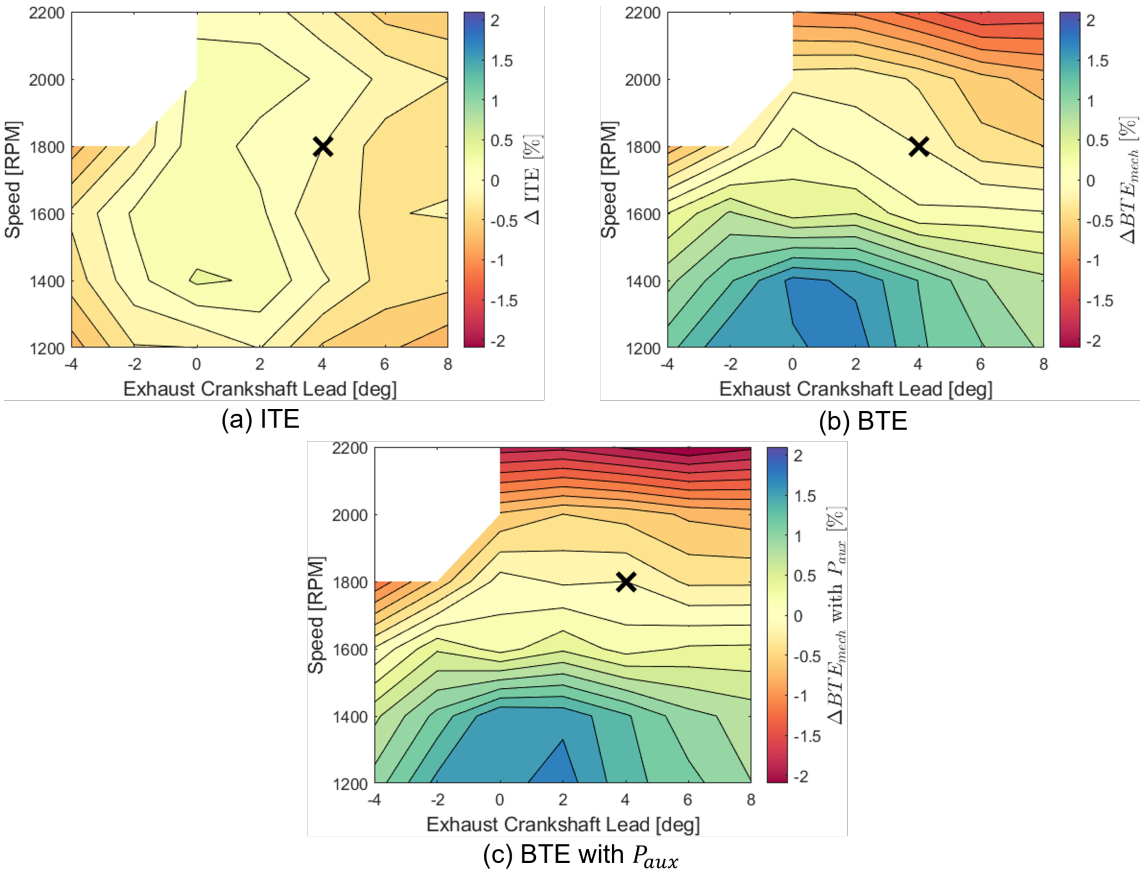

Figure 5.2: Results from engine sweeps for the 16 kW power setpoint. The results shown are the (a) indicated thermal efficiency (ITE), (b) brake thermal efficiency (BTE) with output power measured at the engine crankshafts, and (c) BTE with power measured at the engine crankshafts while also including the auxiliary power loss due to the e-turbo. The efficiency values are normalized with respect to the baseline operating point denoted by the black "X". The increase expansion ratio maintains the optimal ECL near 0 to 2 degrees while friction losses drive the speed to the minimum setpoint. Auxiliary power demand from the compressor narrows the ideal operating range for the ECL to 2 degrees.

speed to 2200 RPM exhibits a near 2% decrease in the mechanical BTE. At low speeds, the influence of the ECL on effective compression and expansion ratio of the engine discussed previously limits the optimal ECL to between an ECL of 0 and 2 degrees. However, at the optimal speed setpoint of 1200 RPM, the range in BTE over the full ECL range is only 0.9%.

Then, in Fig. 5.2(c), the auxiliary power required by the e-turbo to supply the required boost pressure is also included in the BTE calculation. While the contour plot remains largely unchanged with the optimal operation located at the minimum speed of 1200 RPM, the maximum BTE starts to shift towards higher ECL points, centered around 2 degrees

ECL rather than the 1 degree ECL when neglecting the e-turbo auxiliary power. These results illustrate a trade-off between the larger expansion ratio of the engine achieved at smaller ECLs, the peak compression ratio near 4 degrees for this port design, and the reduced boost pressure required at larger ECLs. However, the impact on the location of the optimal operating point is small.

5.3.1.2 28kW Power Setpoint

The same set of speed and ECL points as discussed for the 16kW power output setpoint were also run at a higher power of 28kW with the results shown in Fig. 5.3. The ITE results show a similarly flat operating map with higher indicated losses experienced at low speeds and ECL. This is expected at higher power setpoints as the low speed increases heat transfer loses. Furthermore, as noted by Niak et al. [12], the required blowdown period, the time when only the exhaust ports are open after combustion to allow the burnt gasses to exit the engine cylinder, is proportional to the fuel energy released during combustion. At this higher power setpoint, the low and even negative ECL setpoints limit this gas exchange process and push the optimal ECL to near 2 degrees.

In Fig. 5.3 (b), the peak mechanical BTE is no longer at the minimum speed of 1200 RPM but increased to 1400 RPM due to the higher heat transfer losses at low speeds. However, the range of efficiency values across this operating map is reduced as compared to the 16kW setpoint. For the 28kW setpoint, the mechanical BTE values have a range of 2.9% compared to the 3.4% range at 16kW.

In Fig. 5.3(c), when incorporating the e-turbo power into the BTE calculation, the optimal ECL shifts higher to 4 degrees, again illustrating the trade-off between the power required for boost pressure and the improved indicated efficiency for low ECL points. Compared to the 16 kW operation, the sensitivity to changes is ECL is decreased at 28kW. At 1400 RPM, there is a range of 1.5% for the BTE values in Fig. 5.3 (c). The range in efficiency values at the optimal speed for the 16 kW operation is 1.7%. While this is a rather small difference, this reduced sensitivity to operating conditions impacts the real-time optimization procedure discussed in later sections of this work.

Figure 5.4 provides a more explicit comparison of the impact of ECL on expansion and compression ratio, as well as the auxiliary power. Auxiliary power is plotted for each power setpoint at the 1200 RPM speed setpoint. As the ECL increases, the compression ratio increases until an ECL of 4 degrees. Past this point, the increasing ECL starts to shrink the trapped volume of the engine as the exhaust ports are starting to close before the intake ports. Similarly, the auxiliary power required decreases until around 4 degree ECL. Then, as the exhaust ports now start to close before the intake, the time period in which both

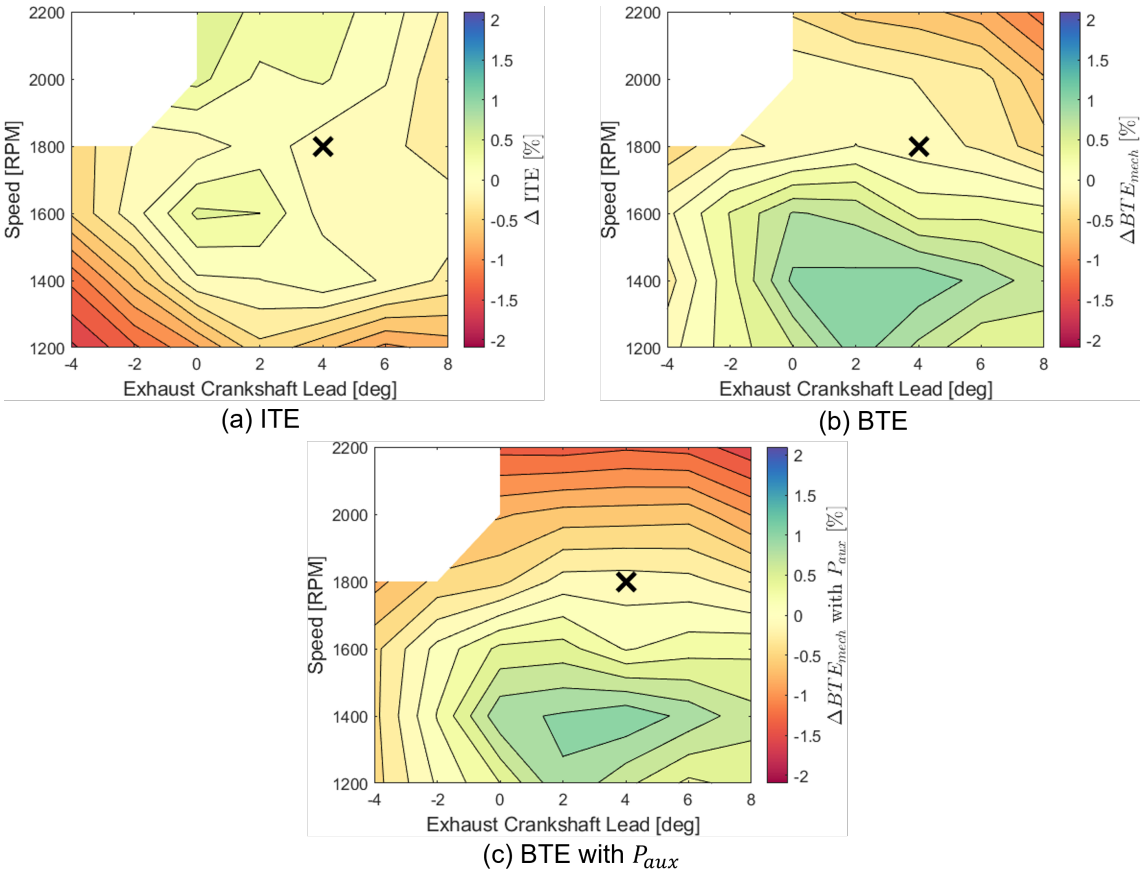

Figure 5.3: Results from engine sweeps for the 28 kW power setpoint. The results shown are the (a) indicated thermal efficiency (ITE), (b) brake thermal efficiency (BTE) with output power measured at the engine crankshafts, and (c) BTE with power measured at the engine crankshafts while also including the auxiliary power loss due to the e-turbo. The efficiency values are normalized with respect to the baseline operating point denoted by the black "X". At the higher power setpoint, the optimal ECL shifts to to higher values betwee n 2 and 4 degrees will the optimal speed also increases to 1400 RPM due to the increased heat transfer losses.

ports are simultaneously open starts to shrink. For the expansion ratio, the exhaust port will always open first, meaning increasing ECL creates a continual decline in expansion ratio.

With the sweeps of the hybrid OP engine system completed for two power setpoints, the learning methodology to calibrate the system operation can now be validated.

5.3.2 Setpoint Optimization

Using the information provided by the initial baseline testing of the hybrid OP engine, the approach to engine calibration proposed by Gupta et al. [67] and Filev et al. [31] can now be validated. This methodology consists of two parts as highlighted in Fig. 5.5 which

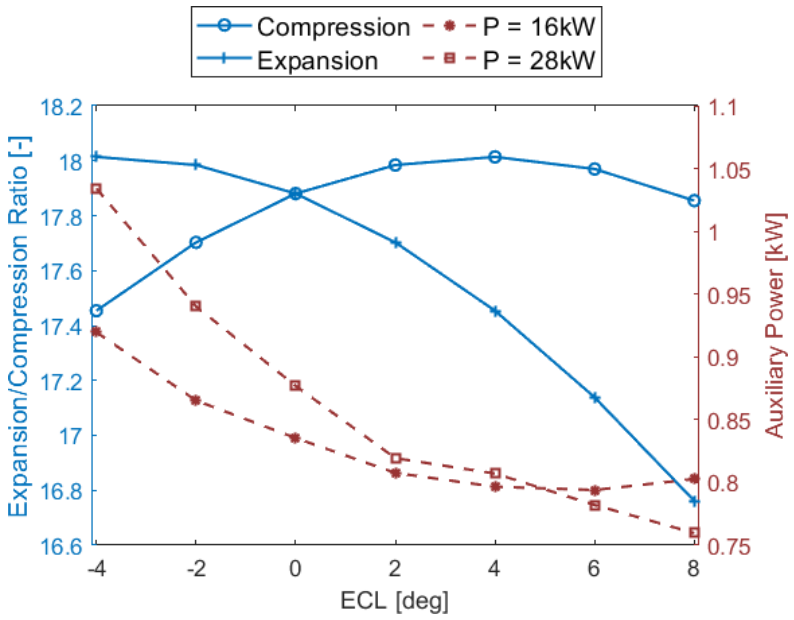

Figure 5.4: Comparison of the effects of ECL on compression ratio, expansion ratio, and the auxiliary power required for the demanded boost pressure at 1200 RPM for each power setpoints. The peak compression ratio occurs near a 4 degree ECL while the expansion ratio decreases with increasing ECL, similar to the required auxiliary power.

provides a block diagram to show how the onboard setpoint optimization methodology was implemented. First, an approximate model relating the engine output to changes in engine input must be learned from measured real-time values. In this case, the output is considered the brake specific fuel consumption (BSFC) and the inputs are engine speed and ECL. Second, constrained optimization utilizing the learned model updates the control inputs to improve system performance while remaining within safe operating limits. The value of BSFC is used rather than BTE as minimization of BSFC fits more readily into the optimization scheme proposed while accomplishing the same goal of maximizing BTE. The following sections further develop the methods used in the onboard learning and setpoint optimization.

5.3.2.1 Jacobian Learning

For this model approximation, the engine is assumed to be a nonlinear but smooth system represented as

$$y = F(u, p) \tag{5.6}$$

where u is the control input, $u = [N \quad ECL]^T$ and p is the power setpoint of the engine. The output, y, is the BSFC of the system, calculated as

$$\text{BSFC} = \frac{\dot{\text{m}}_{\text{fuel}}}{\text{P}_{\text{out}}} \tag{5.7}$$

where P_{out} is the power output from the mechanical system, including the auxiliary power losses.

To simplify the optimization problem and make it tractable for online implementation, a surrogate model linearized about the current operating point is defined as

$$\Delta y(k) = \hat{J}_u \Delta u(k) + \hat{J}_p \Delta p(k) \tag{5.8}$$

where the changes of these values are represented as

$$\begin{aligned} \Delta y(k) &= y(k) - y(k-1) \\ \Delta u(k) &= u(k) - u(k-1) \\ \Delta p(k) &= p(k) - p(k-1). \end{aligned}$$

The estimated Jacobians of the system, $\hat{J}_u$ and $\hat{J}_p$, are defined as

$$\hat{J}_u = \frac{\partial y}{\partial u} \quad \hat{J}_p = \frac{\partial y}{\partial p}$$

and represent the change in the output y due to changes in the control input and power setpoint. As y is the scalar output of BSFC, $\hat{J}_u$ is a row vector and $\hat{J}_p$ is a scalar.

To estimate the value of the Jacobians, Kalman filtering is applied to a linear system given as

$$\begin{aligned} \hat{J}_i^T(k+1) &= \hat{J}_i^T(k) + w(k) \\ \Delta y(k) &= \Delta i^T(k) J_i^T(k) + v(k) \end{aligned} \tag{5.9}$$

which can be obtained using the relation described in Eqn. 5.8 and rearranging to represent the individual components of the Jacobian as the linear system states. The term $i \in [u, p]$ as each Jacobian can be found separately as detailed elsewhere [31]. The variable $w(k)$ represents process noise while $v(k)$ is the measurement noise. The Kalman filter updates

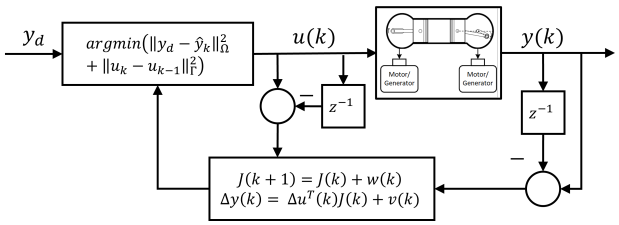

Figure 5.5: Block diagram showing the implementation of the setpoint optimization technique. Feedback values are used along with a Kalman filter to estimate a linearized approximation of the system. Constrained optimization is then performed with this approximation to determine the control inputs for the system.

for the Jacobians follow as

$$\begin{aligned} \hat{J}_i^T(k+1) = \hat{J}_i^T(k) + P_i(k)\Delta i(k)(\Delta y - \Delta i^T(k)\hat{J}_i^T(k))... \\ (R_i + \Delta i^T(k)P_i(k)\Delta i)^{-1} \\ P_i(k+1) = P(k) + Q_i - (P_i(k)i(k)i^T(k)P_i(k))... \\ (R_i + \Delta i^T(k)P_i(k)\Delta i)^{-1} \end{aligned} \tag{5.10}$$

where Q_i represents the variance of the process noise and R_i the variance of the sensor noise. As these values are not completely known, they can be determined through heuristic tuning. Filev et al. [31] use the value of Q_i in a similar manner as the forgetting factor in other parameter identification schemes such as recursive least squares. If changes in the control update cause large changes in the estimated Jacobian, decreasing the value of Q_i can slow the learning rate of the Kalman filter. While this can avoid poor estimates in the Jacobian for large changes in control input, it also limits the convergence rate of the Jacobian estimation.

Remark 1. As noted by Filev et al. [31], an advantage in the use of a Kalman filter is that the Jacobian can be estimated using only the general input excitation when other system identification techniques require a persistent excitation term in the system input. However, in this experimental implementation, an additional persistent excitation term is found to be beneficial for exploration of the control space, especially during the initialization period when knowledge of the Jacobian is weak.

Remark 2. Different values of Q_i were used for learning the response to changes in speed and ECL. As the system efficiency has a generally weaker response to changes in ECL and also a heavy dependence on the engine speed, it is advantageous to have the setpoint algorithm converge to a speed setpoint faster than the ECL setpoint. As such, the value of Q_u corresponding to the change in ECL is set to 0.001 while the value

Table 5.2: Jacobian Learning Parameter Values

Parameters	Values
Q_u	[0.01 0; 0 0.001]
Q_p	0.0001
R_u	15
R_p	15

corresponding to the change is speed is set to 0.01. The values used for the tunable parameters within the Kalman filter are provided in Table 5.2.

Now, with values for the estimated Jacobians relating changes in control and power setpoints to changes in BSFC, a constrained optimization problem can be formulated to minimize BSFC.

5.3.2.2 Constrained Optimization

Using the linear model described in Eqn. 5.8, the objective of the optimization problem is to find the optimal control inputs $u(k)$ defined by

$$u(k) = argmin(||y_d - \hat{y}(k)||^2_{\Omega} + ||u(k) - u(k-1)||^2_{\Gamma}) + r(k) \tag{5.11}$$

where $r(k)$ is the persistent excitation term on the control inputs. This term is defined as

$$r(k) = [A_N(k)(W_N - 0.5) \quad A_{ECL}(k)(W_{ECL} - 0.5)]^T \tag{5.12}$$

with $A_N(k)$ and $A_{ECL}(k)$ representing the range of the persistent excitation term on engine speed and ECL, respectively. The W_N and W_{ECL} terms are randomly generated values between 0 and 1. The cost function, the function within the *argmin* operation in Eqn. 5.11, can be written as

$$\begin{aligned} F = &(y_d - \hat{y}(k))^T \Omega (y_d - \hat{y}(k)) + \\ &(\Delta u(k))^T \Gamma (\Delta u(k)) \end{aligned} \tag{5.13}$$

where y_d is the desired BSFC output value. The purpose of the first term in the cost function is to penalize the difference between the desired output value, y_d, and the estimated value $\hat{y}(k)$. The second term penalizes the difference between the previous and current control input values. The relative importance of these penalties is determined through the Ω and Γ weighting factors. In this case, as the output is BSFC, $y_d = 0$. As there is only one

Table 5.3: Quadratic Programming Parameter Values

Parameters	Values
Ω	37
Γ	[300 0; 0 1150]
$A_N(k)$	10 RPM
$A_{ECL}(k)$	0.25 degrees

output value, Ω is a scalar weighting factor to penalize the size of the estimated BSFC, $\hat{y}(k)$. However, the transpose terminology is kept to maintain generality in the problem derivation. Similarly, using the positive definite weighting matrix Γ, the rate at which the input values are changed can also be penalized to limit the control step sizes. Too large of a change in the control input results in the local Jacobian estimates no longer being valid, but small step sizes increase the time spent at sub-optimal control setpoints.

Remark 3. Heuristic tuning of the the weights of Ω and Γ, as used in this work, can be a time consuming process. The value of Ω should be large enough to influence the system performance without being concealed by the persistent excitation term. However, too large of an Ω value can cause large steps in the control input value, drastically changing Jacobian values and providing poor robustness against noisy measured performance values. Similarly, Γ should be sized large enough to limit the step size of the control values without allowing the persistent excitation to be the dominant factor in the control input. The values utilized here for Ω and Γ as well as the persistent excitation term are given in Table 5.3.

To find the current control input $u(k)$, the cost function needs to be a quadratic function with respect to $u(k)$, meaning the estimate of $\hat{y}(k)$ should be replaced by

$$\hat{y}(k) = y(k-1) + \hat{J}_u(\Delta u(k)) + \hat{J}_p(\Delta p(k)). \tag{5.14}$$

Combining Eqns. (5.13) and (5.14), the cost function can be written in a conventional quadratic programming problem (QP) form of

$$\min_{u(k)} \quad F = \frac{1}{2}u^T(k)Hu(k) + g^T u(k) \tag{5.15}$$

where the terms H and g are defined as

$$H = 2(\hat{J}_u^T \Omega \hat{J}_u + \Gamma) \tag{5.16}$$

$$\begin{aligned} g =& 2((-y_d^T + y^T(k-1) - (\hat{J}_u u(k-1))^T \\ &+ (\hat{J}_p \Delta p)^T)\Omega \hat{J}_u - u^T(k-1)\Gamma)^T \end{aligned} \tag{5.17}$$

Furthermore, linear constraints can be included in the QP problem to restrict the range of the inputs $u(k)$. These bounds are defined as

$$[1200 \quad -4]^T \leq u(k) \leq [2200 \quad 8]^T \tag{5.18}$$

where speed is given in RPM and ECL in degrees. To solve this optimization problem in an online manner, the Matlab function "quadprog" was used with the active-set algorithm due to the constraints.

Remark 4. Changing the input values of speed and ECL will create small disturbances in the BSFC and power output of the system. Therefore, the setpoint optimization algorithm is only updated once every 300 engine cycles to allow the system to settle after each input change.

Remark 5. In the implementation described in Filev et al. [31], all control values contained in u are changed at each iteration of the algorithm. However, this can obfuscate the response of the system to any one particular input. As such, the manipulated control input is alternated for each iteration in this work, meaning only one control variable changes at a time.

5.4 Results

The learning algorithm described in the previous section was implemented on the hybridized opposed piston engine at the same two power setpoints where the engine sweeps were completed. At each power setpoint, the algorithm was initialized at a pair of sub-optimal speed and ECL operating points of 1800 RPM, 4 degree ECL and 2000 RPM, 6 deg ECL.

The dynamic response of the system to the learning algorithm starting at 1800 RPM, 4 degrees ECL at the 16 kW power setpoint is shown in Fig. 5.6. On the left, the evolution of the measured speed and ECL of the engine is shown. After each change in the speed setpoint, the torque produced by the engine must adjust to maintain a constant power output from the system. As the speed is shifted incrementally to lower values, the torque increases. By only running the optimization algorithm once every 300 cycles, the controller regulating the power output of the hybrid powertrain has time to adjust the fuel input to the system, increasing the torque and maintaining the 16 kW electrical output power. On the right of Fig. 5.6, the engine speed setpoint starts by taking small steps around the initial 1800 RPM

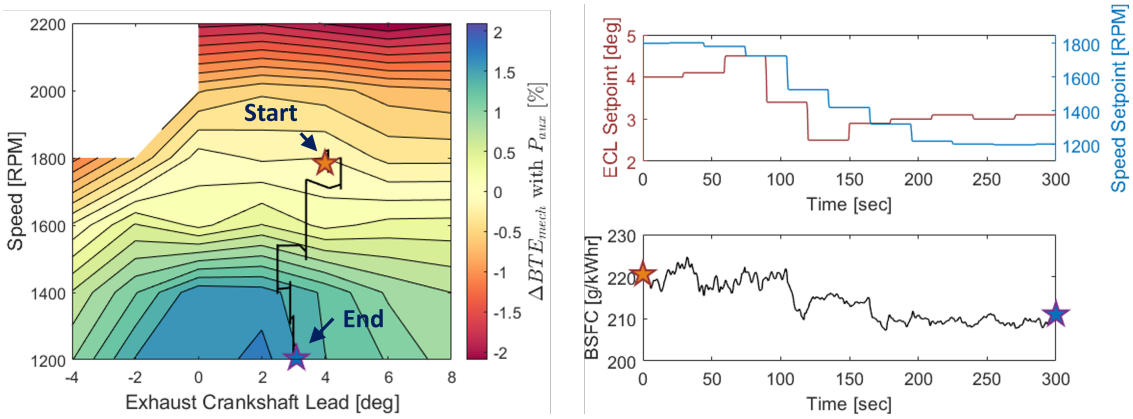

Figure 5.6: Learning trajectory of the system at a 16 kW setpoint using an initialization of 1800 RPM and 4 degree ECL. On the left, the evolution of engine speed and ECL are provided to show how the system can maintain a constant output power. On the right, the trajectories for the ECL and speed setpoints are provided, along with the BSFC at each setpoint. The BSFC shows a fairly constant decrease as the setpoint optimization algorithm adjust speed and ECL towards the optimal setpoint.

setpoint, largely motivated by the excitation term in the control input. However, the speed quickly starts to decrease towards the minimum speed of 1200 RPM, which in the case of the 16kW power setpoint is the optimal speed point. At 1800 RPM, ECL has little impact on the system and starts to drift upwards. However, as speed decreases, so does ECL, eventually settling around 3 degrees which is close to the optimal ECL setting of 2 degrees as shown in Fig. 5.2.

Next, at the 16 kW operating setpoint, the speed and ECL were initialized at 2000 RPM and 6 degrees ECL. Shown in Fig. 5.7, after an initial increase in speed, it decreases monotonically to the optimal speed of 1200 RPM. However, ECL takes a much longer time to converge. As discussed previously, the learning rate for ECL was tuned to be slower than that of speed as the response of BSFC to changes in ECL can vary according to the speed setpoint. Similarly, from the BSFC plot in Fig. 5.7 it is evident that speed has a much larger impact on efficiency than ECL does. As ECL decreases, as it starts to do near 800 seconds, the required boost pressure decreases, decreasing the auxiliary power required to drive the compressor. However, this also increases the expansion ratio of the engine. As show in Fig. 5.2 c, while an ECL of 2 degrees provides the highest efficiency for the system, between 6 and -2 degree ECL at 1200 RPM, there is only a range of 0.2% BTE efficiency when including the auxiliary power. This is reflected in the near constant BSFC curve as the ECL setpoint decreases in Fig. 5.7. However, the poor performance of the engine at large negative ECL values prevents the learning algorithm from passing below a -2 degree

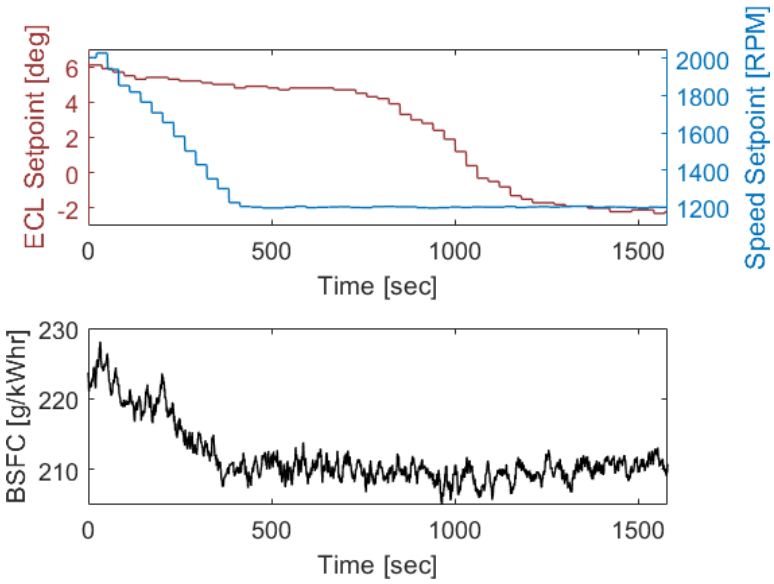

Figure 5.7: Learning trajectory of the system at a 16 kW setpoint using an initialization of 2000 RPM and 6 degree ECL. The top figure shows the trajectory of the ECL and speed setpoints. The lower figure displays the corresponding BSFC. The speed of the engine is adjusted more rapidly than the ECL due to the tuning of the Kalman filter for Jacobian approximation. The BSFC response is much more sensitive the changes in engine speed do to the relatively flat efficiency map corresponding to ECL at 1200 RPM.

ECL. It is worth noting here the relatively noisy BSFC used by the learning algorithm to adjust the estimated Jacobian for the system. To reduce the impact of noise on the learned values, a moving window average of the past 45 cycles is used when evaluating the change in BSFC from one control input to the next. Further, while the learning algorithm converged in approximately 5 minutes from the first setpoint, it took nearly 25 minutes for the system to converge from the speed and ECL setpoint that were further from the optimal operating point. Yet, when only evaluating the convergence rate of BSFC, the performance metric of interest, the BSFC converges to its minimum point at similar rates for each case. Although the ECL takes a long time to converge, it has little impact on performance.

After implementing the learning algorithm at two different initialization points at 16kW brake power output, the power level was increased to 28kW and the same initialization points were analyzed. Figure 5.8 provides the ECL and speed trajectories as well as the BSFC response of the system when initialized at 1800 RPM and a 4 degree ECL. Again, the change in speed is quicker than that of ECL. However, in the case of the 28kW setpoint, the optimal speed is around 1400 RPM. The learning algorithm starts to slow the decent of speed as the engine approaches 1400 RPM, but continues on to 1200 RPM. As shown in Fig. 5.3, the operating map for the hybridized OP engine system at 28 kW is relatively

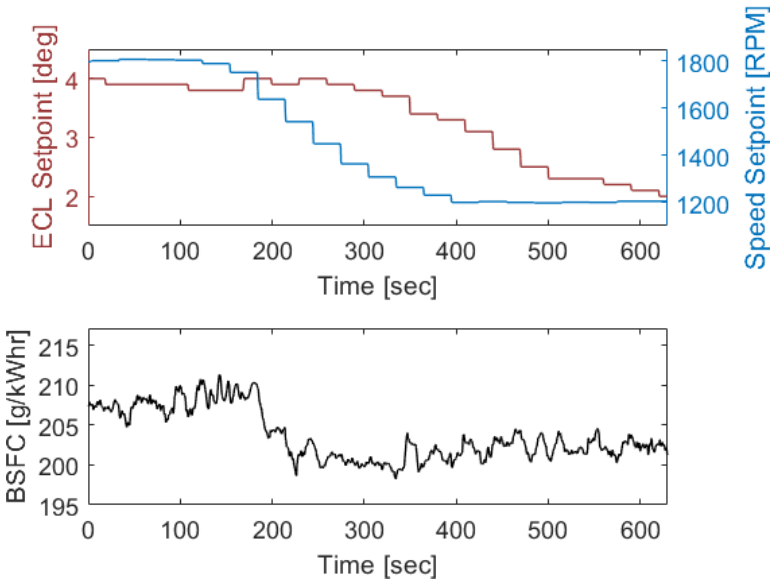

Figure 5.8: Variation in the control inputs and BFSC of the hybridized OP engine system implementing the setpoint optimization algorithm at an initialization point of 1800 RPM and 4 degree ECL for a 28 kW power setpoint. Speed passes the optimal operating point of 1400 RPM and settles on the boundary of 1200 RPM due to the relatively flat operating map. Changes in ECL slow near 2 degree ECL but make small continued steps downward as there is only a range of 0.9% in BTE between the ECL setponts of -2 to 8 degrees at 1200 RPM.

flat over the speed and ECL of interest. As such, the gradient of BSFC around 1200 RPM is not large enough to change the Jacobian value of the system approximation learned by the Kalman filter. Additionally, as a speed constraint of 1200 RPM is applied to the OP problem used to define the control input, only the persistent excitation term can shift the speed control off the boundary of the operating space. The noise associated with the BSFC values used by the learning algorithm are too large compared to the change in BSFC which can be attributed to the persistent excitation of 10 RPM used for the speed control. This poor signal to noise ratio limits the effectiveness of the learning algorithm when it reaches a boundary in a fairly insensitive portion of the operating map. The ECL setting during this process drifts slowly downward from an inital setting of 4 degrees. As there is only a range of 0.9% BTE at 1200 RPM, the ECL has little impact on fuel consumption for this operating point. The changes slow near 2 degrees, but still continue to drift slowly downward. The learning algorithm at this 28 kW operating setpoint also took over double the amount of time to reach a near optimal operating point than it did for the 16 kW setpoint with the same initialization point, highlighting again the relatively flat performance map of the engine at this power output.

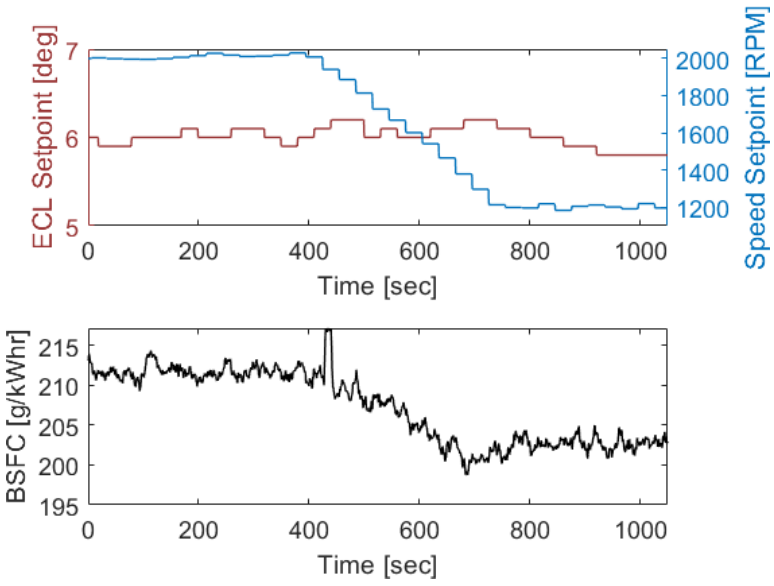

Figure 5.9: Variation in the control inputs and BFSC of the hybridized OP engine system implementing the setpoint optimization algorithm at an initialization point of 2000 RPM and 6 degree ECL for a 28 kW power setpoint. Again speed passes the optimal setpoint of 1400 RPM and settles at 1200 RPM. The setpoint of ECL oscillates around the original value of 6 degrees for the entire test due to the insensitivity of BSFC to ECL at this operating point.

Finally, speed and ECL were initialized at 1800 RPM and 6 degrees, respectively, for the 28 kW setpoint. The results of the speed and ECL setpoint along with BSFC are shown in Fig. 5.9. At this initialization point, both speed and ECL remain near the initial values for nearly 7 minutes. Finally, speed decreases from 2000 RPM and again passes the optimal 1400 RPM setting to stop at the 1200 RPM boundary. However, as shown in the BSFC response, fuel consuption decreased continually with speed. This indicates that 300 cycles between control input may not be a sufficient length of time to allow the BSFC to stabilize. Similarly, the ECL setpoint for this case has a negligible change from the initial setpoint due to the insensitivity of the system efficiency to changes in BSFC due to the trade-off between ECL's impact on ITE and the auxiliary power required to drive the compressor.

5.5 Conclusions

In this chapter, the inter-cycle operating characteristics of an opposed piston engine utilized in a range extender powertrain are investigated. Due to the decoupling of the crankshafts, the ECL becomes a novel actuator to improve the efficiency of the system, balancing trade-offs between ITE and auxiliary boost power requirements. Further, as the speed and load

setpoint of the engine are decoupled from the instantaneous power demand of the vehicle in this hybrid powertrain, a method of on-board learning of the optimal calibration of the speed and ECL setpoint is experimentally analyzed.

As shown in the initial speed and ECL sweeps, ECL becomes more influential on the BTE of the system at lower speed operating points. However, due to the trade-off between ECL and the auxiliary power required to produce the necessary boost pressure, the system remains relatively insensitive to changes in the ECL over the operating range investigated. While this resulted in poor convergence performance for the ECL input for the on-board learning algorithm, the BSFC of the engine was consistently decreased to near minimum values for the engine power setpoints analyzed.

CHAPTER 6

Control and Design Optimization of a Series Hybrid Powertrain

This chapter investigates the energy management and optimal powertrain and drivetrain component sizing to complete the discussion of a hybrid powertrain utilizing an OP engine in a series hybrid or range extender architecture. The motivation behind this final technical chapter is to provide a tool or process framework with which to integrate the hybrid OP engine operation into a full vehicle model, thereby elevating the usefulness of the previous chapters in this thesis. Therefore, a co-design problem combining the energy management and component sizing optimization is formulated and solved in this chapter. Of specific interest is the trade-off between the cost of fuel consumption of the OP engine and the cost of battery degradation in the hybrid powertrain.

6.1 Introduction

Transitioning to Electric Vehicles (EVs) presents a direct method of decarbonizing tailpipe emissions in the transportation sector and combating climate change. However, the adoption of EVs has been rather slow; such that in 2020 less that 2% of all vehicles sold in the U.S. were electric [85]. One of the key obstacles hindering widespread EV acceptance is their limited range causing range anxiety. While evidence suggests that a range of about 100 miles per charge will address most daily transportation needs [86], consumers usually prefer vehicles with substantially higher range [87]. A larger battery delivers a larger range at the cost of a larger ecological footprint [88], a higher energy consumption due to the higher weight, and a reduced affordability because of the higher initial cost. Therefore, from the environmental and economic point of view the smallest battery that provides sufficient range is the optimal battery size. This dilemma between EV range, cost, and environmental impact defines the EV range paradox, studied by Franke and Krems [89].

Range extender Hybrid Electric Vehicles (HEVs) address this paradox by including an onboard charging system to EVs while adopting the smallest battery size for daily needs.

It is shown that range extender HEVs can be even more effective when coupled with advanced highly efficient engine technologies [90]. This chapter studies the combined design and control optimization (co-design) for a range extender HEV coupled with an Opposed Piston (OP) engine. In an opposed piston engine, two pistons operate opposite each other to control the combustion chamber volume as defined in previous chapters. Due to the removal of the traditional cylinder head the heat transfer is significantly lower in OP engines leading to a higher thermal efficiency. Furthermore, the opposite movement of the pistons within these engines creates an intrinsic stability allowing a reduction in the displacement volume of the engine by reducing the number of cylinders rather than reducing the displacement of each cylinder resulting in a higher thermal efficiency again.

Optimal sizing and design of components that accounts for the dependency of optimal energy management strategies on the powertrain design is necessary to fully exploit the advantages of a flexible and highly efficient powertrain such as a range extender HEV. Combined design and control optimization (co-design) has been used in the past for finding the optimal sizing of HEV powertrain components [91, 92]. The traditional design approach designs the plant first and then the optimal control laws are found next. However, this sequential optimization does not consider the coupling between the plant design and control variables and produces a suboptimal solution [93]. The co-design methods on the other hand, incorporate these inter-dependencies by solving the optimal design and control problem simultaneously or by embedding the optimal control problem into the optimal design problem [93, 94].

The resulting co-design problem usually has a large dimensionality and is difficult to solve. To address this problem, Bayrak et al. [95] decomposed the co-design problem into hierarchical optimization problems and in another work [96] the authors used heuristic methods to search the design space of an HEV powertrain with nested Equivalent Consumption Minimization Strategy (ECMS). Convexification of the simultaneous optimal design and control problem [97, 98] and using gradient-free optimization techniques such as multiobjective self-adaptive differential evolution (MOSADE) [99] are among other approaches used to find solutions to the co-design problems of HEVs. Stochastic and robust combined design and optimization methods that account for the variations in the manufacturing process, model simplification, and the uncertainty surrounding vehicle operation have also been introduced for co-design of HEVs [100, 101]. A comprehensive review of system-level optimization for hybrid electric vehicles is provided by Silvas et al. [91].

However, few works detail the impact of battery capacity fade, or degradation, on the component sizing and energy management for an HEV. In most automotive applications, the battery pack is considered defunct when it reaches 80% of its original capacity. As the battery pack makes up a large portion of the principal cost for an HEV, minimizing fuel consumption of the internal combustion engine in the vehicle must be balanced with minimizing the capacity fade of the battery pack. As such, this chapter presents scalable models for each subsystem of an HEV suitable for nonlinear optimization techniques. The battery model is able to accommodate usage degradation to include the price of batteries within the cost function, while allowing the nominal state of charge (SOC) to shift and help reduce capacity loss. Then, a combined design and optimization method similar to the approach utilized by Azad and Alexander-Ramos [100] is used to integrate the OP engine, which has been the focus of this entire work, into an optimally sized series hybrid powertrain.

6.2 Combined Sizing and Control Optimization Problem

A schematic of the powertrain architecture is provided in Fig. 6.1 with the associated inputs, states, and parameters for each system component. This system consists of a OP engine coupled to electric motors on each crankshaft to act as a generator, a lithium-ion battery pack to buffer the power provided by the engine and store any recaptured power from regenerative braking, a traction motor to provide power to the wheels, and a gear set representing the final drive for the drivetrain. The objective of this optimization process is not only to coordinate the operation of the OP engine with the rest of the series hybrid powertrain, but also to size the components according to the vehicle and drive cycle demands. Therefore, the optimization problem can be formulated as

$$\begin{aligned} &\min_{d,u(t)} \quad J(d,x(t),u(t),t) \\ &\text{subject to :} \\ &g(d,x(t),u(t),t) \leq 0 \\ &h(d,x(t),u(t),t) = 0 \\ &\dot{x}(t) - f(d,x(t),u(t),t) = 0 \end{aligned} \tag{6.1}$$

where the function $J(d,x(t),u(t),t)$ represents the cost function of the optimization problem. This function is dependent on the sizing of the design parameters, d, the state

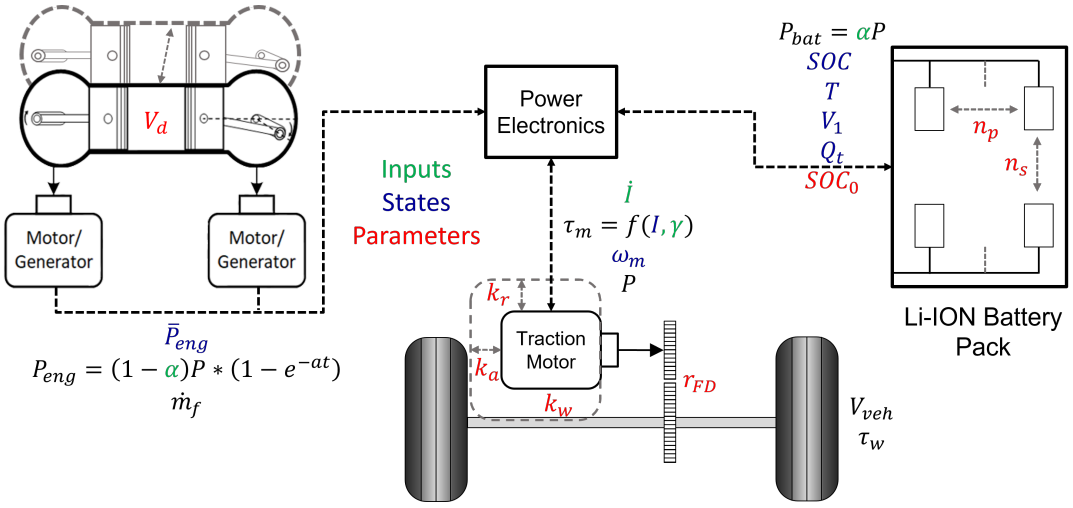

Figure 6.1: Schematic of the series hybrid vehicle model used for the component sizing and energy management analysis.

values, $x(t)$, and the control inputs, $u(t)$. This optimization problem is also subject to constraints defined by the functions g and h along with the system dynamics defined by the function f. The design parameters in this optimization problem are the displacement volume of the engine, V_d, the radial, k_r, axial, k_a, and winding, k_w, size of the traction motor, the final drive gear ratio, r_{FD}, the number of cells in parallel, n_p, and in series, n_s, in the lithium ion battery pack, and lastly the nominal SOC operating point of the battery pack, SOC_0. The states are the normalized engine power, $\bar{P}_{eng}$, the traction motor speed, ω_m, and current, I, along with the cell state of charge, SOC, temperature, T, voltage V_1 across the resistor, capacitor (RC) pair in the equivalent circuit model, and finally the accumulated charge throughput for each cell, Q_t.

6.2.1 Optimization Problem Formulation

In this analysis, the cost function will only account for the running cost of the vehicle and not the initial cost for all the components involved. As such, the cost function is defined as

$$J = \int_{t_0}^{t_1} \dot{m}_f p_f + \frac{\dot{Q}_{loss}}{20} Q_c p_c V_0 n_p n_s \tag{6.2}$$

where the first term represents the fuel costs of the engine from the mass flow rate of fuel, $\dot{m}_f$, and the price of fuel, p_f. The second term represents the battery degradation costs assuming the battery will be replaced after 20% capacity loss. The capacity loss is represented as $\dot{Q}_{loss}$ in [%/s]. In order to convert this to a cost equivalent to fuel price,

the nominal capacity of a cell within the pack, Q_c, is multiplied by the nominal operating voltage, V_0, providing a Watt hour, [Wh], value. This can then be used with the price of a cell, p_c, in [price/Wh] and the number of cells in the pack, n_c, to find the equivalent battery cost for the vehicle operation.

The system constraints are defined as

$$\dot{x} = f(d, x(t), u(t), t) \quad \forall t \in [t_0, t_1] \tag{6.3a}$$

$$x^{min} \leq x(t) \leq x^{max} \tag{6.3b}$$

$$u^{min} \leq u(t) \leq u^{max} \tag{6.3c}$$

$$|V_{veh}(t) - V_{dem}(t)| \leq V_{diff} \tag{6.3d}$$

$$V_{mot} \leq V_{mot,max} \tag{6.3e}$$

$$V_{bat} \leq V_{bat,max} \tag{6.3f}$$

$$|SOC - SOC_0| \leq SOC_{diff,max} \tag{6.3g}$$

$$SOC(t_1) - SOC(t_0) = 0 \tag{6.3h}$$

where Eqn. 6.3a represents the constraints of the vehicle dynamics while Eqns. 6.3b and 6.3c represent the limits on the state and control values. In Eqn, 6.3d, the vehicle velocity, V_{veh} is constrained to within a set difference of ± 2 mph from the demanded vehicle speed of the selected drive cycle, V_{dem}, at all times. The motor terminal voltage, V_{mot}, is constrained by a factor of the DC bus voltage in Eqn. 6.3e and the battery cell terminal voltage, V_{bat}, is constrained based on the cell chemistry. As this is a series hybrid vehicle model operating in a charge sustaining mode, the instantaneous SOC is constrained to $\pm 20\%$ around the nominal SOC operating range in Eqn. 6.3g. Finally, the initial and ending SOC must be equal as defined by Eqn. 6.3h.

6.3 Series Hybrid Model

The sub-models for all of the components shown in Fig. 6.1 as well as a vehicle model to provide the terms within the cost function and system dynamics defined in Eqn. 6.2, are provided in the following sections.

6.3.1 Vehicle Model

The longitudinal vehicle dynamics are given as

$$m_{eff}\dot{V}_{veh} = \frac{\tau_w}{R_w} - F_{RL} \tag{6.4}$$

which represents a force balance between the road load, F_{RL} and the torque applied to the wheels, τ_w, multiplied by the wheel radius, R_w. This then calculates the vehicle acceleration, $\dot{V}_{veh}$, given the effective mass of the vehicle, m_{eff}, is known. The effective mass takes into account the inertia of the rotating components as well as the vehicle mass and is given as

$$m_{eff} = m_v + \frac{J_w + J_m r_{FD}^2}{R_w^2} \tag{6.5}$$

where m_v is the vehicle mass while J_w and J_m are the inertia of the wheels and traction motor, respectively. The final drive ratio is denoted as r_{FD} and is a sizing parameter of the optimization process. The mass of the vehicle is a sum of the base vehicle weight along with the battery, engine, and motor components. The road load is calculated using

$$F_{RL} = C_0 + C_1 V_{veh} + C_2 V_{veh}^2 \tag{6.6}$$

where the coefficients C_0, C_1, and C_2 are the EPA reported dynamometer correction factors for a 2010 Nissan Leaf, the assumed vehicle model for this work.

The dynamics of the vehicle must now be linked to the traction motor operation, which is not obvious from Eqn. 6.4. However, the speed of the vehicle and torque applied to the wheels can also be converted into a motor torque and speed utilizing the final drive ratio. The longitudinal dynamics can then be converted to

$$\dot{\omega}_m = \frac{r_{FD}}{R_w m_{eff}} \left(\frac{\tau_m r_{FD}}{R_w} - F_{RL} \right) \tag{6.7}$$

where the motor toque, τ_m, can be determined from the current applied to the motor and motor speed, ω_m, is a state.

6.3.2 Motor

The traction motor model represents an interior permanent magnet synchronous machine (IPMSM) based in the 2004 Toyota Prius motor. This motor was selected due to the abundant literature detailing the operation of this machine design. The model selected from this work was developed by Goss et al [102]. Furthermore, to include the scaling

parameters outlined in Fig. 6.1, the electric machine scaling laws detailed by Stipetic et al. [103] are implemented. Nominally, axial and radial scaling factors are used to scale the performance capabilities and size of the electric motor while the winding factor adjusts the base speed of the electric machine to comply with the predetermined inverter voltage limit, in this case set to $\frac{V_{DC}}{\sqrt{3}}$ where V_{DC} is the bus voltage of the system, set to 500 volts as is similar to the work by Azad et al. [100]. The scaling laws will be defined after the model is outlined.

The electric motor torque is calculated as

$$\tau_{em} = \frac{3}{2} p(\Psi_d I_q - \Psi_q I_d) \tag{6.8}$$

where $\Psi_{d,q}$ are the direct and quadrature axis flux linkages, $I_{d,q}$ are the direct and quadrature axis currents and p denotes the number of pole pairs in the motor, which is 4 in this case. The current values in the rotating two-phase reference frame are calculated from the peak phase current, I_s as $I_d = -I_s \sin(\gamma)$ and $I_q = I_s \cos(\gamma)$ where I_s is a state and γ is an input to the model. The value of I_s is considered a state in this model and is obtained from the input $\dot{I}_s$ as this allows for constraints to be placed on the rate of change of the phase current and therefore the rate of change of torque developed from the electric machine. The input γ allow for the maximum torque per current input while also utilizing flux weakening at high speeds to maintain the voltage limit applied to the motor. The values of $\Psi_(d,q)$ are calculated from polynomial fits defined by Goss et al. [102] which are fucntions of $I_{d,q}$.

The peak phase voltage of the motor, V_{mot}, which must be constrained, is calculated as

$$V_{mot} = \sqrt{(R_{ph} I_d - \omega_{m,e} \Psi_q)^2 + (R_{ph} I_q - \omega_{m,e} \Psi_d)^2} \tag{6.9}$$

where R_{ph} is a per phase resistance, assumed to be 9.3 mΩ as from Goss et al. [102]. The electrical motor speed, $\omega_{m,e}$ is related to the mechanical speed of the motor through the pole pairs and is calculated as $\omega_{m,e} = \omega_m * p$.

With these dynamics, the electric machine torque and voltage can be calculated. However, the power loss of the motors must also be considered to determine the power requirements from the engine and motor. The power delivered to the motor is denoted as P and is positive when power is delivered to the wheels and negative during regenerative braking when power flows from the wheels to the motor. The power which reaches the motor is denoted as P_{em} and is related to P by

$$P = P_{em} + P_{cu} \tag{6.10}$$

where P_{cu} denotes the copper loss in the electric machine. The value of $P_{em} = \tau_{em}\omega_m$ while the copper losses are calculated as

$$P_{cu} = \frac{3}{2}R_{ph}(I_q^2 + I_d^2) \tag{6.11}$$

providing a means to calculate P, the combined power demanded from the battery and engine in the vehicle.

Finally, mechanical as well as core losses in the motor (P_{mech}, P_c), must be considered when calculating τ_m, the shaft torque of the motor that is translated to the wheels, from τ_{em}, the electric machine torque, similar to the modeling structure presented by Stipetic et al. [104]. The mechanical losses are calculated using a polynomial fit of the mechanical losses as a function of motor speed. These losses are based on a report from Hsu et al. [105] in which a Prius motor was dismantled and evaluated. The core losses are calculated as

$$P_c = g_1(V_{mot}) + g_2(V_d) \tag{6.12}$$

where V_d is the magnetizing voltage given as

$$V_d = -\omega_{m,e}(\Psi(I_d, I_q) - \Psi(0, I_q)) \tag{6.13}$$

and the functions g_1 and g_2 are defined by Goss et al. [102]. With the mechanical and core losses, an electric machine efficiency, η_{em}, can be used to find the output motor toque as

$$\tau_m = \tau_{em}\eta_{em}^{\text{sign}(\tau_{\text{em}})}. \tag{6.14}$$

Note, however, that this form of τ_m causes a discontinuity as τ_{em} crosses 0. Therefore, the function is modified with a hyperbolic tangent function as

$$\tau_m = \tau_{em}\eta_{em}^{-1} + \frac{1 + \tanh(10^4\tau_{\text{em}})}{2}(\tau_{em}\eta_{em} - \tau_{em}\eta_{em}^{-1}). \tag{6.15}$$

Now, to provide a scalable model of the motor, the pertinent scaling laws as detailed by

Table 6.1: Motor Parameters

Parameters	Values
Mass of copper (m_{cu})	0.5 [kg]
Mass of stator iron ($m_{fe,s}$)	19.0 [kg]
Mass of rotor iron ($m_{fe,r}$)	3.1 [kg]
Mass of permanent magnets (m_{mag})	0.6 [kg]
Inner Diameter of rotor (d_{ri})	13.7 [cm]
Outer Diameter of rotor (d_{ro})	16.1 [cm]

Stipetic et al. [103] are:

$$V_{mot} = k_w k_a k_r V_{mot,0} \tag{6.16a}$$

$$P_c = k_r^2 k_a P_{c,0} \tag{6.16b}$$

$$P_{mech} = k_r^2 k_a P_{mech,0} \tag{6.16c}$$

$$\tau_{em} = k_r^2 k_a P_{mech,0} \tag{6.16d}$$

$$m_{mot} = k_r^2 k_a m_{cu} + k_r^2 k_a (m_{fe,s} + m_{fe,r}) + k_r^2 k_a m_{mag} + m_h \tag{6.16e}$$

$$J_{mot} = \frac{1}{2}(k_r^2 k_a m_{fe,r} + k_r^2 k_a m_{mag}) 0.25((k_r d_{ri})^2 + (k_r d_{ro})^2) + 0.5\rho_s(\frac{\pi}{4}(k_r d_{ri})^2 k_a l)\frac{(k_r d_{ri})^2}{4} \tag{6.16f}$$

By only scaling the variables that interact with other model subsystems, the internal variables within the motor model, such as I_s, remain unscaled and the fitted functions for the motor model remain valid. These unscaled values calculate the base values, denoted by the subscript 0, as in the motor voltage $V_{mot,0}$. The mass and inertia of the motor, m_{mot} and J_{mot}, are dependent on the individual copper, magnetic, and iron components of the motor as well as the original dimensions of the motor. These values are provided in Tab. 6.1

6.3.3 Engine

The engine model used in this vehicle simulation uses an optimal operating line defined by the experimental work in Chapter 5. An optimal operating line (OOL), as defined by Gupta et al. [67], is a drive cycle independent operating map for an IC engine in which the operation of the engine has slow transients and the instantaneous speed and load of the engine is decoupled from the instantaneous vehicle demands, as in this vehicle architecture. The OOL defines the speed and load setpoint of the engine that provides the minimum BSFC for a given power setpoint. As such, to simplify the model used here for

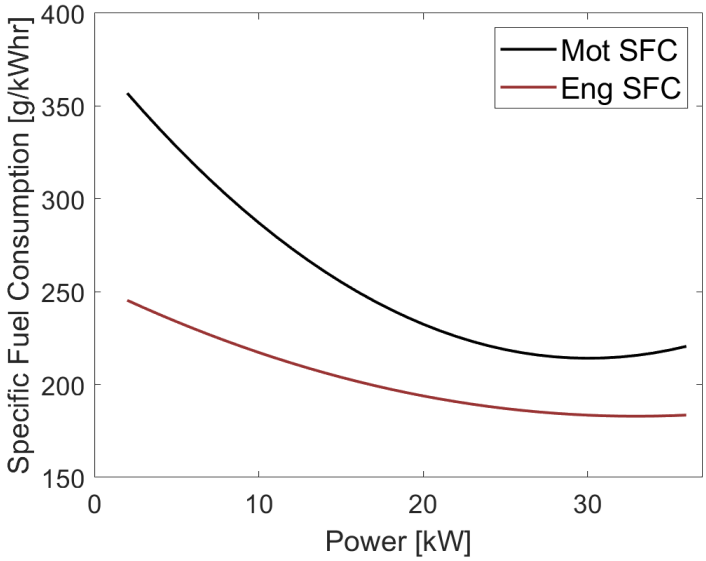

Figure 6.2: The minimum specific fuel consumption (SFC) of the OP engine can be defined using the online optimization process outlined in Chapter 5. The value of this line depends on the point at which the power is measured. The Eng SFC denotes the SFC with the power measured at the engine crankshafts. The Mot SFC denotes the power that is extracted from the system by the electric motors.

optimization, the speed and torque of the OP engine is not modeled. Rather, the power demanded from the engine is defined as

$$P_{e,dem} = (1-\alpha)P \tag{6.17}$$

where P is the power delivered to the motor as defined in Eqn. 6.10. The control input α defines the power split between the battery and the engine. The value of α ranges between -1:1 as the engine can deliver power to the motor and battery simultaneously, but is limited by the peak power of the engine. Utilizing the optimization methodology from last chapter, a relation between the minimum fuel consumption and the power output of the engine can be determined and is shown in Fig. 6.2. In this case, rather than considering just the power output from the engine as in Chapter 5, the motor efficiency must also be accounted for to determine the accurate fuel consumption. Therefore, the brake power is considered to be after the motor generators used to extract the power from the OP engine, shown as "Mot SFC" in the figure.

While the fuel consumption of the engine can now be determined, using the the BSFC and power relation shown in Fig. 6.2 is not conducive to optimization. If a power of 0 is demanded from the engine, the fuel consumption will be undefined as BSFC must be

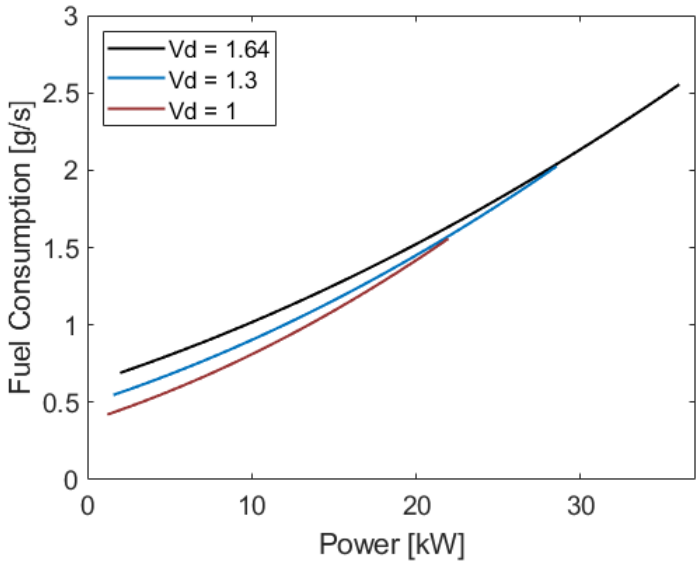

Figure 6.3: Fuel consumption of the OP engine system with respect to power output. This relationship can be normalized by the displacement volume (in liters) to allow for simple scaling of the engine while maintaining the same brake mean effective pressure.

divided by power to find the fuel flow rate. Furthermore, it is desirable to use a model that can be scaled to optimally size the engine. Therefore, by normalizing the power output of the engine by the displacement volume and using this normalized power, denoted as $\bar{P}_e = \frac{P_e}{V_d}$, multiplied by the BFSC, the fuel flow and power output of the engine can be determined while scaling the displacement volume, V_d, of the engine as shown in Fig. 6.3. The displacement volume of the engine now becomes a scaling parameter within the optimization problem.

To ensure a slow engine response that remains on the OOL, the normalized actual power from the engine is modeled as a first order response where

$$\dot{\bar{P}}_e = \frac{1}{t_{eng}}(\bar{P}_{e,dem} - \bar{P}_e) \tag{6.18}$$

where $\bar{P}_e$ is a state variable and t_{eng} denotes the time constant of the engine, which here will be set to 10 seconds for a slow engine response. Then, the rate of fuel consumption can be calculated from a fitted polynomial as

$$\dot{m}_f = N_0 + N_1\bar{P}_e + N_2\bar{P}_e^2 \tag{6.19}$$

where $N = [3.777e-1, \quad 3.440e-2, \quad 8.809e-4]$ using $\bar{P}_e$ in kilowatts and $\dot{m}_f$ in grams

per second. To provide a mass estimate of the engine for the vehicle model, a base engine mass of 130 kg is used for the 1.64 liter engine. For the sake of simplicity, the change in mass of the engine is considered proportional to the change in displacement volume.

6.3.4 Battery

Finally, with the power demand from the traction motor as well as the power supplied by the engine, the power supplied by the battery pack can be calculated as

$$P_b = P - P_e. \tag{6.20}$$

It is worth noting that the α input term utilized to set the engine power output can request an engine power larger than the power demand from the motor. This is an important distinction as this allows the engine to provide power to the traction motor while simultaneously charging the battery. Assuming a fully balanced battery pack, each cell contributes an equal amount of power for the battery pack where the cell power is $P_{cell} = {}^{P_b}/_{(n_p n_s)}$. The values of n_p and n_s denote the number of cells in parallel and series, respectively, and are used as parameters in the optimization process. Note, n_p and n_s are treated as continuous variables for optimization, but as the cell count is a discrete value, are rounded for the solution. Using the power required from the battery, the current applied to an individual cell can be calculated as

$$I_{cell} = \frac{V_{OCV}(z) - V_1 - \sqrt{(V_{OCV}(z) - V_1)^2 - 4RP_{cell}}}{2R} \tag{6.21}$$

where V_{OCV} is the open circuit voltage (OCV) and is a function of SOC, represented as z, and is determined through coulomb counting. The value of resistance, R, is set to $4m\Omega$. The battery dynamics are modeled at the cell level utilizing an equivalent circuit model of a Nickel-Manganese-Cobalt(NMC)/Graphite Li-ion prismatic cell based on the work from Samad et al. [106]. An OCV-R-RC model is used, meaning the equivalent circuit is made up of an OCV source connected in series with resistor (R) followed by a resistor-capacitor (RC) pair. To simplify the model, the resistance and capacitance in the RC pair is considered constant at $R_1 = 1m\Omega$ and $C_1 = 5e3F$. As this is a charge sustaining hybrid model and the SOC varies only slightly, this assumption has a relatively small impact on the cell dynamics. The dynamics of the RC pair is calculated as

$$\dot{V}_1 = \frac{-1}{R_1 C_1} V_1 + \frac{I_{cell}}{C} \tag{6.22}$$

Table 6.2: OCV Model Parameters

Constant	V_0	α	β	δ	ζ	ε
Value	3	4.3e-1	-20.5	4.4e-1	2.1e-1	1/5e-1

Table 6.3: Capacity Fade Model Parameters

Constant	σ	δ	c	μ	E_a	R_g
Value	125.2	-1925	2.618	0.5361	22406	8.314

where V_1 is considered to be the voltage drop across the resistor-capacitor pair.

The OCV curve is parameterized as

$$V_{OCV} = V_0 + \alpha(1 - exp(-\beta z)) + \gamma z + \zeta(1 - exp(\frac{-\varepsilon}{1-z})) \tag{6.23}$$

where V_0, α, β, γ, ζ, and ε are tuning parameters from the OCV model proposed by Hu et al. [107]. The parameters used to represent the NMC/Graphite cell are specified in Tab. 6.2.

To capture the capacity loss of the battery pack, the capacity fade model developed by Samad et al. [106] is

$$Q_{loss} = \sigma + \delta(0.66 - SOC_0)^c)exp(\frac{-E_a}{R_g T})Ah^{\mu} \tag{6.24}$$

which is dependent on the nominal operating SOC, SOC_0, which is a parameter of the optimization problem. The current throughput of the cell in amp hours is represented as Ah, and cell temperature as, T. The remaining parameters are specified in Tab. 6.3. The thermal model for the cell temperature is given by

$$\dot{T} = \frac{1}{mc_p}\left(\dot{Q}_{gen} + hA(T_\infty - T)\right) \tag{6.25}$$

where m is the mass of the cell, c_p is the lumped heat capacity, h is the convection coefficient and A is the surface area of the cell. These values are specified in Tab. 6.4.

However, for the capacity loss to be included in the cost function of the optimization process, as in Eqn. 6.2, a capacity loss rate is required. Therefore, assuming a constant temperature for this derivation and denoting that $Ah = \int_0^T I_{cell}dt/3600$, the derivative of Eqn.

Table 6.4: Thermal Model Parameters

Constant	m [kg]	c_p $\left[\frac{\text{J}}{\text{kgK}}\right]$	h $\left[\frac{\text{W}}{\text{m}^2\text{K}}\right]$	A [m^2]
Value	3.0e-2	1280	27.6	4.4e-1

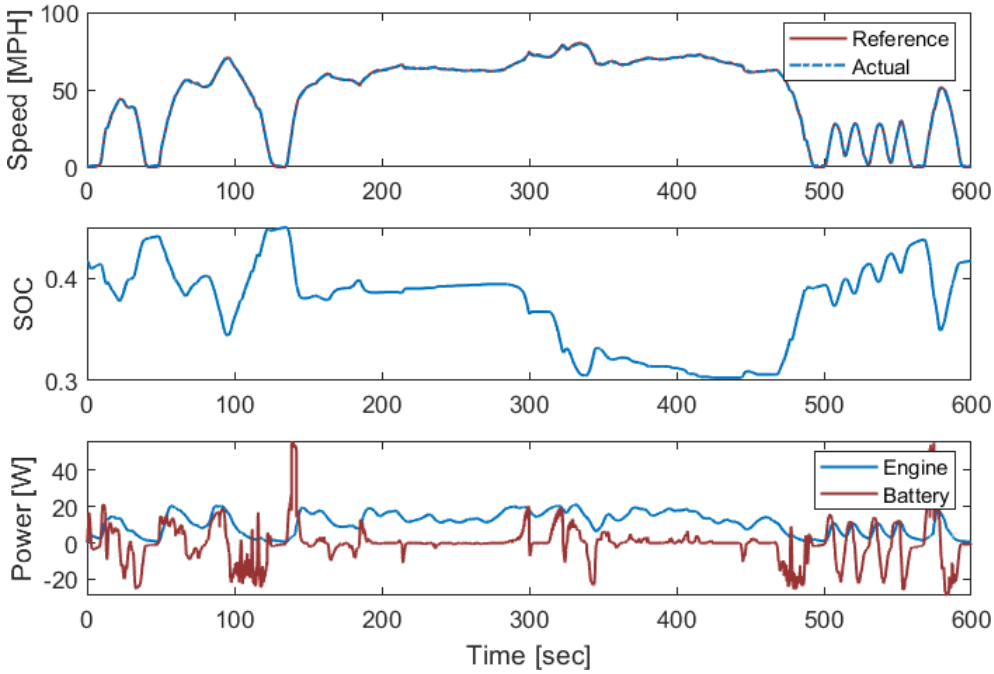

Figure 6.4: Resulting trajectories for the energy management in the HEV co-design problem. From top to bottom: Vehicle reference and actual speed, battery SOC, and the power supplied to the traction motor from the battery and engine. Due to the slow response of the engine, the battery is mainly used for load leveling while the engine provides smooth and relatively constant power to the traction motor.

6.24 is given as

$$\dot{Q}_{loss} = \left(\frac{\sigma_\delta (0.66 - SOC_0)^c}{3600^\mu}\right) exp\left(\frac{-Ea}{R_g T}\right) \mu A s^{\mu-1} |I_{cell}| \tag{6.26}$$

where the current throughput is now in amp seconds, As. Thus, As now becomes a state whose integral is simply the absolute value of I_{cell}.

6.4 Preliminary Results and Conclusions

The optimal control software used to solve Eqn. 6.2 subject to the constraints in Eqn. 6.3 was GPOPS-II [36], using the LuiRao-Legendre adaptive mesh refinement techniques

Table 6.5: Parameter Results for the HEV Powertrain Co-design Problem

Parameter	V_d	k_r	k_a	k_w	r_{FD}	SOC_0	n_p	n_s
Value	1	1.1	1.24	0.75	3.11	0.4	1	51

to discretize the optimal control problem. The resulting finite dimensional optimization problem is solved using IPOPT [37] with a mesh tolerance of $1e-3$ and an nonlinear programming problem (NLP) tolerance of $1e-2$. The objective of this chapter was to develop a flexible optimization framework to integrate the OP engine into a vehicle level design. Ideally, this tool can be directed to various vehicle models and drive cycles to investigate operating characteristics pertinent to those specific situations. As preliminary analysis, a smaller vehicle architecture in the Nissan Leaf was selected with the objective of analysing the influence of battery capacity fade and fuel consumption on the optimal operation of a series hybrid or range extender vehicle model.

For this initial analysis, the US06 drive cycle was selected as the velocity reference for the vehicle. The resulting vehicle speed, SOC, and power supplied by the engine and battery are shown in Fig. 6.4. The vehicle speed was constrained to maintain a tracking error of less than ± 2 mph from the reference velocity supplied by the US06 drive cycle. During the majority of the cycle, the vehicle maintains the reference speed well. However, it is interesting to note that at points where the reference demands 0 speed, the vehicle speed never comes to a complete stop. By maintaining a non-zero speed, the vehicle reduces the required power in the next acceleration.

In the sub-figure containing engine and battery power, it is clear that the battery is operating as a load leveling tool while the engine response is much slower and nearer the average power requirements of the vehicle. The slow response of the engine is in part due to the large time constant placed on the dynamics to ensure slow transients. However, by allowing the battery to cover the peak power demands, the engine can be downsized according to Fig 6.3, therefore reducing the overall fuel consumption but allowing the engine to operate near full load where the minimum BSFC is located.

Table 6.5 contains the sizing parameters selected. The engine is downsized to the minimum displacement volume allowed of 1 L. For the traction motor sizing, the radial and axial scaling increases. As shown in Eqn. 6.16d, this increases the torque capabilities of the motor. Further, the smaller winding parameter increases the base speed of the motor, which, when combining these three parameters, is effectively increasing the power capabilities of the motor. As the base motor model selected was used in a power split hybrid, it is expected that the motor model needs increased power capabilities to drive this vehicle in a series

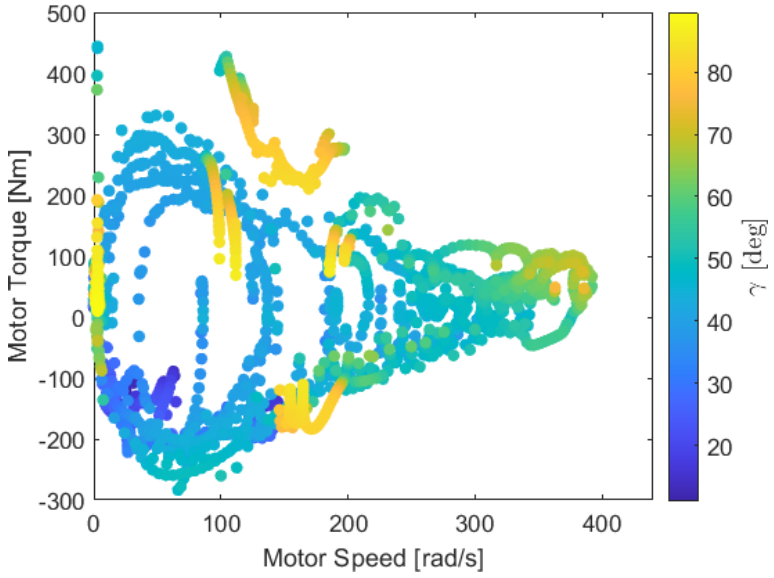

Figure 6.5: Torque and speed operating points for the traction motor over the drive cycle. The points are colored according to the current angle used.

hybrid format. However, the scaling is balanced with the increased losses as well as the increased mass for the electric machines.

The resulting torque and speed operation for the traction motor is shown in Fig. 6.5 with the color of the points indicating the current angle (γ) used at each point. The general trend of the figure shows an increase in γ as the speed of the motor increases, limiting the phase voltage of the motor under the set bus voltage. When not at the higher speeds, the majority of points operate near a γ of 45 degrees. As this is an interior permanent magnet motor, the saliency of the direct and quadrature axis means the peak torque per current angle is slightly below 45 degrees. However, there are areas within the map where the current angle is near 80 to 90 degrees when is does not need to be. These appear to be artifacts in the optimization algorithm and may require an increase in the tolerance of the NLP solution. However, as shown in Fig.!6.6, the time spent during the cycle with these gamma values is quite small and the losses resulting from the suboptimal current angle are negligible. Increasing the tolerances on the NLP can become computationally prohibitive in highly nonlinear and non-smooth problems such as this one. The large current angle values are typically utilized in high acceleration or deceleration areas within the drive cycle where flux weakening is expected for these high power demand situations.

Finally, the operational costs for both the engine and the battery are provided in Fig. 6.7. While the fuel cost from the engine operation is the larger contributor to the overall cost, the battery capacity fade presents a significant cost, even on such a short drive cycle. For

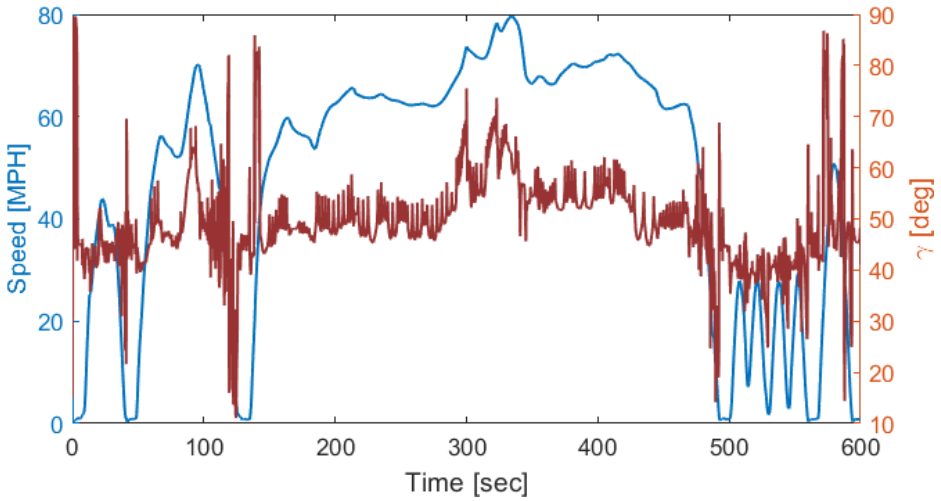

Figure 6.6: Vehicle speed and current angle trajectories during the drive cycle analysis. During periods of large acceleration or deceleration, γ is increased to limit the phase voltage of the motor.

the approximately 8 miles traveled for the US06 drive cycle, the cumulative fuel cost was \$0.77 while the battery cost was \$0.13.

From the initial results of the co-design framework, it is clear that an increase in the NLP tolerance is necessary to improve the accuracy of the resulting state and control trajectories from this co-design framework. However, the computational burden of such a large and nonlinear problem is limiting. Nonetheless, it is clear that the included battery capacity fade contributes to a significant portion of the total operating cost for the hybrid vehicle under consideration, highlighting the importance of this cost for future analysis. Further, capacity fade is not linear over the lifespan of the battery, suggesting that this analysis should be completed using different initial conditions for the charge throughput of the battery pack.

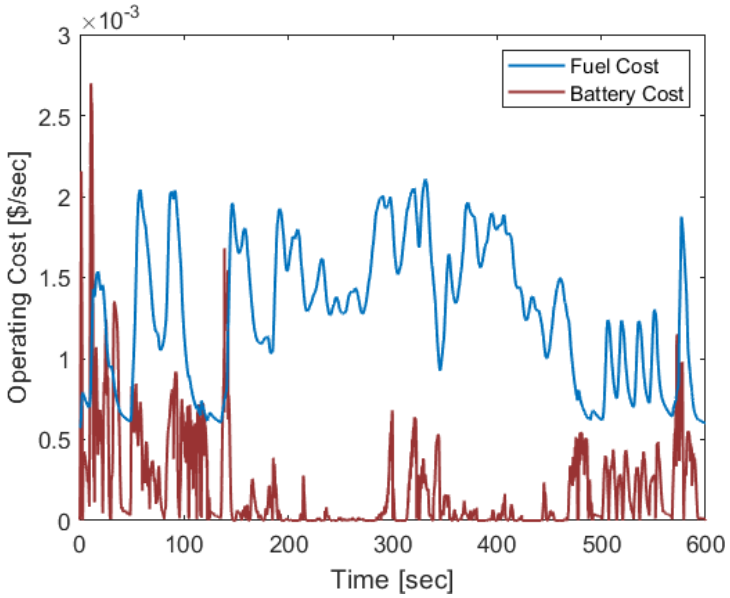

Figure 6.7: Operational costs for both the engine and battery pack. The engine cost is calculated from the fueling rate, while the battery cost is calculated from the capacity fade model. While the larger cost is associated with the engine, the battery operating cost presents a non-negligible cost, showing the importance of including battery cost in the optimization cost function.

CHAPTER 7

Conclusions and Future Work

7.1 Conclusions

In the current transition to low emission vehicle (LEV) technologies, hybrid electric vehicles (HEV) present a bridging vehicle architecture between internal combustion engine and battery technologies. These HEV powertrains are capable of capturing and also amplifying the benefits of each technology due to the diversified power sources on board the vehicle. This thesis investigates the use of a OP engine in a hybrid powertrain format in a effort to maximize the potential of hybridization. The OP engine was chosen for this study as it presents several advantages in a hybrid vehicle over a conventional ICE, with the focus of this work being on the inherently balanced nature of the OP engine; therefore, engine downsizing can be achieved by reducing the number of cylinders while keeping the combustion volume per cylinder the same and heat losses to a minimum. This work proposed eliminating the geartrain that couples the two crankshafts of a single cylinder OP engine and used a motor-generator on each crankshaft to directly extract mechanical work from combustion and convert it to electricity. The resulting analysis can be segregated into two domains: intra-cycle (Chapters 1-4) and inter-cycle (Chapters 5-6).

7.1.1 Intra-cycle Analysis

First, an optimization process of a 0-D model for the dual motor controlled OP engine intra-cycle dynamics to compute the crankshaft motion profile that maximizes the work generated by the system was formulated. This optimization was then iteratively coupled with a high fidelity model which supplied the cylinder flow boundary conditions. The iterative approach reduced the model complexity used in the optimal control problem (OCP) while capturing the gas exchange dynamics critical to the 2-stroke cycle of the OP engine. The results show crankshaft velocity slows during the compression stroke and conversely accelerates during the expansion stroke, reducing the peak motor torque

required for control and thus reducing the motor losses. The extended residence time at top dead center, however, leads to an increase in heat transfer, illustrating the trade-off between the work extraction efficiency and the indicated engine efficiency. However, the most consequential finding from this optimization process was the importance of accounting for the operating characteristics of the electric machines extracting work from the crankshafts. When neglecting the electric machine efficiency in the optimization problem, the BTE of the system was near 0%. When including the electric machine losses in the optimization, a BTE of 45% could be achieved.

With a better understanding of the coupling of crankshaft dynamics and electric machine operation, the next step was to evaluate the physical feasibility of this system. To that end, a linear quadratic regulator with an augmented integrator and feedforward estimation was developed to track the crankshaft motion profile on an experimental single cylinder OP engine utilizing electric machine torque as the control input. While the controller showed sufficient tracking capabilities, maintaining a position error of less than ± 1 degree, the physical system exhibited significant sensitivity to model uncertainty. Small perturbations in cylinder pressure with respect to piston position have a remarkably large impact on the instantaneous engine torque generation and thus, the motor torque required to track a crankshaft motion profile. The electric machine torque profile from experimentation showed a near 700 Nm discrepancy in peak amplitude to the torque expected from the offline optimization process.

At this point, it was relevant to question the theoretical performance benefits and limits of the dual motor controlled hybrid OP engine design. Therefore, a study was completed to compare the proposed dual motor design and a similar hybrid OP engine platform that utilized a geartrain to couple the crankshafts. While the dual motor design possessed the highest ceiling for work extraction efficiency of 93.5%, this level of efficiency was highly dependent on the ability to smooth the electric machine torque required to maintain control of the OP engine.

From these analyses, it was clear that this system does present a feasible series hybrid architecture which can be adequately controlled to a given crankshaft motion profile. However, the accuracy of the simplified models used for the optimization were limited in order to make the problem numerically tractable in an optimal control problem, thereby limiting the ability of the calculated crankshaft motion trajectories to be translated to the physical setup. Thus, a novel, real-time trajectory optimization scheme was developed. Theoretical convergence criteria was provided for this new iterative trajectory optimization scheme, followed by the practical application to the crankshaft motion planning of the OP engine. The algorithm was able to reduce the peak to peak electric machine torque

amplitude to 297 Nm, an approximate 57% reduction in the torque oscillations as compared to the initial experimental tests with trajectories from offline optimization.

7.1.2 Inter-cycle Analysis

With a reliable intra-cycle control structure developed, consideration was then given to the inter-cycle operation and the capability of varying the exhaust crankshaft lead (ECL) of the engine during operation. As calibration of ICEs is typically a very time intensive process, this work implemented an onboard setpoint optimization technique to investigate the optimal operating setpoint of engine speed and ECL for two different output power setpoints. While the optimization scheme reliably reduced the BSFC at all initialization points considered, the operation of the OP engine showed very little sensitivity to changes in ECL at these operating conditions due to the trade-off between boost pressure requirements and the effective compression and expansion ratio of the engine. For the optimal speed conditions, the BTE varied less than 2% for a sweep of ECL from -4 to 8 degrees.

Finally, the last technical chapter in this thesis provided a optimization framework for the component sizing and energy management of a vehicle utilizing a series hybrid powertrain featuring an OP engine on a drive cycle timescale. An optimal operating line for the OP engine was used to define the fuel consumption for the vehicle and a preliminary analysis investigated the relative operational costs of fuel consumption of the engine and capacity fade within the hybrid vehicle battery pack. For the drive cycle considered, 13% of the operating cost for the vehicle was due to capacity fade within the vehicle, showing the importance of including the cost due to battery capacity loss when attempting to minimize the cost of operating an HEV.

7.2 Future Work and Open Challenges

In this work, the potential of a series hybrid OP engine powertrain architecture was investigated. It would be interesting to consider other available hybrid powertrain topologies that can highlight the novel attributes of the OP engine such as the two crankshafts available on an OP engine. Adding this additional degree of freedom to the design of a hybrid powertrain presents significant challenges, but also significant opportunities to expand the design space of current hybrid topologies. The iterative trajectory optimization algorithm developed here is easily adaptable to other power take-off strategies. However, sizing of the hybrid drive components and OP engine should also

be addressed in that future work as the results in Chapter 3 highlight the importance of properly sized electric machines. Further, future electric machine design could enable higher system efficiency for cyclic torque profiles by re-distributing the machine windings across the crank angles of interest near minimum volume of the engine.

In addition, this powertrain design has a significant disposition towards fuel agnostic operation. For example, the majority of Chapters 1-4 was completed using a GCI combustion strategy. However, the Chapter 5 was completed using F24 rather than gasoline with only a slight change to the injection strategy. Use of the ECL as an actuator to regulate combustion stability for fuels of varying reactivity would also be interesting. Salvi et al. [14] have already proposed varying the boost pressure supplied to the OP engine as a means to regulate internal exhaust gas recirculation (EGR) and maintain combustion stability for GCI. Could the ECL actuation be used to extend the possible operating range of such strategies?

Finally, the developed ITO algorithm can certainly have applications beyond that of the hybrid OP engine. In particular, the Fourier series parameterization implemented in the ITO scheme may lend itself well to identifying harmonics within the induced voltage of interior permanent magnet synchronous machines, helping to inject the phase currents with the same harmonic content to maximize the torque generated by the same current amplitude.

BIBLIOGRAPHY

[1] *Energy Technology Perspectives 2020*. OECD, sep 2020.

[2] Derek Splitter, Alexander Pawlowski, and Robert Wagner. A historical analysis of the co-evolution of gasoline octane number and spark-ignition engines. *Frontiers in Mechanical Engineering*, 1, jan 2016.

[3] Xiaodong Yuan and Yuchen Cai. Forecasting the development trend of low emission vehicle technologies: Based on patent data. *Technol Forecast Soc*, 166:120651, may 2021.

[4] Alex G. Young, Aaron W. Costall, Daniel Coren, and James W. G. Turner. The effect of crankshaft phasing and port timing asymmetry on opposed-piston engine thermal efficiency. *Energies*, 14(20):6696, oct 2021.

[5] José Ramón Serrano, Antonio García, Javier Monsalve-Serrano, and Santiago Martínez-Boggio. High efficiency two stroke opposed piston engine for plug-in hybrid electric vehicle applications: Evaluation under homologation and real driving conditions. *Appl Energ*, 282:116078, jan 2021.

[6] Joseph Austin Drallmeier, Heath Hofmann, Robert Middleton, Jason Siegel, Anna Stefanopoulou, and Ashwin Salvi. Work extraction efficiency in a series hybrid opposed piston engine. In *SAE Technical Paper Series*. SAE International, sep 2021.

[7] Randy E. Herold, Michael H. Wahl, Gerhard Regner, James U. Lemke, and David E. Foster. Thermodynamic benefits of opposed-piston two-stroke engines. In *SAE Technical Paper Series*. SAE International, sep 2011.

[8] Michael A Willcox, James M Cleeves, Simon Jackson, Michael Hawkes, and Joshua Raimond. Indicated cycle efficiency improvements of a 4-stroke, high compression ratio, s.i., opposed-piston, sleeve-valve engine using highly delayed spark timing for knock mitigation. In *SAE Technical Paper Series*. SAE International, apr 2012.

[9] Pirault. *Opposed piston engines : evolution, use, and future applications*. SAE International, Warrendale, Pa, 2010.

[10] Ke Li, Wilson Santiago, and Zongxuan Sun. Modeling of a two-stroke free-piston engine with HCCI combustion. In *ASME 2010 Dynamic Systems and Control Conference*. ASMEDC, jan 2010.

[11] Chen Zhang and Zongxuan Sun. Using variable piston trajectory to reduce engine-out emissions. *Appl Energ*, 170:403–414, may 2016.

[12] Suramya Naik, David Johnson, John Koszewnik, Laurence Fromm, Fabien Redon, Gerhard Regner, and Kevin Fuqua. Practical applications of opposed-piston engine technology to reduce fuel consumption and emissions. In *SAE Technical Paper Series*. SAE International, nov 2013.

[13] Gerhard Regner, Randy E. Herold, Michael H. Wahl, Eric Dion, Fabien Redon, David Johnson, Brian J. Callahan, and Shauna McIntyre. The achates power opposed-piston two-stroke engine: Performance and emissions results in a medium-duty application. *SAE International Journal of Engines*, 4(3):2726–2735, sep 2011.

[14] *Initial Results on a New Light-Duty 2.7L Opposed-Piston Gasoline Compression Ignition Multi-Cylinder Engine*, volume Volume 1: Large Bore Engines; Fuels; Advanced Combustion of *Internal Combustion Engine Division Fall Technical Conference*, 11 2018. V001T03A010.

[15] Gerhard Regner, David Johnson, John Koszewnik, Eric Dion, Fabien Redon, and Laurence Fromm. Modernizing the opposed piston, two stroke engine for clean, efficient transportation. In *SAE Technical Paper Series*. SAE International, jan 2013.

[16] Ke Li, Ali Sadighi, and Zongxuan Sun. Active motion control of a hydraulic free piston engine. *IEEE/ASME Transactions on Mechatronics*, 19(4):1148–1159, aug 2014.

[17] Chen Zhang, Ke Li, and Zongxuan Sun. Modeling of piston trajectory-based hcci combustion enabled by a free piston engine. *Applied Energy*, 139:313–326, 2015.

[18] Chen Zhang and Zongxuan Sun. Trajectory-based combustion control for renewable fuels in free piston engines. *Appl Energ*, 187:72–83, feb 2017.

[19] Suramya Naik, Fabien Redon, Gerhard Regner, and John Koszewnik. Opposed-piston 2-stroke multi-cylinder engine dynamometer demonstration. In *SAE Technical Paper Series*. SAE International, jan 2015.

[20] Enrico Mattarelli, Carlo Rinaldini, Tommaso Savioli, Giuseppe Cantore, Alok Warey, Michael Potter, Venkatesh Gopalakrishnan, and Sandro Balestrino. Scavenge ports ooptimization of a 2-stroke opposed piston diesel engine. In *SAE Technical Paper Series*. SAE International, sep 2017.

[21] Siddhartha Banerjee, Clayton Naber, Michael Willcox, Charles Finney, and K. Edwards. High performance computing and analysis-led development of high efficiency dilute opposed piston gasoline engine. page V001T03A012, 10 2017.

[22] Michael Mozurkewich and R. Stephen Berry. Optimal paths for thermodynamic systems: The ideal otto cycle. *J Appl Phys*, 53(1):34–42, jan 1982.

[23] Karl Heinz Hoffmann, Stanley J. Watowich, and R. Stephen Berry. Optimal paths for thermodynamic systems: The ideal diesel cycle. *J Appl Phys*, 58(6):2125–2134, sep 1985.

[24] Jing Xu, Chenheng Yuan, Yituan He, and Rong Wang. An optimization of free-piston engine generator combustion using variable piston motion. *Advances in Mechanical Engineering*, 9(9):168781401772087, sep 2017.

[25] Lars Eriksson and Martin Sivertsson. Computing optimal heat release rates in combustion engines. *SAE International Journal of Engines*, 8(3):1069–1079, apr 2015.

[26] Lars Eriksson and Martin Sivertsson. Calculation of optimal heat release rates under constrained conditions. *SAE International Journal of Engines*, 9(2):1143–1162, apr 2016.

[27] Joseph Drallmeier, Jason B. Siegel, Robert Middleton, Anna G. Stefanopoulou, Ashwin Salvi, and Ming Huo. Modeling and control of a hybrid opposed piston engine. In *ASME 2021 ICEF*. American Society of Mechanical Engineers, oct 2021.

[28] Xunzhao Yu, Ling Zhu, Yan Wang, Dimitar Filev, and Xin Yao. Internal combustion engine calibration using optimization algorithms. *Applied Energy*, 305:117894, jan 2022.

[29] Anuj Pal, Yan Wang, Ling Zhu, and Guoming George Zhu. Multi-objective surrogate-assisted stochastic optimization for engine calibration. *Journal of Dynamic Systems, Measurement, and Control*, apr 2021.

[30] D. Popovic, M. Jankovic, S. Magner, and A.R. Teel. Extremum seeking methods for optimization of variable cam timing engine operation. *IEEE Transactions on Control Systems Technology*, 14(3):398–407, may 2006.

[31] Dimitar Filev, Yan Wang, and Ilya Kolmanovsky. Learning based approaches to engine mapping and calibration optimization. In *Optimization and Optimal Control in Automotive Systems*, pages 257–272. Springer International Publishing, 2014.

[32] Andreas A. Malikopoulos, Dennis N. Assanis, and Panos Y. Papalambros. Real-time self-learning optimization of diesel engine calibration. *Journal of Engineering for Gas Turbines and Power*, 131(2), dec 2008.

[33] Joseph A Drallmeier, Robert J Middleton, and Jason B Siegel. Optimizing the fuel efficiency of an opposed piston engine for electric power generation. *International Journal of Engine Research*, page 146808742211210, sep 2022.

[34] *Comparison of Estimation Techniques for the Crankshaft Dynamics of an Opposed Piston Engine*, volume Volume 1: Advanced Driver Assistance and Autonomous Technologies; Advances in Control Design Methods; Advances in Robotics; Automotive Systems; Design, Modeling, Analysis, and Control of Assistive and

Rehabilitation Devices; Diagnostics and Detection; Dynamics and Control of Human-Robot Systems; Energy Optimization for Intelligent Vehicle Systems; Estimation and Identification; Manufacturing of *Dynamic Systems and Control Conference*, 10 2019. V001T04A006.

[35] Joseph A. Drallmeier, Jason B. Siegel, and Anna G. Stefanopoulou. Iterative learning-based trajectory optimization using fourier series basis functions. *IEEE Control Systems Letters*, 6:2180–2185, 2022.

[36] Michael A. Patterson and Anil V. Rao. GPOPS-II. *ACM Trans. Math. Software*, 41(1):1–37, oct 2014.

[37] Andreas Wächter and Lorenz T. Biegler. On the implementation of an interior-point filter line-search algorithm for large-scale nonlinear programming. *Appl Manag Sci*, 106(1):25–57, apr 2005.

[38] G. P. Merker and M. Gerstle. Evaluation on two stroke engines scavenging models. In *SAE Technical Paper Series*. SAE International, feb 1997.

[39] GT-Suite Manual G.-P.U. *GT-Suite version 2020.0*. Gamma Technologies Inc.

[40] Ahmed Yar, A. I. Bhatti, and Qadeer Ahmed. First principle-based control oriented model of a gasoline engine. *J. Dyn. Syst. Meas. Contr.*, 139(5), mar 2017.

[41] G. Woschni. A universally applicable equation for the instantaneous heat transfer coefficient in the internal combustion engine. In *SAE Technical Paper Series*. SAE International, feb 1967.

[42] J I Ghojel. Review of the development and applications of the wiebe function: A tribute to the contribution of ivan wiebe to engine research. *Int J Engine Res*, 11(4):297–312, jun 2010.

[43] Yingcong Zhou, Deivanayagam Hariharan, Ruinan Yang, Sotirios Mamalis, and Benjamin Lawler. A predictive 0-d HCCI combustion model for ethanol, natural gas, gasoline, and primary reference fuel blends. *Fuel*, 237:658–675, feb 2019.

[44] J.C. Livengood and P.C. Wu. Correlation of autoignition phenomena in internal combustion engines and rapid compression machines. *Symposium (International) on Combustion*, 5(1):347–356, jan 1955.

[45] Z. S. Filipi and D. N. Assanis. A nonlinear, transient, single-cylinder diesel engine simulation for predictions of instantaneous engine speed and torque. *Journal of Engineering for Gas Turbines and Power*, 123(4):951–959, oct 2000.

[46] F. Yusivar, N. Hidayat, R. Gunawan, and A. Halim. Implementation of field oriented control for permanent magnet synchronous motor. In *2014 International Conference on Electrical Engineering and Computer Science (ICEECS)*. IEEE, nov 2014.

[47] He Song and Heath Hofmann. Robust, accurate systems-based power electronic circuit models in simulink. In *2018 IEEE 19th Workshop on Control and Modeling for Power Electronics (COMPEL)*. IEEE, jun 2018.

[48] Greg Horn, Sébastien Gros, and Moritz Diehl. Numerical trajectory optimization for airborne wind energy systems described by high fidelity aircraft models. *Airborne Wind Energy*, pages 205–218, 2013.

[49] J. P. Barreto, F. J.F. Schöler, and B. Corves. The concept of natural motion for pick and place operations. *Mechanisms and Machine Science*, 46:89–98, 2017.

[50] Stefania Pellegrinelli, Stefano Borgia, Nicola Pedrocchi, Enrico Villagrossi, Giacomo Bianchi, and Lorenzo Molinari Tosatti. Minimization of the energy consumption in motion planning for single-robot tasks. *Procedia CIRP*, 29:354–359, 2015.

[51] Seunghan Lim and Hyochoong Bang. Waypoint guidance of cooperative uavs for intelligence, surveillance, and reconnaissance. *IEEE ICCA*, pages 291–296, 2009.

[52] Mitchell K. Cobb, Kira Barton, Hosam Fathy, and Chris Vermillion. Iterative learning-based path optimization for repetitive path planning, with application to 3-d crosswind flight of airborne wind energy systems. *IEEE Trans Contr Syst Technol*, 28(4):1447–1459, jul 2020.

[53] Douglas A. Bristow, Marina Tharayil, and Andrew G. Alleyne. A survey of iterative learning control. *IEEE Control Syst.*, 26(3):96–114, jun 2006.

[54] Youqing Wang, Furong Gao, and Francis J Doyle. Survey on iterative learning control , repetitive control , and run-to-run control. *Journal of Process Control*, 19:1589–1600, 2009.

[55] Lukas G. Dekker, Joshua A. Marshall, and Johan Larsson. Industrial-scale autonomous wheeled-vehicle path following by combining iterative learning control with feedback linearization. *IEEE ICIRS*, pages 2643–2648, 2017.

[56] Lennart Blanken, Sjirk Koekebakker, and Tom Oomen. Data-driven feedforward tuning using non-causal rational basis functions: With application to an industrial flatbed printer. *Mechatronics*, 71, 2020.

[57] Patrick M. Sammons, Douglas A. Bristow, and Robert G. Landers. Iterative learning control of bead morphology in laser metal deposition processes. *Proceedings of the ACC*, pages 5942–5947, 2013.

[58] Ingyu Lim and Kira L Barton. Pareto optimization-based iterative learning control. *Proceedings of the ACC*, pages 5171–5176, 2013.

[59] Chris T Freeman and Ying Tan. Iterative learning control with mixed constraints for point-to-point tracking. *Ieee TCST*, 21:604–616, 2013.

[60] David H. Owens, Chris T. Freeman, and Bing Chu. Multivariable norm optimal iterative learning control with auxiliary optimisation. *International Journal of Control*, 86:1026–1045, 2013.

[61] Douglas A. Bristow, Kira L. Barton, and Andrew G. Alleyne. Iterative learning control. *The Control Systems Handbook: Control System Advanced Methods, 2nd Ed*, pages 857–876, 2010.

[62] Dimitry Gorinevsky. Loop shaping for iterative control of batch processes. *IEEE Control Systems Magazine*, 22:55–65, 2002.

[63] Xiaoqi Tang, Lilong Cai, and Weiqing Huang. A learning controller for robot manipulators using fourier series. *IEEE TRA*, 16:36–45, 2000.

[64] Wubi Qin and Lilong Cai. A fourier series based iterative learning control for nonlinear uncertain systems. *IEEE/ASME ICAIM*, pages 482–487, 2001.

[65] Daniel Mellinger and Vijay Kumar. Minimum snap trajectory generation and control for quadrotors. *Proceedings - IEEE ICRA*, pages 2520–2525, 2011.

[66] Jorge Nocedal and Stephen Wright. *Numerical Optimization*. Springer, 2006.

[67] R. Gupta, I. V. Kolmanovsky, Yan Wang, and D. P. Filev. Onboard learning-based fuel consumption optimization in series hybrid electric vehicles. In *2012 American Control Conference (ACC)*. IEEE, jun 2012.

[68] Karsten ROEPKE. Design of experiments for engine calibration. *Journal of The Society of Instrument and Control Engineers*, 53(4):322–327, 2014.

[69] Farhad Salek, Meisam Babaie, Seyed Vahid Hosseini, and O. Anwar Bég. Multi-objective optimization of the engine performance and emissions for a hydrogen/gasoline dual-fuel engine equipped with the port water injection system. *International Journal of Hydrogen Energy*, 46(17):10535–10547, mar 2021.

[70] Chris Atkinson and Gregory Mott. Dynamic model-based calibration optimization: An introduction and application to diesel engines. In *SAE Technical Paper Series*. SAE International, apr 2005.

[71] Vincenzo De Bellis. Performance optimization of a spark-ignition turbocharged VVA engine under knock limited operation. *Applied Energy*, 164:162–174, feb 2016.

[72] Jinxing Zhao and Min Xu. Fuel economy optimization of an atkinson cycle engine using genetic algorithm. *Applied Energy*, 105:335–348, may 2013.

[73] Ehsan Samadani, Amir Hossein Shamekhi, Mohammad Hassan Behroozi, and Reza Chini. A method for pre-calibration of di diesel engine emissions and performance using neural network and multi-objective genetic algorithm. *Iranian Journal of Chemistry and Chemical Engineering (IJCCE)*, 28, 2009.

[74] Tobias Gutjahr, Thomas Kruse, and Thorsten Huber. Advanced modeling and optimization for virtual calibration of internal combustion engines. In *NDIA Ground Vehicle Systems Engineering and Technology Symposium*, 2017.

[75] Yui Nishio, Yutaka Murata, Yukihisa Yamaya, and Masato Kikuchi. Optimal calibration scheme for map-based control of diesel engines. *Science China Information Sciences*, 61(7), jun 2018.

[76] Jinwu Gao, Yahui Zhang, and Tielong Shen. An on-board calibration scheme for map-based combustion phase control of spark-ignition engines. *IEEE/ASME Transactions on Mechatronics*, 22(4):1485–1496, aug 2017.

[77] Andreas A. Malikopoulos, Panos Y. Papalambros, and Dennis N. Assanis. A learning algorithm for optimal internal combustion engine calibration in real time. In *Volume 6: 33rd Design Automation Conference, Parts A and B*. ASMEDC, jan 2007.

[78] Carlos Guardiola, Benjamín Pla, Pau Bares, and Harald Waschl. Adaptive calibration for reduced fuel consumption and emissions. *Proceedings of the Institution of Mechanical Engineers, Part D: Journal of Automobile Engineering*, 230(14):2002–2014, aug 2016.

[79] Carlos Guardiola, Héctor Climent, Benjamín Pla, and Alberto Reig. Optimal control as a method for diesel engine efficiency assessment including pressure and NO x constraints. *Applied Thermal Engineering*, 117:452–461, may 2017.

[80] Jose Manuel Luján, Carlos Guardiola, Benjamín Pla, and Alberto Reig. Optimal control of a turbocharged direct injection diesel engine by direct method optimization. *International Journal of Engine Research*, 20(6):640–652, may 2018.

[81] He Ma, Ziyang Li, Mohamad Tayarani, Guoxiang Lu, Hongming Xu, and Xin Yao. Model-based computational intelligence multi-objective optimization for gasoline direct injection engine calibration. *Proceedings of the Institution of Mechanical Engineers, Part D: Journal of Automobile Engineering*, 233(6):1391–1402, jun 2018.

[82] Xun Shen, Yahui Zhang, Tielong Shen, and Chanyut Khajorntraidet. Spark advance self-optimization with knock probability threshold for lean-burn operation mode of SI engine. *Energy*, 122:1–10, mar 2017.

[83] He Ma, Hongming Xu, Jihong Wang, Thorsten Schnier, Ben Neaves, Cheng Tan, and Zhi Wang. Model-based multiobjective evolutionary algorithm optimization for HCCI engines. *IEEE Transactions on Vehicular Technology*, 64(9):4326–4331, sep 2015.

[84] Qingyuan Tan, Prasad Divekar, Ying Tan, Xiang Chen, and Ming Zheng. Model-guided extremum seeking for diesel engine fuel injection optimization. *IEEE/ASME Transactions on Mechatronics*, 23(2):936–946, apr 2018.

[85] US Environmental Protection Agency. Highlights of the automotive trends report. techreport, 2020.

[86] Nathaniel S. Pearre, Willett Kempton, Randall L. Guensler, and Vetri V. Elango. Electric vehicles: How much range is required for a day's driving? *Transportation Research Part C: Emerging Technologies*, 19(6):1171–1184, dec 2011.

[87] Alexandros Dimitropoulos, Piet Rietveld, and Jos N. van Ommeren. Consumer valuation of changes in driving range: A meta-analysis. *Transportation Research Part A: Policy and Practice*, 55:27–45, sep 2013.

[88] M.C. McManus. Environmental consequences of the use of batteries in low carbon systems: The impact of battery production. *Applied Energy*, 93:288–295, may 2012.

[89] Thomas Franke and Josef F. Krems. What drives range preferences in electric vehicle users? *Transp Policy*, 30:56–62, nov 2013.

[90] A. Solouk, J. Tripp, M. Shakiba-Herfeh, and M. Shahbakhti. Fuel consumption assessment of a multi-mode low temperature combustion engine as range extender for an electric vehicle. *Energy Conversion and Management*, 148:1478–1496, sep 2017.

[91] Emilia Silvas, Theo Hofman, Nikolce Murgovski, Pascal Etman, and Maarten Steinbuch. Review of optimization strategies for system-level design in hybrid electric vehicles. *IEEE Transactions on Vehicular Technology*, pages 1–1, 2016.

[92] Arian Houshmand. Multidisciplinary dynamic system design optimization of hybrid electric vehicle powertrains. Master's thesis, University of Cincinnati, 2016.

[93] H.K. Fathy, J.A. Reyer, P.Y. Papalambros, and A.G. Ulsov. On the coupling between the plant and controller optimization problems. In *Proceedings of the 2001 American Control Conference. (Cat. No.01CH37148)*. IEEE, 2001.

[94] James T. Allison and Daniel R. Herber. Special section on multidisciplinary design optimization: Multidisciplinary design optimization of dynamic engineering systems. *AIAA Journal*, 52(4):691–710, apr 2014.

[95] Alparslan Emrah Bayrak, Namwoo Kang, and Panos Y. Papalambros. Decomposition-based design optimization of hybrid electric powertrain architectures: Simultaneous configuration and sizing design. *Journal of Mechanical Design*, 138(7), jun 2016.

[96] *Optimal Dual-Mode Hybrid Electric Vehicle Powertrain Architecture Design for a Variety of Loading Scenarios*, volume Volume 3: 16th International Conference on Advanced Vehicle Technologies; 11th International Conference on Design Education; 7th Frontiers in Biomedical Devices of *International Design Engineering Technical Conferences and Computers and Information in Engineering Conference*, 08 2014. V003T01A005.

[97] Bo Egardt, Nikolce Murgovski, Mitra Pourabdollah, and Lars Johannesson Mardh. Electromobility studies based on convex optimization: Design and control issues regarding vehicle electrification. *IEEE Control Systems*, 34(2):32–49, apr 2014.

[98] Nikolce Murgovski, Xiaosong Hu, Lars Johannesson, and Bo Egardt. *Combined Design and Control Optimization of Hybrid Vehicles*, pages 1–14. John Wiley and Sons, Ltd, 2015.

[99] Lianghong Wu, Yaonan Wang, Xiaofang Yuan, and Zhenlong Chen. Multiobjective optimization of HEV fuel economy and emissions using the self-adaptive differential evolution algorithm. *IEEE Transactions on Vehicular Technology*, 60(6):2458–2470, jul 2011.

[100] Saeed Azad and Michael J. Alexander-Ramos. Robust combined design and control optimization of hybrid-electric vehicles using MDSDO. *IEEE Transactions on Vehicular Technology*, 70(5):4139–4152, may 2021.

[101] Qian Xun, Nikolce Murgovski, and Yujing Liu. Chance-constrained robust co-design optimization for fuel cell hybrid electric trucks. *Applied Energy*, 320:119252, aug 2022.

[102] J. Goss, P.H. Mellor, R. Wrobel, D.A. Staton, and M. Popescu. The design of AC permanent magnet motors for electric vehicles: a computationally efficient model of the operational envelope. In *6th IET International Conference on Power Electronics, Machines and Drives (PEMD 2012)*. IET, 2012.

[103] Stjepan Stipetic, Damir Zarko, and Mircea Popescu. Ultra-fast axial and radial scaling of synchronous permanent magnet machines. *IET Electric Power Applications*, 10(7):658–666, aug 2016.

[104] Stjepan Stipetic, James Goss, Damir Zarko, and Mircea Popescu. Calculation of efficiency maps using a scalable saturated model of synchronous permanent magnet machines. *IEEE Transactions on Industry Applications*, 54(5):4257–4267, sep 2018.

[105] J.S. Hsu, C. W. Ayers, C. L. Coomer, R. H. Wiles, S.L. Campbell, K.T. Lowe, and R. T. Michelhaugh. Report on toyota/prius motor torque capability ,torque property, no-load back emf, and mechanical losses. Technical report, Oak Ridge National Laboratory, 2004.

[106] Nassim A. Samad, Youngki Kim, and Jason B. Siegel. On power denials and lost energy opportunities in downsizing battery packs in hybrid electric vehicles. *Journal of Energy Storage*, 16:187–196, apr 2018.

[107] Y. Hu, S. Yurkovich, Y. Guezennec, and B.J. Yurkovich. Electro-thermal battery model identification for automotive applications. *Journal of Power Sources*, 196(1):449–457, jan 2011.